Diss. ETH No. 19457

Failure of weak snow layers

Ingrid Reiweger

2011

Diss. ETH No. 19457

FAILURE OF WEAK SNOW LAYERS

A dissertation submitted to the

ETH ZÜRICH

for the degree of

Doctor of Sciences

presented by

INGRID REIWEGER

Dipl. Ing., Technische Universität Graz

born 25 September, 1978

citizen of Austria

Accepted on the recommendation of

Prof. Dr. Jürg Dual (ETH Zürich)

Dr. Jürg Schweizer (SLF Davos)

Prof. Dr. Hans-Jürgen Herrmann (ETH Zürich)

2011

Acknowledgements

First of all I would like to express my gratitude to my supervisor Jürg Schweizer. His advise, support, and encouragement were essential for my research and the writing of this thesis. Many thanks also to my doctoral advisor Jürg Dual and my second advisor Hans-Jürgen Herrmann for their time and many fruitful discussions where we developed new ideas. I appreciate that Robert Ernst, Thomas Huber, Marco Frigerio, and Klemens Mayer trusted me to supervise their Master's respectively Bachelor's Theses. While working with them I guess I learned at least as much as they did. I am also very grateful for the support provided by my colleagues at SLF: Julia Kowalski, Bernd Pinzer, Christoph Mitterer, Alec van Herwijnen, Michael Schirmer, Johanna Spiegel, Susanna Hoinkes, Marc Christen, Martin Schneebeli, Michael Lehning, and Sascha Bellaire. Furthermore, thanks to Matthias Jaggi, Stephen Steiner, Christian Simeon, and Andreas Tröger for technical support. My deepest thanks go to my friends and family, especially to Romano and Adrian. Last but not least, thank you Markus Aichhorn, Christian Scheiber, and Ralf Gamillscheg for drawing my attention to this PhD position and for convincing me to move to Switzerland.

Ingrid Reiweger — Davos, November, 2010

Contents

Summary

Dry-snow slab avalanches start with a failure within a weak snow layer beneath a cohesive snow slab. The objective of this thesis was to investigate the failure behaviour of such weak snow layers.

In a first part the weak layer was modeled with a fibre bundle model, introducing instantaneous breaking of bonds between crystals and a finite healing time for broken bonds. Using these two different times the rate-dependent failure behaviour of snow could be reproduced - snow fails in a brittle manner if deformed or loaded quickly, while it fails in a ductile manner if deformed or loaded slowly.

In a second part two kinds of experiments were performed, displacement-controlled shear experiments and force-controlled loading experiments. During the shear experiments the snow sample was deformed in simple shear, and the force needed to achieve the deformation was measured. For the loading experiments the snow sample was tilted by a 'slope angle' within our newly designed apparatus and loaded by the gravitational force. The deformation field on the side of the snow sample was measured optically with a particle image velocimetry algorithm. In addition acoustic emission signals were counted in order to assess the pre-catastrophic fractures occurring within the snow samples.

Both kinds of experiments displayed the expected strain- and loading-rate dependent failure behaviour of snow. The shear strain was constant over the sample height for homogeneous snow samples. Within layered snow samples a strong concentration of shear deformation at the weak layer and hardly any shear deformation within the layers above and below the weak layer was observed. This concentration of deformation justifies the commonly used modelling assumption of a stiff slab and substratum above and below the weak layer. It also suggests that in a natural snowpack local strains within weak layers may be high enough for catastrophic failure despite low global strains of the whole snowpack.

Force-controlled loading experiments with a weak surface hoar layer showed that the strength of the layer decreased with loading rate and also with slope angle. The latter illustrates the anisotropic failure behaviour of surface hoar, it is weaker in shear than in compression. We therefore conclude that natural dry-snow slab avalanche release is rather caused by the shear component of deformation than by the compressive component - at least if the failure layer consists of surface hoar. For the slab release process in nature, this decrease in strength with increasing slope angle indicates that failure initiation and therewith avalanche formation is more probable in steep terrain due to the shear component of deformation, this is in agreement with observations.

Zusammenfassung

Trockene Schneebrettlawinen beginnen mit einem Versagen in einer schwachen Schneeschicht, welche unter einer kohäsiven Schneeschicht liegt. Die Zielsetzung dieser Dissertation war es, das Versagensverhalten solcher schwachen Schneeschichten zu untersuchen.

In einem ersten Teil wurde die schwache Schneeschicht mit einem Faserbündelmodell modelliert. Dabei wurde instantanes Brechen von Verbindungen zwischen Schneekörnern und gleichzeitig eine endliche Zeit für das Heilen gebrochener Bindungen eingeführt. Es konnte gezeigt werden, dass allein diese beiden verschiedenen Zeiten ausreichen, um das verformungsgeschwindigkeitsabhängige Verhalten von Schnee qualitativ richtig zu beschreiben. Schnee zeigt sprödes Verhalten bei schnellen Verformungen und Belastungen sowie duktiles Verhalten bei langsamen Verformungen und Belastungen.

In einem zweiten Teil wurden zwei Arten von Experimenten durchgeführt, verformungskontrollierte Scherexperimente und kraftkontrollierte Belastungsexperimente. Bei den Scherexperimenten wurde die Schneeprobe in einfacher Scherung verformt, und die Kraft, die dazu nötig war, wurde gemessen. Bei den Belastungsexperimenten wurde die Schneeprobe in unserem neu entworfenen Scherapparat um einen 'Hangneigungswinkel' geneigt und mithilfe der Gravitationskraft belastet. Das Deformationsfeld der Schneeprobe in Seitenansicht wurde optisch mit einem Mustererkennungsalgorithmus gemessen. Zusätzlich wurden akustische Emissionen gezählt, um die Schädigungsprozesse, die vor dem katastrophalen Bruch innerhalb der Schneeprobe stattfanden, abschätzen zu können.

Beide Arten von Experimenten zeigten das erwartete verformungs- bzw. belastungsgeschwindigkeitsabhängige Verhalten von Schnee. Die Scherverformung

war konstant über die Probenhöhe bei homogenen Proben. Innerhalb geschichteter Proben konnte eine starke Konzentration von Scherverformung bei der Schwachschicht beobachtet werden, während die Schichten darüber und darunter praktisch keine Verformung zeigten. Diese Konzentration von Scherverformung rechtfertigt die üblichen Modellannahmen von starren Schichten über und unter der Schwachschicht. Zusätzlich suggeriert sie, dass in Schwachschichten katastrophale Brüche passieren können, da dort die lokale Verformungsrate gross sein kann, trotz kleiner Verformungsrate der gesamten Schneedecke.

Kraftkontrollierte Belastungsexperimente mit einer Oberflächenreifschicht zeigten, dass die Festigkeit der Schicht abnahm mit zunehmender Belastungsgeschwindigkeit und zunehmendem Neigungswinkel. Zweiteres illustriert das anisotrope Versagensverhalten von Oberflächenreif, er ist schwächer in Scherung als in Kompression. Für Schneebrettauslösung in der Natur bedeutet diese Abnahme von Festigkeit mit zunemendem Neigungswinkel, dass Schädigungen in der Schwachschicht und damit Lawinenentstehung in steilerem Gelände wahrscheinlicher sind, dies stimmt mit Beobachtungen überein.

Chapter 1

Introduction

Snow comes to the mountains every winter and with snow come avalanches. The earliest reportings on avalanches date back to the time between the 12th and 14th century. During this period the Walser and the Alemani starting settling in even the remotest valleys of the European Alps in search of new living space (Ammann et al., 1997). The settlers were forced to live with natural hazards like mud flows, rockfalls, floods, landslides, and avalanches, the last being the subject of this thesis. Figure 1.1 (ETH picture archive) shows the reproduction of a copper engraving of an avalanche from the 18th century. People then pictured an avalanche as a ball of snow coming down from the mountains. Nevertheless they already realized that avalanche danger increases if they cut down too much forest. In the 19th century people started building the first avalanche defence structures using wood and stones. The destruction caused by avalanches could be greatly reduced since then, but it is still not possible to eliminate avalanche danger and destruction or loss of lives caused by avalanches completely. Avalanches can still not be predicted in time, only an estimate of the regional danger for avalanches can be given.

Figure 1.1: Avalanche.

Avalanches do not only threaten infrastructure like roads, railways, or buildings but also the increasing number of recreationists spending their time in snow-covered mountainous areas. On average, 25 people die of avalanches per year in Switzerland, 90% of these

Figure 1.2: The two main types of avalanches. Left: Point release avalanches. Right: Slab avalanche. Photos: C. Mitterer and R. Pajarola.

fatalities can be attributed to skiing or snowboarding beyond controlled ski runs (Tschirky et al., 2001).

The aim of the WSL-Institute for Snow and Avalanche Research (SLF) is to increase and improve the prevention and the knowledge of the physical and mechanical processes involved in avalanche formation. The present thesis is a contribution to studying the fracture nucleation process for dry-snow slab avalanches.

1.1 Snow avalanche formation

There are two kinds of snow avalanches, loose snow avalanches (Fig. 1.2a) and slab avalanches (Fig. 1.2b) (e.g. McClung and Schaerer, 2006). Loose snow avalanches form in relatively cohesionless snow. They start at a single point at the snow surface and pick up more snow and grow wider as they move down the slope. Loose snow avalanches are comparable to the slip of sand or other granular materials. Slab avalanches start moving down the slope as a cohesive slab, which breaks into single pieces on its way down the mountain. A prerequisite for a slab avalanche release is a weak layer beneath the amply cohesive slab.

Slab avalanches are more dangerous than loose snow avalanches for several reasons. They are harder to predict, there is less time of warning since they arrive without noticeable precursors, and they usually involve larger snow masses and higher speeds. Jamieson

Figure 1.3: A buried surface hoar layer in a natural snowpack. Photo: J. Schweizer.

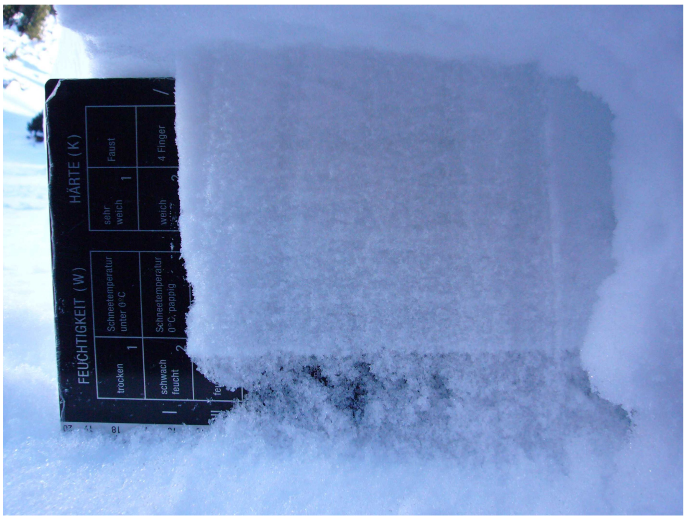

Figure 1.4: A depth hoar layer in a natural snowpack.

and Johnston (1992) found that 99% of the fatal avalanche accidents in Canada between 1972 and 1991 were caused by slab avalanches. Slab avalanches can further be divided into wet and dry-snow slab avalanches. In the European Alps wet snow avalanches occur mainly during the spring when temperatures are rising. Dry-snow slab avalanches on the other hand may occur throughout the winter season. In this thesis we concentrate on the formation of dry-snow slab avalanches.

Most (80%) dry-snow slab avalanches release on either a surface hoar (Fig. 1.3), a depth hoar (Fig. 1.4), or snow layer consisting of faceted crystals (Schweizer and Jamieson, 2001). Figures 1.5 and 1.6 show the crown fractures of dry-snow slab avalanches which released on layers of surface hoar.

Figure 1.5: Crown fracture of a dry-snow slab avalanche which released on a layer of surface hoar and was triggered by skiers. Photo: R. Pajarola

1.2 Experiments on snow failure

In order to grasp the mechanisms behind avalanche release, snow as a material and in particular the failure behaviour of snow has to be understood. The first and most obvious approach for understanding snow failure is performing deformation and loading experiments with snow, either in the field or in a cold laboratory.

Field measurements of strength in weak snow layers or snow layers in general show large scatter in the results (Föhn et al., 1998; Jamieson and Johnston, 2001) because the mechanical properties of snow depend on microstructural characteristics which are variable both in space and time. This impairs the reproducibility of experiments performed at different times even at the same snowpack location.

As monitoring the initiation process for dry-snow slab avalanches in the field is very challenging due to the inhomogeneity of snow (e.g. van Herwijnen and Schweizer, 2008), a sim-

Figure 1.6: Huge crown fracture of a dry-snow slab avalanche which released on a layer of surface hoar and was artificially triggered by explosives. Photo: P. Müller

pler approach is to study it experimentally in a cold laboratory. Displacement-controlled shear experiments give insight into the material behaviour and material characteristics before failure. The results of the displacement-controlled experiments can be compared to the results of shear experiments with other materials, and if interpreted with care, the conclusions for materials with similar shear properties or from modeled results might be conveyed to snow. We performed direct displacement-controlled shear experiments with a linear friction tester (LFT), which was already available at the SLF. For directly studying failure, load controlled experiments are needed, which we performed with a new loading apparatus especially designed for studying the failure of snow with respect to avalanche release. In this apparatus the snow samples are loaded via the gravitational force. This gives a natural combination of shear and normal load depending on the 'slope angle'.

1.3 Modelling snow failure

Snow is a sintered material, which consists of an ice matrix with open pores filled with air and water vapour. During snow deformation (snow density $\sim$ 300 kg m^{-3}), the microstructure (and hence the bulk mechanical properties) continuously changes because of the rearrangement of single snow grains (Camponovo and Schweizer, 2001). In other words, bond breaking repeatedly has to occur. On the other hand, two snow grains which come into contact may easily bond to each other, since snow in a natural snow cover exists close to its melting point. The failure process preceding avalanche release is therefore believed to be related to two fundamental, but competing processes at the micro-scale: bond fracturing and sintering (bond formation) (Schweizer, 1999). We therefore model snow failure with a fibre bundle model (FBM) were the snow grains are represented by fibres which may break and re-sinter.

1.4 Research objectives

We want to understand the failure of snow. In particular, we are interested in how a failure within a weak layer forms since the development of a failure in a weak layer is a necessary condition for slab avalanche release. We therefore want to monitor the failure behaviour of snow samples containing a weak layer during displacement-controlled shear experiments and force-controlled experiments. The observed failure behaviour described in terms of bond breaking and sintering are modeled.

To reach our goal, the following tasks and objectives are defined:

1. Model the failure of snow under shear.

2. Develop a loading apparatus where snow can be loaded under nature-like but controlled laboratory conditions.

3. Perform displacement-controlled shear experiments and loading experiments with snow samples containing a weak layer in order to assess the failure properties of weak snow layers.

4. Perform acoustic emission measurements during these shear experiments to assess the breaking of single bonds within the snow structure.

5. Obtain deformation patterns from photographs or high-speed videos from deformed snow samples.

6. Compare the microstructure from snow samples obtained from μ-CT images to the macroscopic failure behaviour and find a relation between them.

7. Compare the model output with the experimental results and obtain new insights about the microscopic properties of snow.

Chapter 2

Present state of research

2.1 Dry-snow slab avalanche release

Dry-snow slab avalanches involve the release of a cohesive slab over an extended plane of weakness. A slope parallel crack below the slab spreads along this plane of weakness (weak layer or weak interface within the snowpack), and if the weight of the now unsupported slab is high enough, a tensile crack develops upslope and on the flanks of the slab and an avalanche releases (McClung and Schaerer, 2006; Perla, 1980). The current perception of slab release is that the primary failure is between the slab and the substratum, either in slope-parallel shear or due to a compressive failure which leads to loss of shear support (McClung, 1987). The slab avalanche is a result of a failure and fracture process that covers a wide range of scales: from the scale of the bonds between snow crystals to the scale of an avalanche slope. According to a conceptual model, slab release starts with a damage process that leads to a localized failure which will grow and when reaching critical size will eventually rapidly propagate below the slab so that it becomes – after a tensile crack at the top – fully detached and releases (Schweizer et al., 2003) (Fig. 2.1). Therefore, a comprehensive model of slab release should include (1) snow failure (damage) leading to failure initiation and (2) fracture propagation.

Recent studies on crack propagation (McClung, 2005; Sigrist and Schweizer, 2007) found that the material properties of the weak layer as well as the properties of the slab play an important role for crack propagation. It was found that bending of the slab due to a

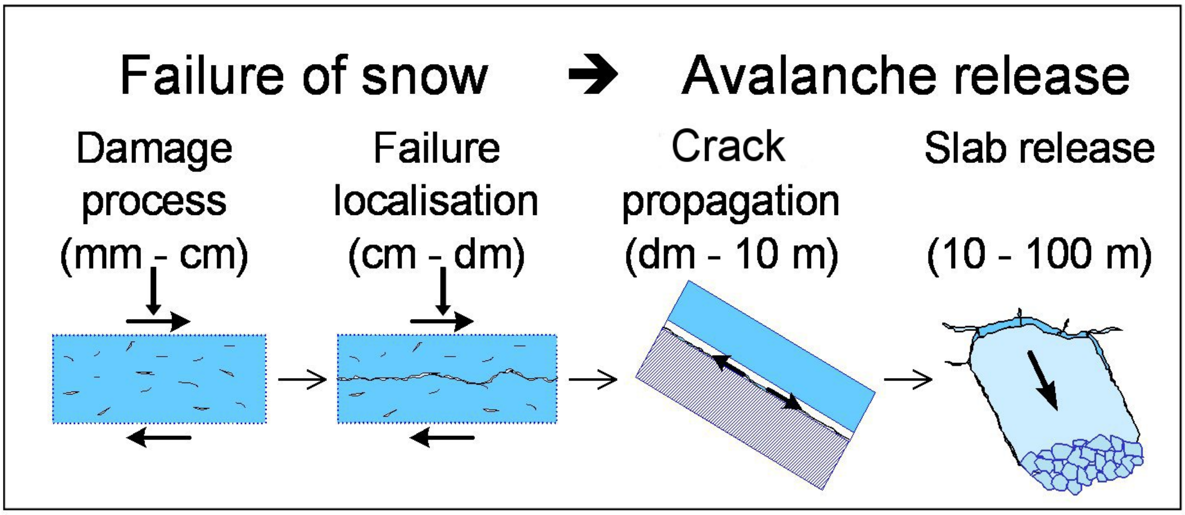

Figure 2.1: Conceptual model of dry-snow slab avalanche release (from Schweizer et al., 2003).

slope normal collapse of the weak layer can supply a substantial amount of energy to the fracture process. The formation of the initial failure is only documented in the case of artificially triggered dry-snow slab avalanches (e.g. van Herwijnen and Jamieson, 2005). The initiation process for spontaneous dry-snow slab avalanches remains unclear and is the subject of the present thesis.

Several factors contribute to snow avalanche formation. The five most relevant contributing factors are terrain (a slope angle of 30° or more favours avalanche formation), precipitation (snowfall and, occasionally, rain), wind, temperature (including radiation effects), and the snow cover (see Schweizer et al., 2003). The nomenclature for a slab avalanche is depicted in Figure 2.2. As mentioned before the presence of a weak layer is a necessary but not sufficient condition for slab avalanche formation (Bader and Salm, 1990). Additionally, the slab (snow layer(s)) above the weak layer needs to be sufficiently hard and cohesive in order to enable crack propagation, and for the avalanche to actually start moving down the mountain, the slope has to be steep enough since the friction between the slab and the bed surface needs to be overcome (van Herwijnen and Heierli, 2009).

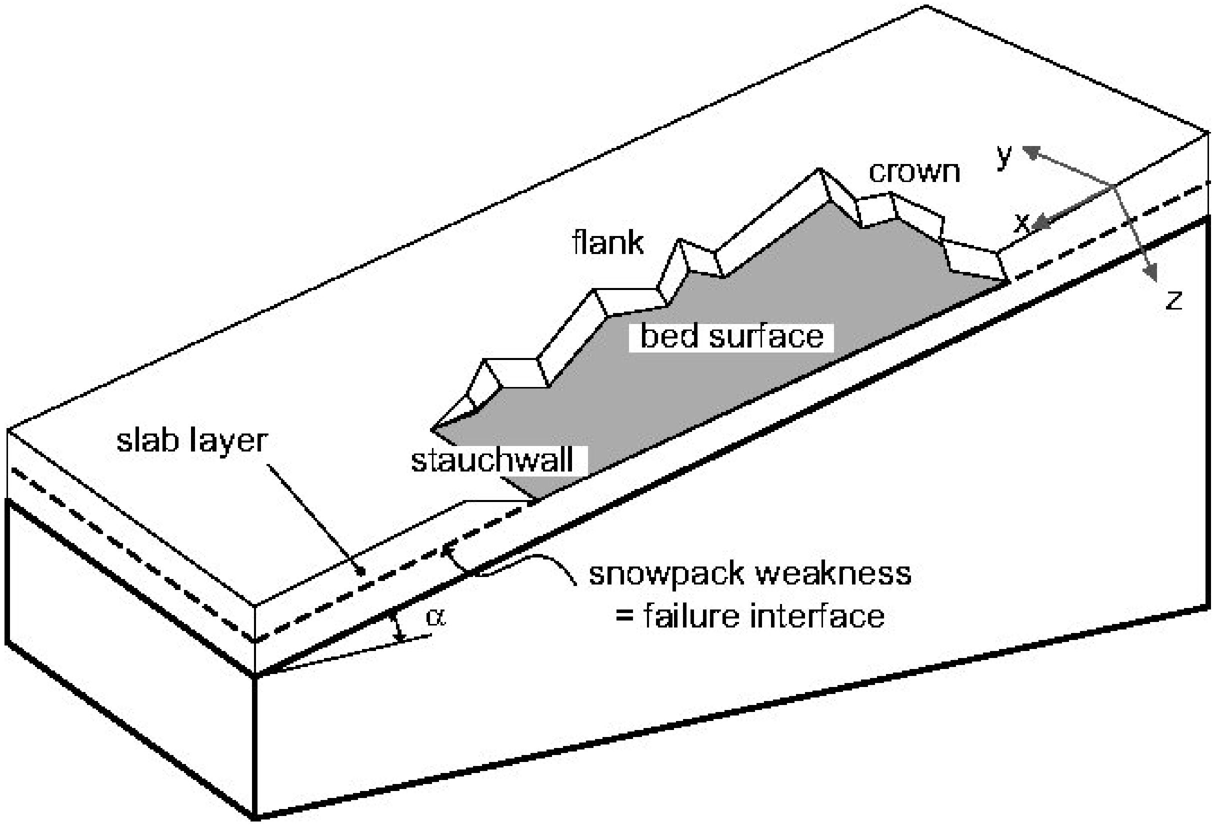

Figure 2.2: Schematic of a slab avalanche release (from Schweizer et al., 2003).

2.2 Snow microstructure and properties

Snow crystals form in the atmosphere by deposition of water vapour onto small particles or by accretion of super-cooled water droplets. Different shapes of crystals result from variations in temperature and supersaturation in the atmosphere (McClung and Schaerer, 2006). The most common form of crystals during snow fall events are stellar crystals with six arms (Fig. 2.3a).

Once the snow crystals reach the ground, they start bonding to each other and changing their forms. In the case of an alternating temperature gradient (Pinzer and Schneebeli, 2009) or constant temperature, freshly fallen dry snow will begin to decompose into rounded crystals (Fig. 2.3b). The initial forms – usually dendritic – change into smaller particles, to reduce their specific surface, followed by the slow growth of larger particles at the expense of the smaller particles. This happens because the water vapour pressure is higher at points of high curvature of the surface. This process, called rounding

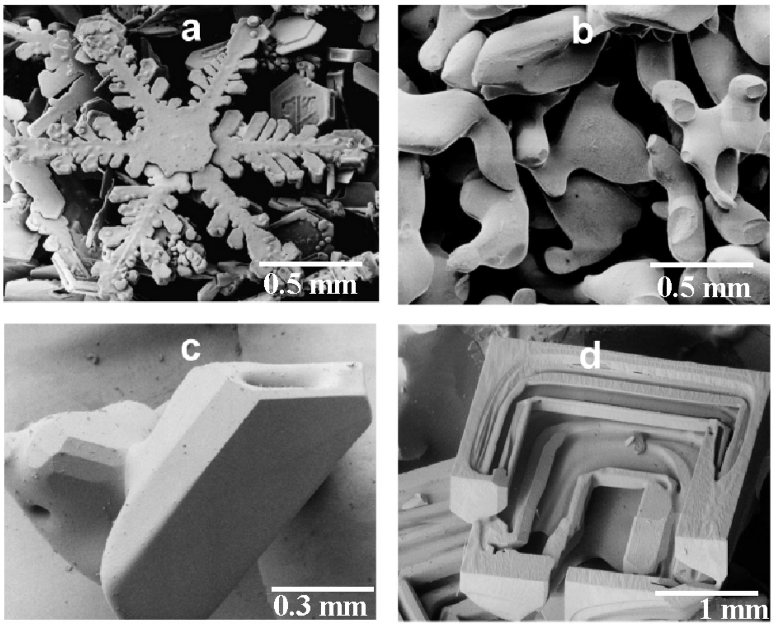

Figure 2.3: Examples of snow crystals: a. Stellar snow crystal, b. Rounded snow crystals, c. Faceted snow crystal, d. Depth hoar. Low temperature scanning electron microscope images from http://emu.arsusda.gov/

metamorphism, is associated with intergranular bonding and the gain of strength (Perla and Sommerfeld, 1987). Usually, equilibrium metamorphism increases the stability of the snowpack.

Repeated snowfalls throughout the winter produce a layered snowpack, which may vary strongly in time and also space. Gravity leads to settlement of the snowpack and thus densification of the snow layers.

We can differentiate between wet and dry snowpacks. A snowpack is considered as wet if liquid water is present. This can only happen if the snowpack is isothermal, i.e. at 0 °C. In this thesis, we only consider dry snowpacks.

Weak layers in dry snowpacks may form either on the surface (surface hoar) or within the snowpack (depth hoar). On cold, clear nights, the cooling of the snow surface due to radiation may lead to a condensation of water vapor on the snow surface producing surface hoar crystals (McClung and Schaerer, 2006). These crystals are relatively large (Fig. 2.4) and hardly show any lateral bonding to each other. When buried by a subsequent snowfall layers of surface hoar may remain weak for a long time and often play an important role in slab avalanche formation (Schweizer et al., 2003). In Figure 2.4 (b) a buried surface

hoar layer is shown that is fractured on the left side of the photograph. Depth hoar and faceted crystals form due to faceting metamorphism. Faceting metamorphism usually occurs when the temperature gradient is greater than about 10 °C m^{-1} (Akitaya, 1974) and stays constant in direction. Faceting metamorphism requires a stationary vapour diffusion field (M. Schneebeli, personal communication). Such a 'stable' diffusion field causes water vapour to move from the 'warm' surface of one snow crystal to the 'cold' surface of another crystal, usually upward through the snowpack. One should not imagine a global transport of water vapour through the whole snowpack though, it is rather a direct transport from one snow grain to another. The water vapour is deposited as ice on the cooler surface of crystals, normally the bottom. Larger grains grow at the expense of smaller ones. Typically, decomposed fragments or rounded grains will grow into faceted crystals, characterized by flat faces and angular crystals (Fig. 2.3c). If the strong temperature gradient persists, depth hoar, consisting of larger striated or hollow crystals, will form (Fig. 2.3d). At typical densities, faceting metamorphism does not promote intergranular bonding and is therefore often associated with loss of strength.
Both rounding and faceting metamorphism are caused by water vapour transport within the snowpack. In both cases the water vapour transport is caused by a difference in vapour pressure. For the rounding metamorphism this difference in vapour pressure is due to alternating or small temperature gradients (Pinzer and Schneebeli, 2009), while huge temperature differences are the driving factor for faceting metamorphism. Rounding metamorphism usually increases the snowpack stability while faceting metamorphism decreases stability and even causes the formation of weak snow layers.
In the following, the most relevant microstructural and mechanical properties of snow will be described.

- **High temperature dependence:** The temperature of seasonal snow on the ground is usually close to its melting point, this means that its homologous temperature (actual temperature divided by melting temperature on the Kelvin scale) is high (i.e 0.9 . . . 0.95). This implies a strong temperature dependence of the mechanical properties of snow and emphazises the importance of using a cold laboratory where temperature conditions can be controlled.

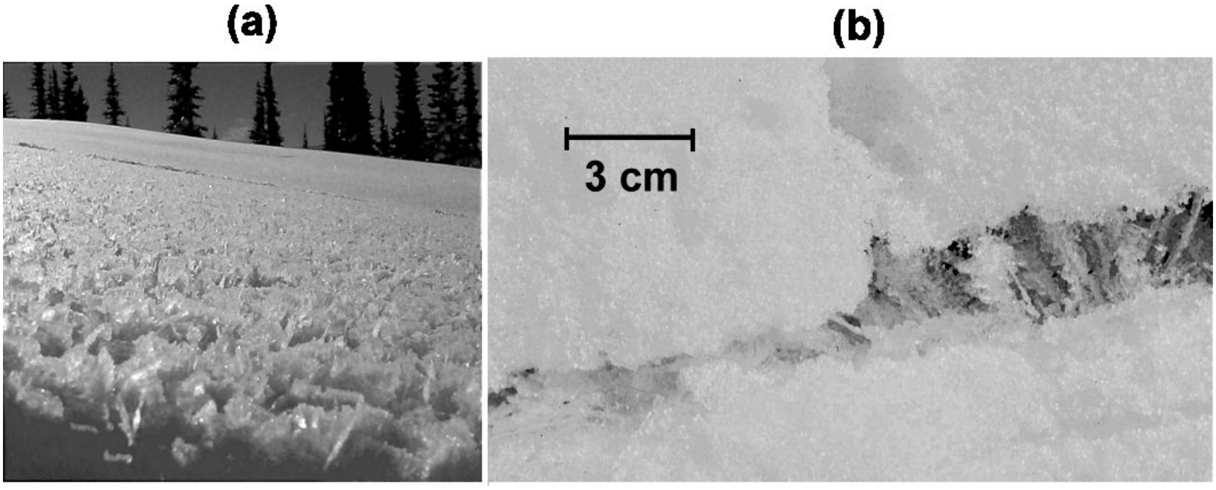

Figure 2.4: Surface hoar produces persistent weak layer. (a) Surface hoar crystals on the snow surface (Applied Snow and Avalanche Research University of Calgary (ASARC) photo). (b) A weak layer of buried surface hoar crystals that partly fractured (photo from Jamieson and Schweizer (2000)).

In engineering materials, the temperature region $T > 0.6 \cdot T_{\mathrm{m}}$, where T is the actual temperature of the material and T_{m} the melting temperature, is considered as a region where the material is 'unable to bear engineering loads in a structure' (http://www.ami.ac.uk/courses/topics/0164_homt/index.html). In this sense, snow is actually surprisingly strong!

- **Sintering:** As soon as two snow grains come into contact with each other, they start bonding (or sintering) to each other (Szabo and Schneebeli, 2007; Gubler, 1982). Snow (ice) is probably the only natural material that sinters with a very low external force. This effect is a result of the high homologous temperature. Its consequence is that if snow fractures and the two resulting pieces are not separated, they will sinter again. This makes pre-catastrophic fractures in snow hard to detect.

- **Complex microstructure:** Snow consists of an ice-matrix filled with air and water vapour (Figs. 7.4 and 7.3). Snow at 0 °C can also contain liquid water. New (freshly fallen) snow can have densities of as low as 60 kg m^{-3}. Well settled snow may reach densities of 550 kg m^{-3}, above this density one speaks of firn. Ice has a density of 917 kg m^{-3}, this means that snow has a high porosity, ranging from 95% to 40%. Kirchner et al. (2000) therefore interpreted snow as a foam of ice and

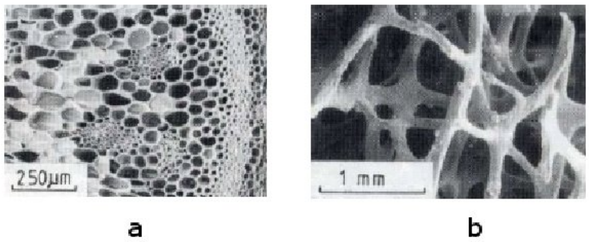

Figure 2.5: Two examples of cellular materials: a) Stem of a plant. b) Bone (from Gibson and Ashby, 1997).

used the theory of cellular materials of Gibson and Ashby (1997) for snow. Unlike other cellular materials like wood, bone (Fig. 2.5), or industrial foams, snow contains many structural elements freely protruding into space and thus not contributing to snow strength. This leads to the fragile nature of snow and its low tensile strength of 0.5-200 kPa (bone: 2'000-20'000 kPa, wood: 70'000-100'000 kPa).

- **Ductile-to-brittle transition:** The failure behaviour of snow under loading or deformation is highly dependent on the loading or deformation speed. For fast loading or for high strain rates ($\dot{\epsilon} > 10^{-3}$ s^{-1}) snow exhibits brittle behaviour, while it reacts to low loading or deformation rates in a ductile manner (Fig. 2.6). In the following we use the terms ductile and brittle as described in Narita (1983) and commonly used in ice mechanics (Petrenko and Whitworth, 1999). Brittle failure behaviour means that virtually none or very little permanent deformation occurs before fracture. Ductile behaviour implies large irreversible deformation before failure or no failure at all.

- **Dependence of the macroscopic mechanical properties on the microstructure :** The macroscopic mechanical properties of snow depend strongly on the microstructure (form, arrangement, and size of grains and bonds) which can be substantially different for different snow types of the same density (McClung and Schaerer, 2006; Mellor, 1975; Keeler and Weeks, 1968), e.g. the shear strength of two snow samples with the same density but different microstructure can vary by a factor of five or more. Here the term macroscopic refers to length scales of $\mathcal{O}(10^{-1}$ m) and larger, while microscopic describes length scales of about $\mathcal{O}(10^{-4}$ m) (size

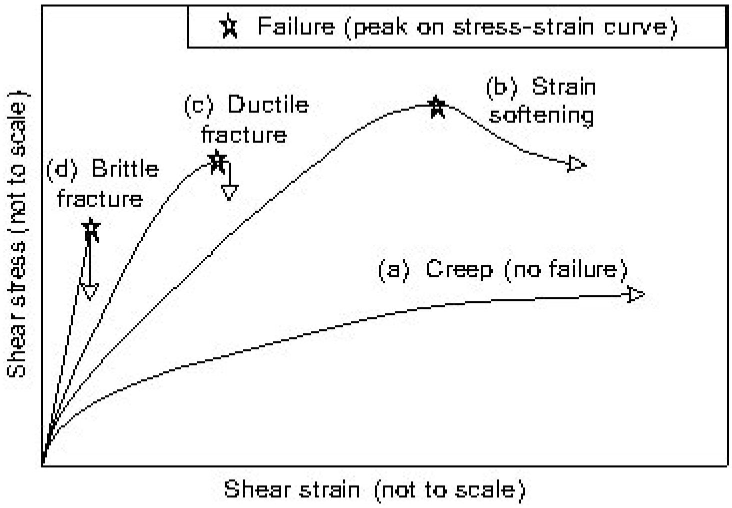

Figure 2.6: Schematic of failure behaviour of snow under shear at different shear strain rates (from Schweizer et al., 2003). Note that the strain rate increases from a to d, i.e. $\dot{\epsilon}_a < \dot{\epsilon}_b < \dot{\epsilon}_c < \dot{\epsilon}_d$.

of snow grains and bonds).

2.3 Mechanics of snow deformation and failure

Snow deformation and failure are highly rate and temperature dependent. This has been demonstrated with tension tests (Narita, 1980, 1983). The mechanical behaviour of snow under compression has recently been revisited and described by a series of papers (Scapozza and Bartelt, 2003; von Moos et al., 2003). In shear, strength decreases with increasing strain rate and temperature. The ductile-to-brittle transition occurs at a strain rate at about $10^{-4} - 10^{-3}\mathrm{s}^{-1}$, depending on temperature and pressure (Fukuzawa and Narita, 1993; Schweizer, 1998; McClung, 1987).

Whereas in other materials the relation between microstructure and mechanical properties has been intensively studied and a deeper understanding of the effects of disorder on this relation has been developed (Duxbury, 1990), for snow, this relation is still lacking.

Failure in quasi-brittle materials – snow has been proposed as being quasi-brittle (Bažant et al., 2003) – occurs often because of the localization of cracking. In these heterogeneous materials, distributed cracks (micro-cracks) develop almost homogeneously and concentrate progressively in order to form a macro-crack, which propagates suddenly while other micro-cracks do not. Distributed cracking is often described in continuum mechanics with damage models (Delaplace et al., 1996). The observed decrease in stiffness during deformation, which is also observed for snow, is attributed to the creation of micro-cracks. These small defects cause a decrease of the effective cross section and lead to an increase of the effective stress (Roux, 1990). Monitoring porosity often allows to assess the degree of damage.

In the case of snow, it is assumed that during the deformation process, broken bonds may re-bond (sinter) and the strength loss might be compensated - depending on the deformation rate. Sintering during shear deformation has been proposed by de Montmollin (1982). Gubler (1982) designed an experiment to study the strength of bonds between ice grains after short contact times. These results give the idea that fast sintering gives some initial strength. Under loading conditions sintering can even happen within less than a second (Szabo and Schneebeli, 2007).

Within this thesis, we use the definition of simple shear, $\epsilon_{\text{simple}} = \frac{\text{deformation}}{\text{original length}} = \frac{\partial u_x}{\partial y}$, see Figure 2.7, as is common in Geology and also snow mechanics (Schweizer, 1998). In engineering another definition of shear is common, namely the definition of pure shear, $\epsilon_{\text{pure}} = \frac{1}{2}\left(\frac{\partial u_x}{\partial y} + \frac{\partial u_y}{\partial x}\right)$. It can be seen that for $\partial u_y = 0$, $\epsilon_{\text{pure}} = \frac{1}{2}\epsilon_{\text{simple}}$.

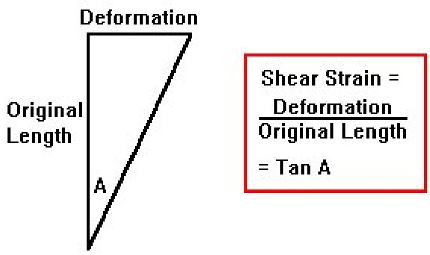

Figure 2.7: Definition of simple shear.

2.4 Experimental studies on snow failure and fracture

The 'golden age' of snow mechanics was in the 1960ies and the 1970ies (Shapiro et al., 1997). In Europe and Japan scientists concentrated on research concerning avalanche formation in mountainous areas. In North America and the former Sowjetunion focus was put on activities in the polar regions. Even earlier, in the 1930ies, loading experiments with snow were performed in order to assess the constitutive equations of snow (Haefeli, 1967; Bader et al., 1939). Scientists and engineers wanted to be able to calculate the forces on buildings and structures due to snow loading.

Previous modern studies on the mechanical behaviour of snow mainly used displacement-controlled shear experiments. Most experiments were made with homogeneous snow (e.g. Schweizer, 1998; McClung, 1987; de Montmollin, 1982), only in two studies layered samples including a weak layer were tested under controlled laboratory conditions (Fukuzawa and Narita, 1993; Joshi et al., 2006).

The deformation of snow in terms of a structural mechanism was studied by St. Lawrence and Bradley (1975); Mellor (1975); Wakahama (1967). Within these studies the deformation of snow was related to five mechanisms: breaking of bonds between grains, sintering of bonds between grains, grain boundary sliding (or grain re-arranging), and the plastic deformation of grains. It was found that the deformation mechanisms of snow depend strongly on the deformation speed and on the snow microstructure, and at the same time the snow microstructure constantly changes during deformation.

Displacement-controlled experiments give insight into the material behaviour before fracture. However, to study fracture itself, and in particular the processes that lead to fracture, load-controlled (or force-controlled) experiments are needed. Camponovo and Schweizer (2001) performed stress-ramp experiments with homogeneous snow with a rheometer, where the snow samples were sheared by rotation. These experiments showed that sintering of snow continuously occurred during the experiments, and only at a high applied stress did the damage process exceed the healing process. The only other modern load-controlled shear experiments, to our knowledge, were performed just recently by Podolsky et al. (2008) who pulled a shear frame on a horizontal snow sample with constantly increasing force. They found that snow strength dramatically decreased with increasing loading rate.

Since for layered snow the deformation (strain) during loading is assumed to be concentrated in the weak layer or at least to be unequally distributed within the snowpack (McClung, 1987), monitoring the displacement field within a layered snow sample is crucial for understanding the failure behaviour. Under the assumption of plane strain, one option to achieve this is monitoring the displacement field on the side of the snow sample, since the displacement field on the side of a sample can be assumed to be representative for the displacement (and thereby deformation) field within the sample. In order to measure displacement fields on snow, particle image velocimetry (PIV) has proven to be a suitable technique since it is non invasive and snow can be, depending on the snow type, very fragile. PIV was already used by Gleason (2004) who measured the deformation on snow under compression. Borstad and McClung (2008) combined high speed video images with a particle tracking software to analyze three-point-bending tests with snow specimens, while van Herwijnen and Jamieson (2005) used this combination to study crack propagation in weak snowpack layers in the field. The idea of marking snow and monitoring the displacement of the marks had been used even earlier by Yosida (1963) who analyzed the deformation within snow in a semi-quantitative manner.

One method to assess the processes leading to catastrophic failure (breaking of bonds, generation of micro-cracks) are acoustic emission (AE) measurements. In ice, AE were related to fracture by e.g. Cole and Dempsey (2004), who studied the breakup of sea ice. Sommerfeld and Gubler (1983) were the first to measure acoustic emissions in snow and relate them to avalanche release. They performed field studies and focused on low frequency sensors with frequencies of the order of 100 Hz because of the strong attenuation of high frequencies in snow. McClung (1987) measured acoustic emissions during slow deformation-controlled shear experiments (without catastrophic failure) in the laboratory, in the frequency range of several Hz to several kHz. He found no acoustic emissions during slow shear tests, and for fast tests the acoustic emissions increased with stress. He suggested that acoustic emissions were associated with slip surface formation, but mentioned explicitly that there was no proof for this assumption. Scapozza et al. (2004) measured acoustic emissions during triaxial compression tests, finding that for ductile failure behaviour the AE rate initially increased but decreased after the yield point. St. Lawrence (1980) considered snow as ice with a low density and hypothesized that the acoustic sources in snow were the same as in ice, namely the breaking of ice crystals or bonds between crystals.

2.5 Modelling snow failure

2.5.1 Models on interface failure

The failure behaviour of homogeneous materials and layered materials is substantially different. Whereas crack propagation in homogeneous materials is normally not restricted to a defined direction, in layered materials cracks usually propagate along the interfaces between two layers. Due to this restriction considerably different loading situations can occur. It is known that mode II (shear) experiments in homogeneous experiments are difficult to perform, since cracks tend to change direction, resulting in a pure mode I (tension or compression) situation (Anderson, 1995). In layered materials, on the other hand, mode II fractures occur frequently (Suo and Hutchinson, 1989).

Many research areas dealing with modern layered materials such as laminates, fibres, and composites apply concepts of interfacial fracture mechanics. Also natural processes like the icing of electrical transmission cables (ice/metal interface) have been treated within this framework (Wei et al., 1996). Since snow is a layered material as well, the application of interfacial fracture mechanics for studying crack propagation suggests itself, and was proposed by Schweizer and Jamieson (2001).

In the classic paper of Palmer and Rice (1973) the mechanism of progressive failure by slip surface propagation was introduced in connection with instabilities of clay slopes. It is based upon concepts of the Barenblatt model of fracture mechanics. McClung (1979) discussed the application of concepts from the Palmer and Rice model for the case of the snow slab in detail. McClung (1981) investigated fracture geometry, time scale of release, and temperature effects and could show that they are consistent with the known facts of dry slab avalanche release.

2.5.2 Mircrostructural modelling of snow failure

To model snow deformation and failure both the microstructure and the disorder of snow need to be considered. There exist several mechanical snow models that have included the microstructure in some way. These models can be divided into three different groups: (1)

There are models which are essentially continuum models but include some parameterization of microstructure (e.g. Mahajan and Brown, 1993). This approach has been used to describe snow viscosity (Bartelt and von Moos, 2000) and to simulate the mass and energy balance of the snow cover (Lehning et al., 2002). Also the model by Gibson and Ashby (1997), where snow is considered as an open cell foam of ice with two structural parameters (beam length and beam cross section), belongs to this group. Louchet (2001) followed their approach and considered healing using rate equations for bond rupture and bond formation. (2) Models that try to reproduce the microstructure in simplified (or generalized) form, for example as arrangement of beams (or spheres), possibly with some random variations of the local properties from one element to the next (Herrmann and Roux, 1990). Fibre bundle models (FBM) belong to this class of model. Johnson (1998) used a dynamic finite element computer program to study the rapid compaction of snow represented as an arrangement of randomly distributed spheres. (3) With new experimental techniques, such as CT measurements, the full 3D representation of microstructure is used as input for a real microstructural (or specimen specific) finite element model (Schneebeli, 2004).

A modelling approach which considers disorder – although on a macroscopic scale – was used by Fyffe and Zaiser (2004) who introduced time-dependent strength recovery and randomly varying shear strength into a model of snow slope failure.

Fibre bundle models (e.g. Daniels, 1945; Alava et al., 2006; Raischel, 2006) are statistical fracture models that can include a simple representation of the microstructure of porous, granular materials (see Kun et al. (2006) for a detailed description). They are especially helpful in describing materials with time dependent failure effects, for example the fatigue failure of asphalt (Kun et al., 2007). As such, the FBM technique allows simulating the important ductile-to-brittle failure transition of snow as well as competing micro-scale processes such as bond fracturing and sintering (Schweizer, 1999).

The FBM used within this thesis is based on the fracturing and sintering of bonds between grains.

Chapter 3

Modelling snow under shear deformation with a fibre bundle model

3.1 Introduction of the fibre bundle model

Three dimensional images of snow microstructure (e.g. Schneebeli, 2004) clearly show that snow is a highly disordered material consisting of an ice matrix and open pores filled with air and water vapour. The degree of heterogeneity is supposed to affect failure initiation at various scales (e.g. Schweizer et al., 2003). Continuum (macroscopic) quantities like global stress, global strain, and global strength are not evenly distributed over all microstructural elements of the snow structure. We assume failure to start where the the stress within the snow structure exceeds the local strength. Accordingly, the strength distribution is expected to play a major role in the failure process.

On an inclined slope the gravitational force induces shear and normal deformation in the snowpack. As we will see in our experiments (see section 7.4), shear deformation is concentrated in the weak layer.

In this thesis, we apply a fibre bundle to simulate snow deformation, damage, and failure of a weak snow layer. The aim is to investigate the influence of micro-structural parameters on the bulk mechanical response of weak snow layers under shear loading. In particular, the hypothesis is tested that different time scales of fracturing and sintering of bonds (Fig.3.1) explain the strain-rate dependence of the failure behaviour of snow (Schweizer,

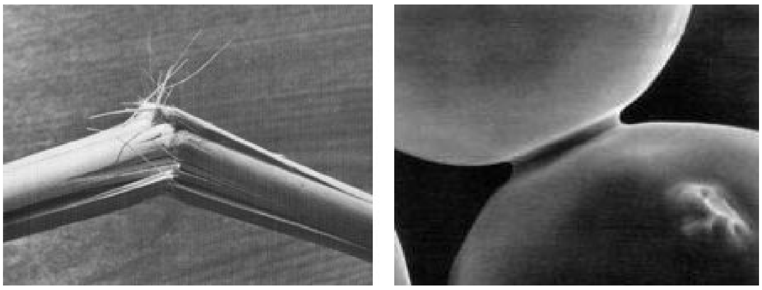

Figure 3.1: The basic idea behind the fibre bundle model: to describe the macroscopic behaviour as a competition between the microscopic processes of the breaking and sintering of bonds between grains during snow deformation. Images from http://bambus.rwth-aachen.de/eng/reports/mechanical_properties/referat2.html and http://www.mpip-mainz.mpg.de/documents/akbu/pages/particles.htm.

1999). The experimental results of snow under shear deformation of Schweizer (1998) are used for comparison with the model output.

The model and the results presented in this chapter have been published previously in Reiweger et al. (2009b). Moreover, Kornél Kovács, a fellow PhD student, found a semi-analytic solution to our model (Kovacs et al., 2010).

3.2 Methods of the fibre bundle model

In this modelling approach, the snow crystals (e.g. buried surface hoar) that form the weak layer correspond to fibres (Fig. 3.2). The fibres are located between two rigid plates which represent the slab above and the substratum below the weak layer. Since the layers above and below are substantially stronger and about an order of magnitude stiffer than the weak layer (Fukuzawa and Narita, 1993; Jamieson and Schweizer, 2000), the simple assumption of rigid plates is justified as a first approximation.

Each fibre i, where $i = 1, \dots N$, behaves in a perfectly elastic manner. In order to stochastically model the spatial variability of strength which is presumed to be caused by variations in crystal orientation, size, and bonding within the weak layer, the initial strengths $\sigma_{c,i}$ are taken from a Weibull probability distribution, where the density function is given by

$$p(\sigma_{c,i}|\alpha,\beta) = \beta\alpha^{-\beta}\sigma_{c,i}^{\beta-1}e^{-(\frac{\sigma_{c,i}}{\alpha})^{\beta}} \tag{3.1}$$

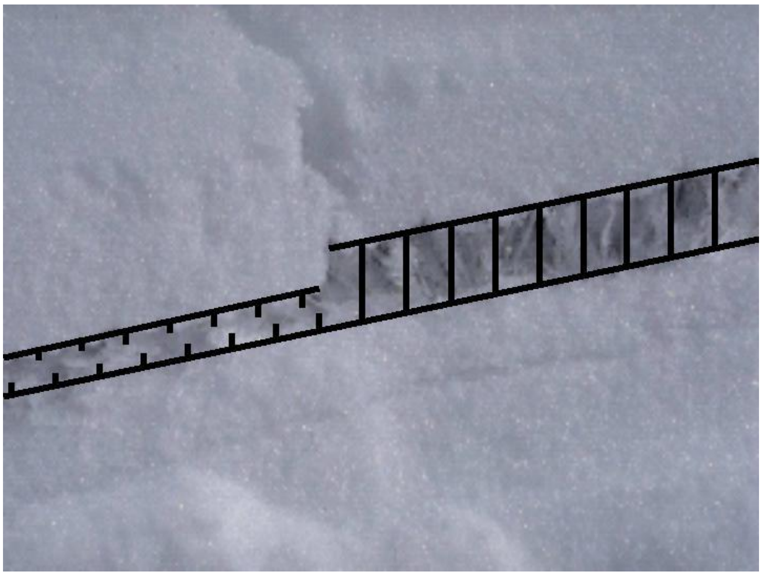

Figure 3.2: Photo of a buried surface hoar layer, fractured on the left, intact on the right. Overlying the photo is a schematic drawing of a bundle of fibres representing the partly fractured weak layer. Photo adapted from Jamieson and Schweizer (2000).

with scale factor α and shape factor β. This is the most commonly used strength probability distribution in statistical fracture models (Herrmann and Roux, 1990; Chakrabarti and Benguigui, 1997) and it has previously been used to describe the strength of snow (e.g. Sommerfeld, 1973; Kirchner et al., 2004). The effect of microstructure is incorporated into the model through this strength distribution.

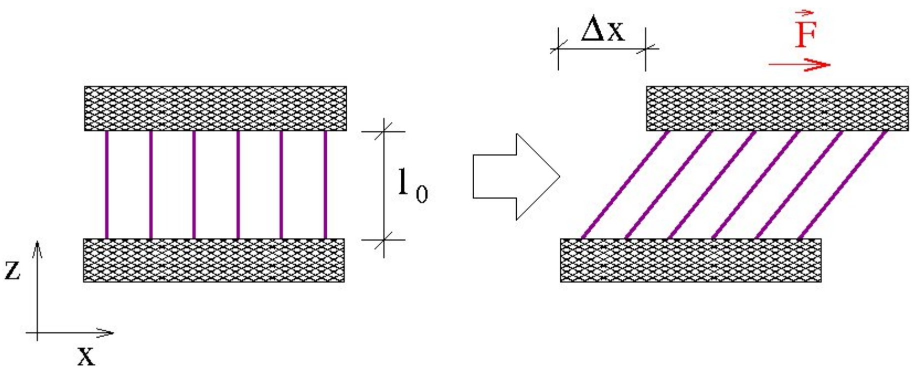

Figure 3.3: Schematic representation of model geometry.

Following the deformation controlled shear experiments mentioned above, at each discrete time step the upper plate is moved along the x-axis by a constant amount (Fig. 3.3). The constant simple global shear strain rate is therefore given by

$$\dot{\epsilon}_{\text{global}} = \frac{1}{l_0}\frac{\Delta x}{\Delta t} \tag{3.2}$$

where l_0 is the initial fibre length (Fig. 3.3).

As a first step we assume no vertical (z-direction) displacement of the upper plate. Furthermore, we treat the fibres as long, thin truss elements under uniaxial tension, i.e. shear deformation and bending within a fibre is neglected. Within this concept, we regard the fibres as long thin bars which can only be loaded in tension. In a later version of the model a more complex failure behavior of the single fibers might be considered. This would include shearing and bending. As a first step, shearing can be disregarded for small deformations. Bending is a macroscopic phenomenon which can also be disregarded for a first approximation. The whole bundle undergoes a shearing deformation, i.e. the upper plate moves within a plane normal to the initial direction of the fiber axes. This is very important for our concept of sintering - broken fibers stay close to each other which enables sintering.

Since the simple shear deformation of the (stiff) upper plate is imposed, the load on a single fibre is always given by the external deformation, no matter how many fibres are intact. The fibres break in order of increasing strength as determined by the Weibull distribution applied to each fibre, i.e. the weakest fibres break first. The elongation Δl of a fibre can be calculated via

$$\Delta l = \sqrt{l_0^2 + (m\Delta x)^2} - l_0 \tag{3.3}$$

where m is the number of time steps the fibre has been intact. The force $f_j(t)$ to deform a single fibre is

$$f_j(t) = \sigma_j(t)a = E\epsilon_j(t)a, \tag{3.4}$$

where $\sigma_j(t)$ is the stress the fibre experiences, E is the elastic modulus, a is the cross section of the fibre, $j = 1, \ldots N_{\text{intact}}$ with N_{intact} the number of intact fibres, and $\epsilon_j(t)$ denotes the axial strain of the fibre.

If $\sigma_j(t)$ acting on a fibre reaches its rupture strength, i.e. $\sigma_j(t) = \sigma_{c,j}$, the fibre breaks instantaneously. At the next discrete time step the strength of the fibre $\sigma_{c,j}$ is zero, and the fibre is considered broken. If more than half the fibres are broken we consider the whole bundle as fractured. However, at each time step there is the probability that the broken fibre can start sintering (re-bonding). The sintering probability is proportional to the square of the number of broken fibres, $p_s = p_{\max}(\frac{N_{\text{broken}}}{N})^2$, since two fibre ends are necessary for sintering (second-order kinetics).

We use periodic boundary conditions (PBC). In mathematical models and computer simulations, PBC are a set of boundary conditions that are often used to simulate a large system by modelling a small part that is far from its edge. PBC mean that the finite system is surrounded by identical systems with exactly the same configuration in phase-space. A typical example is the one of a particle enclosed in a box, and we can imagine that this box is replicated to infinity by rigid translation in all the three cartesian directions, completely filling the space. In our case, one can image the bundle in Figure 3.3 to be drawn on a cylinder, and it can be sheared infinitely with the lower and upper plate staying above each other. The PBC seem realistic, since the extension of a snow slope is very large (infinite) compared to the size of a single snow grain. Also for our laboratory samples the snow layer's thickness is small compared to its width and length. As a result of the PBC, the total number of fibres (broken and intact) remains constant and each broken fibre end always has an appropriate partner for sintering, no matter how far the upper plate has already moved.

At each time step a broken fiber may start sintering with probability p_s (a dice is thrown). If a fibre is chosen to sinter at t_n, it has its axis parallel to the z-direction, has regained the initial length l_0, and is neither loaded or strained. At the next time step $t_{n+1} = t_n + \Delta t$, the fibre is considered intact again and will then experience deformation and therefore also stress. Its final strength will only be reached after s time steps, i.e. at $t_n + t_s$. The time evolution of fibre strength during sintering is given by

$$\sigma_{c,j}(t) = (1 - e^{-\frac{t}{t_s - t}})\sigma'_{c,j,\text{final}} \text{ for } t \le t_s. \tag{3.5}$$

The new final fibre strength after sintering ($t > t_s$), $\sigma'_{\mathrm{c},j,\mathrm{final}}$, is again taken from the same probability distribution as the initial $\sigma'_{\mathrm{c},j}$. So after sintering the fibre strength can be smaller or larger than initially while the Young's modulus stays the same.
The global force $\vec{F}(t)$ needed to perform the change of position of the upper plate (dynamics in the sense of accelerations is not considered) is calculated via

$$\vec{F}(t) = \sum_{j=1}^{N_{\mathrm{intact}}} \vec{f}_j(t). \tag{3.6}$$

and the global stress $\sigma_{\mathrm{global}}(t)$ is then obtained via

$$\sigma_{\mathrm{global}}(t) = \frac{\vec{F}(t)}{A}, \tag{3.7}$$

where A is the area of the upper/lower plate. Actually the $f_j(t)$ and $F(t)$ do not have the same direction, but since only a qualitative model is thought, we use equation 3.6 for simplicity.

Table 3.1: Overview of the model input parameters with typical values used.

Symbol	Description	Typical value
N	number of fibres	1000
t_{s}	time it takes for a fibre to sinter	1.09 s
Δt	time it takes for a fibre to break	0.01 s
p_{max}	max. sintering probability	0.015
$\dot{\epsilon}_{\mathrm{global}}$	global strain rate	$2.7 \times 10^{-4}\mathrm{s}^{-1}$
E	Young's modulus of a single fibre	12 GPa
a	fibre cross section	1 mm^2
A	area of the bundle	$3 \times 10^4\mathrm{mm}^2$
l_0	height of the bundle	20 mm
β	shape factor of the Weibull distribution	0.7
$\bar{\sigma}_{\mathrm{c},i}$	mean fibre strength	4.2 MPa
ρ	density of the bundle	300 kg m^{-3}

The focus is put on the model behavior without assuming too many parameters which we cannot access within an experiment. The idea is to keep the model as simple as possible, to have as little parameters as possible and to study the effect of breaking vs. sintering. In order to compare our model with experimental data, we have to assign physical units to the time of a fibre breaking (time step) and the geometric dimensions of the model (Table 3.1). Where possible we use parameters based on experimental data, the parameters which are not directly accessible in an experiment have to be estimated. For the Young's modulus and the tensile strength we have taken typical values for ice (Petrenko and Whitworth, 1999). Density, height, and area of the bundle are as in the experiment. We assume that 10% of the ice matrix contribute to the mechanical resistance of snow, in accordance with findings by Bartelt and von Moos (2000). The sintering time we use agrees with the range of values found by Szabo and Schneebeli (2007) in their study on sintering of ice.

To summerize, the FBM is governed by only three model parameters: the shape of the Weibull distribution β, the maximum sintering probability $p_{\max}$, and the time it takes for a fibre to regain its full strength t_s.

Chapter 4

Results of the fibre bundle model

4.1 The fibre bundle model without sintering

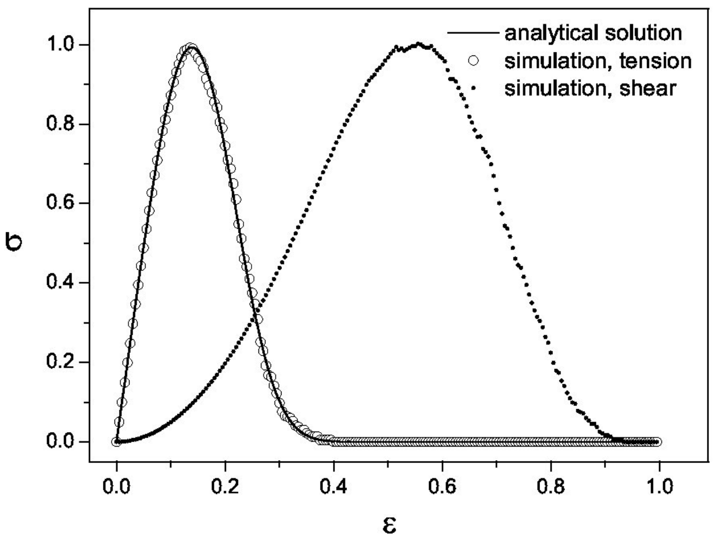

Figure 4.1: Comparison of the analytical solution (tension) with FBM simulation results without sintering (tension: open dots, shear: small solid dots) ($N = 1000$, $\beta = 3$, $\alpha = 2$).

We first compare our model to the analytical solution which exists in the case of absence of sintering. The constitutive relation for a displacement-controlled FBM under tension is given by

$$\sigma = E\epsilon[1 - P(E\epsilon)], \tag{4.1}$$

Table 4.1: Parameters of the probability density distributions shown in Figure 4.2.

no.	distri-bution	scale factor	shape factor	arith. mean	standard deviation	coeff. of variation
1	Weibull	10	0.7	12.4	18.0	1.45
2	Weibull	10	1.2	9.3	7.8	0.84
3	Weibull	10	2.0	8.8	4.8	0.52
4	uniform	-	-	10.0	5.8	0.58

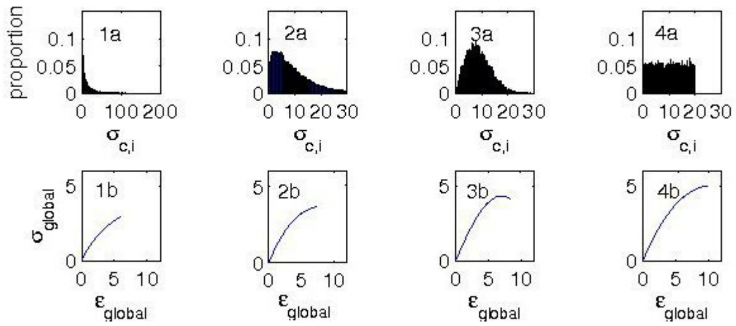

Figure 4.2: Global stress-strain curves of a bundle consisting of $N = 10^4$ fibres for different strength distributions of single fibres, sintering not considered. The upper plots (a) show histograms of fibre strength distributed according to the probability density distributions given in Table 4.1. The lower plots (b) show the global stress-strain diagram (arbitrary units).

where $\sigma = E\epsilon[1 - P(E\epsilon)]$ is the cumulative probability distribution of fibre strength (Kun et al., 2006). Fig. 4.1 shows that the analytical solution agrees with our solution if we simulate a bundle in tension without sintering, while the simulation of shear without sintering moves the stress-strain curve in the direction of larger strains.

Second, we show the dependence of the bulk properties on the microscopic strength distributions. The results shown here are valid with or without sintering. Whereas the mean value of fibre strength only has a quantitative influence on the global stress-strain behaviour, the distribution of the $\sigma_{c,i}$, i.e. the amount of variability in fibre strength, changes the bulk behaviour also qualitatively. Examples of global stress-strain curves for different probability distributions are shown in Figure 4.2. The parameters of the probability distributions used are listed in Table 4.1. The coefficient of variation is defined as $\frac{s}{\bar{x}}$, where s is the standard deviation and $\bar{x}$ the arithmetic mean.

A bundle of linear elastic fibres with varying strength displays a non-linear stress-strain relation. After an initial linear region the bundle shows non-linear behaviour before failure, i.e. $\frac{d^2\sigma}{d\epsilon^2} \leq 0 \quad \forall\epsilon$ (stress-strain curve is concave). This non-linear behaviour follows from the successive rupture of the single fibres which results in irreversible (plastic) deformation at the global level. The global peak strength depends on the type of distribution of single fibre strength, on the mean fibre strength (the larger the mean strength, the larger the bulk strength), on the standard deviation of the distribution (the larger the standard deviation, the smaller the bulk strength), and on the amount of sintering as we will discuss later. The simulations are performed with bundles consisting of a varying number of fibres N. For $N \gtrapprox 30$ the global stress-strain curves become smoother with increasing N without changing their form or position. Fibre bundle models without sintering have been studied in more detail by Kun et al. (2006) and Alava et al. (2006).

4.2 The fibre bundle model including sintering of broken fibres

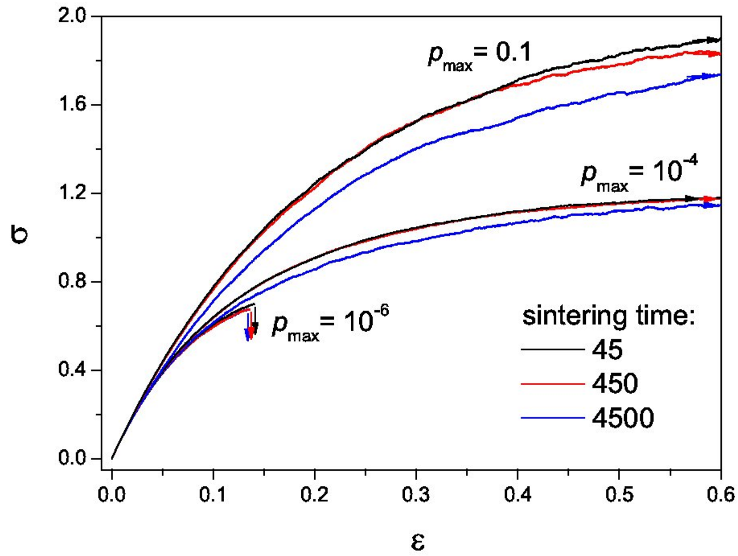

Figure 4.3: FBM simulation results with different sintering times t_s and maximum sintering probability $p_{\max}$ ($N = 10{,}000$, $\dot{\epsilon} = 5 \times 10^{-6}$, $\beta = 1$, $\alpha = 2$). The vertical arrows mark the point where the bundle fractures, while the horizontal arrows indicate that the bundle is still intact, but the simulation was stopped (stress-strain curve would continue in an almost horizontal manner).

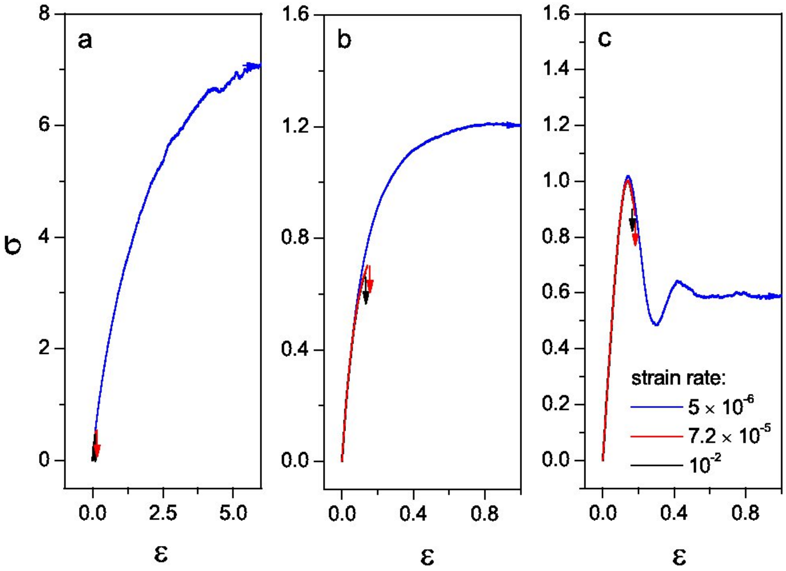

Figure 4.4: FBM simulation results with varying shape factor for the Weibull distributions of single fiber strength: (a) $\beta = 0.5$, (b) $\beta = 1$ (b), and (c) $\beta = 3$. For each shape factor stress-strain curves for three different strain rates (10^{-2}, 7.2×10^{-5}, and 5×10^{-6}) are given (N = 100 000, $\alpha = 2$, $p_{\max} = 0.0001$, $t_s = 450$). The vertical arrows mark the point where the bundle fractures, while the horizontal arrows indicate that the bundle is still intact, but the simulation was stopped (stress-strain curve would continue in an almost horizontal manner).

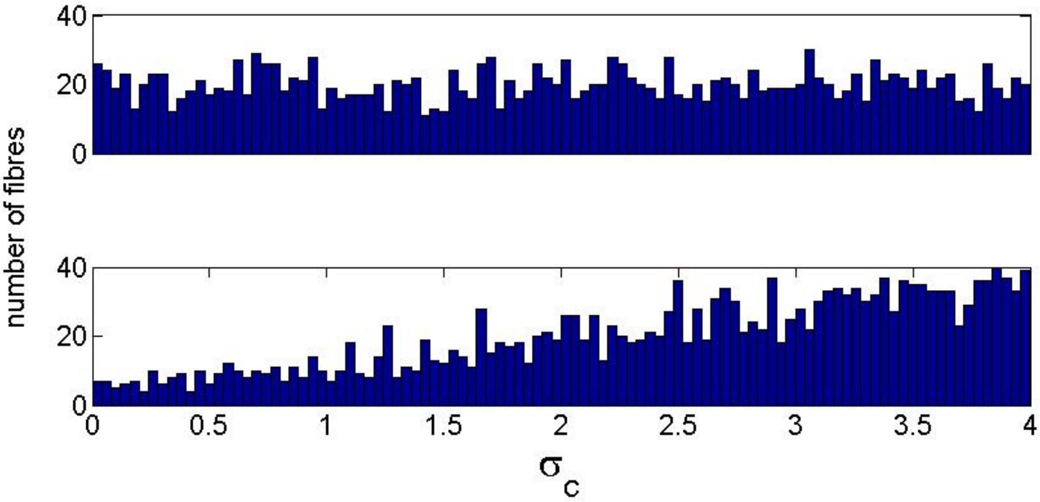

Figure 4.5: Histogram of fibre strengths before and after the simulation. A uniform probability distribution was used. The parameters were $N = 80000$, $p_{\max} = 0.2$, $t_{\mathrm{s}} = 160$, and $\dot{\epsilon} = 10^{-4}$.

Figure 4.3 shows the effect of different maximum sintering probabilities $p_{\max}$ and sintering times t_s on the mechanical behaviour for constant shape factor $\beta = 1$ and strain rate $\dot{\epsilon} = 5 \times 10^{-6}$. Note that the model results are given in arbitrary units. At this strain rate, only for low $p_{\max}$ the bundle fractures. The slope of the stress-strain curve increases with increasing sintering probability, since sintering increases the bundle's stiffness, while broken fibres make it softer.

Brittle behaviour is favoured by either decreasing $p_{\max}$ or increasing t_s. This can be understood if one imagines that if every broken fibre always sintered ($p_{\max} = 1$) and sintering was immediate $t_s = 0$, the bundle would behave perfectly ductile and would never break. Any deviation from the ideal parameters for perfectly ductile behaviour must therefore make the bundle behave more brittle.

Altering the strain rate or the shape factor of the strength distribution also has a great effect on the behaviour of the bundle (Fig. 4.4). Note that the blue curve in Figure 4.4b is equivalent to the red curve in the middle ($p_{\max} = 10^{-4}$) of Figure 4.3. Increasing the strain rate favours brittle behaviour since more fibres break at each time step if the deformation within this time step is large. The scale factor α of the distribution has no qualitative effect on the behaviour of the bundle, it effects only the quantitative value of its strength. The kink in the stress-strain curve with the slowest strain rate in Figure 4.4 was reproduced with the semi-analytical solution of Kovacs et al. (2010). The kink is a relict from the stress-strain curve without sintering.

Sintering makes the bundle stronger with time, since weak fibres break again and strong fibres survive longer. This is best illustrated using a uniform probability distribution and comparing the histogram of fibre strengths at the beginning and at the end of the simulation. Such a comparison of fibre strengths of a bundle of $N = 80000$ fibres is shown in Figure 4.5. The other parameters were $p_{\max} = 0.2$, $t_{\mathrm{s}} = 160$, and $\dot{\epsilon} = 10^{-4}$.

In Figure 4.6 we see the experimental data from Schweizer (1998) plotted together with our model results. Between the three modelled curves only the strain-rate is altered, all other parameters remain unchanged (in accordance with the experiment). Since we had to adapt our model to the experimental reality, we took a smaller number of fibres ($N = 1000$) than in the simulations shown in Figure 4.3 and 4.4. This is the reason that the stress-strain curves shown together with the experimental results are not as smooth as the stress-strain curves produced in the parameter studies.

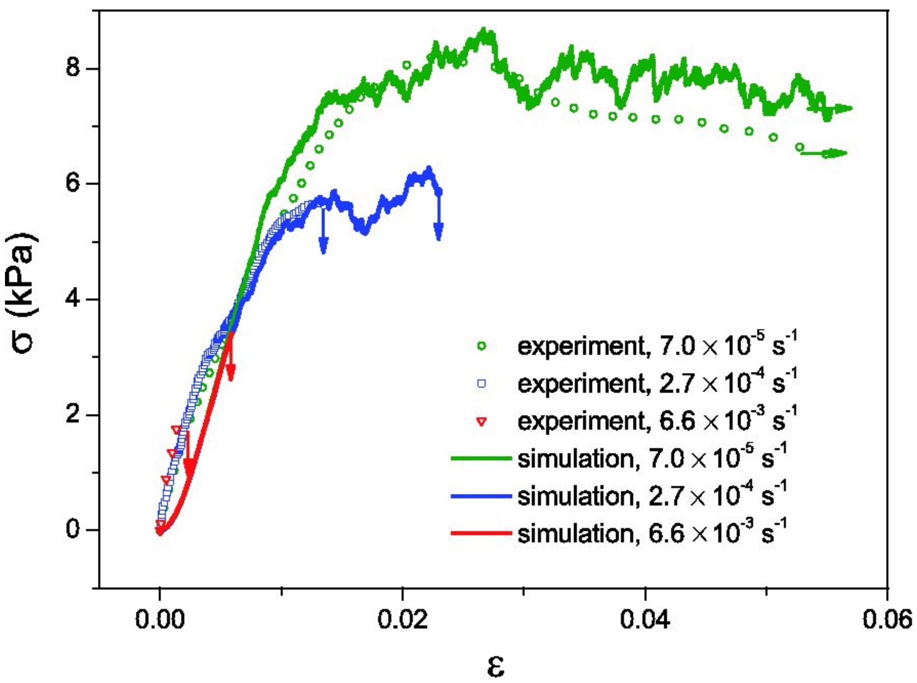

Figure 4.6: Comparison of the FBM simulation with the experimental results from Schweizer (1998).

Chapter 5

Discussion of simulations with the fibre bundle model

We tested the implementation by comparing our results with the analytical solution which exists in the case of no sintering and tensile deformation (Eq. 4.1). If the sintering probability is set to zero and we simulate tensile deformation, i.e. $\Delta l_{\text{fibre}} = \Delta x_{\text{bundle}}$, our simulations agree with the analytical solution. The fact that we have shear deformation shifts the global stress-strain curve towards higher deformations (Fig. 4.1), because $\Delta l < \Delta x$ (Eq. 3.3). Without sintering, the strain rate has no effect on the global stress-strain relation. As we assume stiff plates and impose external deformation there is no load sharing. This is because the displacement of the upper plate is imposed, and the force needed to perform this deformation is calculated. If e.g. one fiber breaks the neighboring fibers do not feel this, but the force needed to achieve a displacement of the upper plate becomes smaller. The layers above and below the weak layer are an order of magnitude stiffer than the weak layer. So although snow hardly seems to be a stiff material, compared to the weak layer, the slab and the substratum can indeed be considered rigid as a first approximation. A more detailed description of deformation versus force controlled fibre bundles is given in Kun et al. (2006).

Compared to a FBM without sintering our model produces stress-strain curves with a larger initial slope and a higher peak stress. This is due to a shift in fibre strengths to higher values. Although the newly assigned fibre strengths after sintering are taken from the same probability distribution as the strengths assigned initially, stronger fibres survive longer. In the natural snow cover, strengthening also occurs with time due to compaction and densification under its own weight which also leads to rearrangement (i.e. breaking of bonds and sintering) of grains.

The snow microstructure (crystal types and sizes) is included into the model by the shape of the strength distribution. Making more assumptions to better describe the microstructure increases the complexity, but does not necessarily improve the model. Since no experimental data yet exist, we have to assume the parameters of the strength distribution. As Figure 4.4 suggests they have a great influence on the type of the stress-strain curve. While the brittle fracture behaviour is not altered with increasing β, the ductile failure behaviour changes from creep (no failure) to strain-softening. For ductile behaviour, the strength increases with the spread of the initial distribution. For $\beta > 1$ we find strain softening in the ductile case because the (always present) strengthening effect cannot compensate for the broken fibres which do not contribute to the global stress.

Even in the case of no sintering, the amount of plastic deformation before fracture depends on the form of the distribution. If we did a load-controlled simulation the strain would become zero again in the case of unloading, but the bundle's elastic modulus would be different for the next loading cycle due to irreversibly broken fibers.

Applying our results to snow would mean that for strength characterisation of snow layers not only the strongest bonds or the mean bond strength between crystals should be considered, but also the variation, i.e. the disorder of the layer.

By incorporating sintering in the model, we show that the two different time scales for sintering and for breaking of fibres explain the rate dependence of snow strength and the ductile to brittle transition. In case the gain of strength due to sintering is faster than the increasing internal stress which results from the external deformation, a sintering fibre survives, i.e. it sinters until it reaches its final strength. Since the breaking of a fibre occurs instantaneously (within one time step) while the sintering takes s time steps, slow deformation rates favour the sintering while the breaking dominates at fast deformation rates. This leads to a transition from ductile failure behaviour to brittle fracture with increasing strain rate. At high strain rates the bundle breaks after little deformation. At slow strain rates the bundle does not break at all, as we use periodic boundary conditions. If open boundary conditions were imposed the bundle would break eventually when the deformation exceeds half the length – such as a natural finite snow sample will break at some point.

For snow this means that brittle breaking, rearranging, and sintering of bonds between snow grains might be sufficient to explain the strain rate dependent bulk behaviour of snow. We can simulate macroscopic plastic behaviour (of the whole bundle) although the microscopic behaviour (of a single fibre) is purely elastic. The plastic deformation within the ice matrix, i.e. more realistic ice properties of grains or bonds between them, seems to be of secondary importance. The breaking and sintering lead to an increase of the mean value of fibre strength over time, because the weakest fibres will break and the strongest will last. In snow, we also see a strengthening of the natural snowpack with time due to vertical settling.

Also the maximum sintering probability $p_{\max}$ and the sintering time t_s affect the global mechanical behaviour of the bundle (Fig. 4.3). The actual time it takes for a bond to break is not so important, the main point is that the breaking is faster than the sintering. Although this is only a very simple model, we compare our results to the experimental results from Schweizer (1998) (Fig. 4.6). At the slowest strain rate the model results agree quite well with the experimental data. The higher residual stress reached in the simulation might be due to the periodic boundary conditions used for the model. For the intermediate strain rate a higher fracture strain than in the experiment is found, but the fracture stress is roughly the same. At the highest strain rate the model shows higher fracture strain and stress than found in the experiment. This is probably due to to fact that the model starts in an 'ideally strong' state, namely with all fibres parallel without any deformation. The convexity of the modelled curve is due to the geometric arrangement of the fibres. They are arranged vertically but the plates move horizontally. At small deformations, the exact orientation of the microstructural elements becomes increasingly important. This effect we cannot capture in our model containing vertical fibres only. However, the different failure behaviour which snow exhibits at different strain rates, that is brittle behaviour at high and ductile behaviour at low strain rates, is captured very well with our model.

Chapter 6

Experimental methods

6.1 Snow sampling

Snow samples were taken from the field or produced in the laboratory. Whereas field samples are faster to obtain during winter, grown samples are more easily controlled (greater reproducibility) and season independent.

6.1.1 Harvesting of snow samples in the field

Snow samples containing a weak layer are very relevant study objects but also very difficult to transport. Therefore, all our natural snow samples were taken from the study plot next to the SLF cold laboratory. We continuously monitored the snowpack during the winter season by making profiles and observing the snow surface for surface hoar. When we found a suitable weak layer for testing, we took samples from that layer. With suitable weak layer we mean a weak layer which is clearly defined and has sufficiently thick and cohesive layers above and below which allow cutting the samples and transporting them into the laboratory without destroying them. The transporting into the laboratory was done by taking away superfluous snow on top of the sampled area, then cutting the sides of the snow samples with a snow saw, and finally carefully extracting the samples from the snowpack and putting them on a styrofoam plate with a spatula. The samples were then carried into the cold laboratory for storage. In the laboratory the samples were stored under styrofoam hoods for maximum a week at -20 °C.

The snow samples of types A,B, and C were natural samples harvested as described above. These three different kind of samples all had a weak layer (consisting of either surface hoar or depth hoar crystals) in the middle, i.e. each sample consisted of three layers. We tested 12 to 34 samples for each layer. Typical lateral dimensions of the samples was 15 cm long and 10 cm wide. An overview of the samples' properties is given in Table 6.1.

Table 6.1: Density (measured manually for samples B and C and with μ-CT images for samples A), height and snow type of the natural snow samples tested. The burial time of the weak layer is also given. Snow type is described as grain type according to Fierz et al. (2009), average grain size, and hand hardness index (1: Fist, 2: Four fingers).

Name	Type	Density (kg m^{-3})	Thickness (mm)	Snow type	Burial time (days)
A	layered,	170	30	RG, 0.5, 1	
	natural	60	5	SH, 5,1	3
		170	30	RG, 0.5,1-2	
B	layered,	200	40	RG(FC), 0.25-1.5, 2-3	
	natural	200	50	DH(FC), 1.25-3, 1	30
		200	20	CR, 1-2, 4	
C	layered,	230	28	RG, 0.5, 2-3	
	natural	70	10	SH, 15, 1-2	14
		190	46	FC, 1-1.5, 1-2	

6.1.2 Production of snow samples in the cold laboratory

Homogeneous snow samples are samples which consist of only one type of snow (one layer). For the production of homogeneous snow samples, we took new snow produced by a snow machine (Meier, 2006), sieved it into a box (2 mm grid sieve), compressed it by a defined short distance (usually from initial height 3.5 cm to compressed height 3 cm), and let it sinter one to two days at $-6\,°C$. The resulting snow consisted of small rounded particles (RG, 0.5 mm, 2). The larger the compressed distance and the longer the sintering time, the denser, harder, and stiffer the resulting snow samples became. The densities which could be achieved this way ranged from 100 - 500 kgm^{-3}. We usually tested samples with densities of 250 - 400 kgm^{-3}, see Table 6.2. Preparing lower density samples was possible, but the handling of extremely low density samples is not feasible for our experiments.

Considering avalanche release, snow samples containing a weak layer (e.g. faceted crystals or buried surface hoar) are more relevant than homogeneous snow samples. In the cold laboratory, weak layers of faceted crystals and depth hoar were grown by applying a strong vertical temperature gradient to a snow sample as described by Fukuzawa and Narita (1993). Our snow samples for growing faceted crystals consisted of a layer of low density snow (fresh new snow crystals produced by the snow machine) sandwiched between two dense homogeneous snow layers ($\rho \approx 300$ kg m^{-3}); produced similarly as the homogeneous samples described above. A heat foil placed at the bottom of such a sample was used to create a temperature gradient of about 200 K m^{-1}. The heat foil kept the bottom of the sample at e.g. -5 °C while the laboratory temperature was set to -20 °C. Within one to two days the low-density layer transformed into faceted crystals and some small depth hoar (Fig. 6.2).

Surface hoar layers grow through deposition of water vapour onto the snow surface. The crystals formed due to this deposition process are primarily plate or needle like (Lang et al., 1984). If they are covered by a subsequent snowfall, a layer with low shear strength is formed. Surface hoar layers were produced by forcing water vapour to flow over a cold snow surface. The surface hoar crystals were then covered with a layer of sieved new snow, which was again left to sinter for at least one day. Figure 6.1 schematically shows the experimental setups for producing the weak layers while Figures 6.2 shows the resulting snow crystals.

Samples of type H1 (homogeneous), L1 (layered, depth hoar), and TRA (layered, depth hoar)[1] where produced as described above. An overview of these samples' properties is given in Table 6.2. The surface hoar samples we produced in the laboratory did not have consistent mechanical properties, since the production parameters (mainly vapour flow) could not be kept constant enough. We therefore do not show any results with artificial surface hoar samples.

[1] L1 and TRA were both artificial depth hoar samples, but they differed in weak layer thickness and properties of the layers above and below, see Table 6.2.

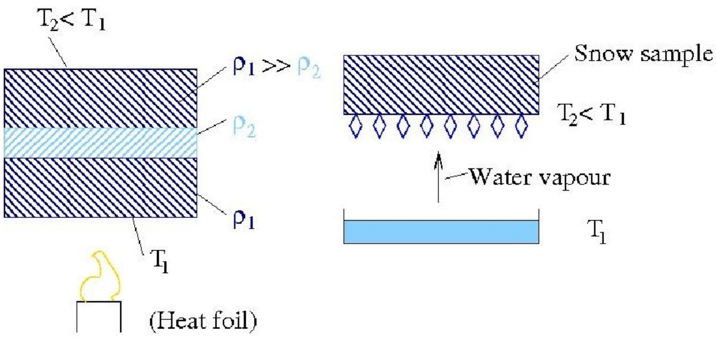

Figure 6.1: Experimental setup for producing a layer of faceted crystals (left) and surface hoar (right). T denotes temperature and ρ denotes density.

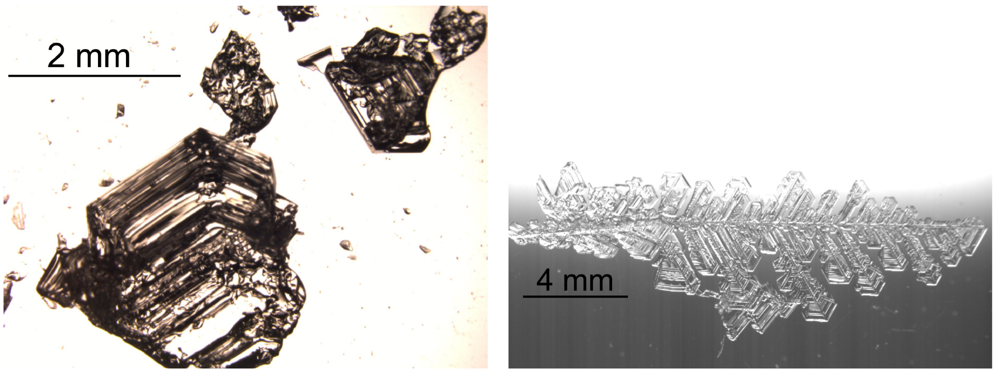

Figure 6.2: Artificially produced depth hoar crystal (left) and artificially produced surface hoar crystal (right, photo: C. Mitterer).

Table 6.2: Density, height and snow type of the artificial snow samples tested. The weak layer within samples of type L1 was too thin for the density to be measured. Snow type is again described as grain type according to Fierz et al. (2009), average grain size (mm), and hand hardness index (1: Fist, 2: Four fingers, 3: One finger, 4: Pencil).

Name	Type	Density ($kg\ m^{-3}$)	Thickness (mm)	Snow type
H1	homogeneous, artificial	270	48	RG, 0.5, 2
L1	layered, artificial	280	28	RG, 0.5, 2
		–	1	FC(DH), 1, 1
		280	46	RG, 0.5, 2
TRA	layered artificial	300	32	RG, 0.75, 4
		240	5	DH, 2, 3
		300	30	RG, 0.75, 4

6.2 Deformation-controlled shear apparatus

The displacement-controlled direct shear experiments were performed in an apparatus described by Theile et al. (2009), a so-called linear friction tester (LFT) (Fig. 6.3). The LFT consisted of two high power and high precision computer controlled linear drives that could be programmed to realize any 2-dimensional movements. In the experiments we performed the vertical drive was turned off, so the upper sample holder rested freely on the snow sample under its own weight (which was partly compensated with a counterweight, since the upper sample holder was quite heavy and would have crushed too many snow samples). The snow sample was frozen to the bottom plate and the upper plate under the weight of the upper sample holder (Figs. 6.3 and 6.4). The plates were warmed with a blow-dryer, and then the upper plate was left to rest on the snow sample for several minutes. After the freezing the horizontal drive (step motor) moved the upper plate in horizontal direction (see Fig. 6.4) by a constant velocity. During the experiments the force and displacement were recorded with a sampling rate from 1 to 10 Hz. The force was measured with 0.1 N resolution by a Kistler Model 9254 piezoelectric force plate (Kistler, Switzerland) placed under the lower sample holder. It measured all three force components simultaneously. The displacement was measured with 1 μm resolution by a linear encoder (Renishaw, UK).

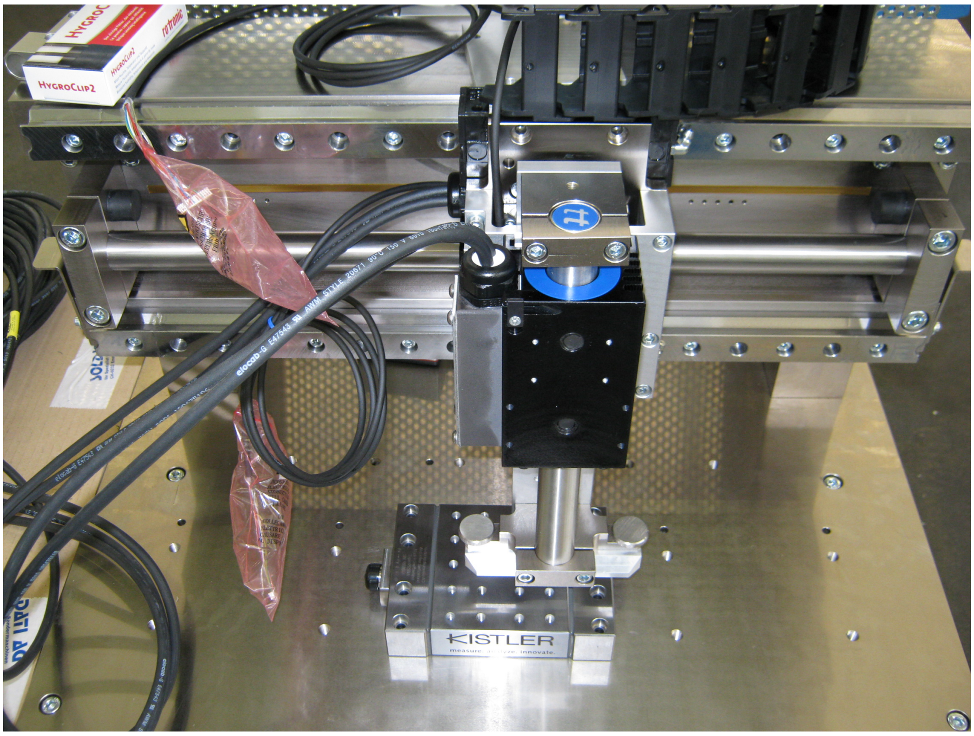

Figure 6.3: Photo (from above) of the displacement-controlled shear apparatus we used. One can see the force plate and the upper arm of the apparatus. The sample holders, which can be seen in Figure 6.4 are screwed onto the force plate and the upper arm, respectively. Photo by M. Jaggi.

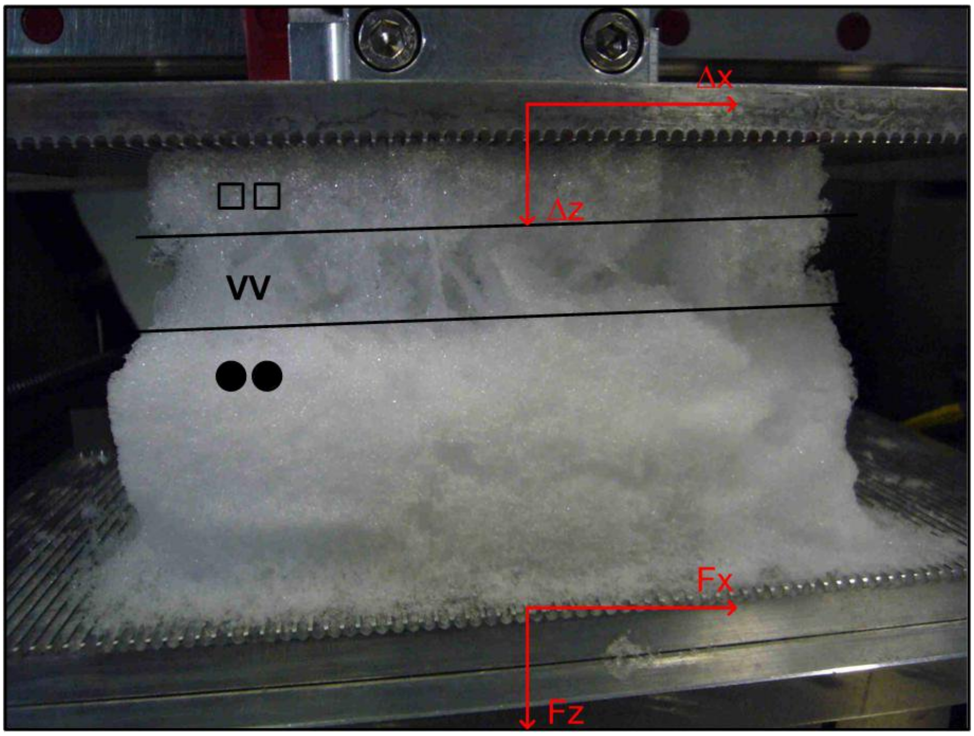

Figure 6.4: Layered snow sample in the displacement-controlled shear apparatus. The quantities measured are the shear displacement Δx, the normal displacement Δz, the shear force F_x, and the normal force F_z. The layers consist of (starting at the top): faceted crystals (FC), surface hoar (SH), rounded grains (RG). The height of the weak layer was 1 cm.

6.3 Force-controlled loading apparatus

The force-controlled loading apparatus (Fig. 6.5) was desigend together with Robert Ernst (Ernst, 2009). The idea was to mimic loading conditions found in a natural snowpack. The relation between shear and normal force was determined by the 'slope angle', which had a range of 0 - 60°. The maximum size of the snow samples that could be tested with the apparatus was 0.2 m × 0.1 m × 0.15 m (length × width × height). Prior to loading, the snow sample was frozen onto the lower sample holder which was tilted by an angle α and had been heated with a heating fan. Then the upper sample holder was heated and placed on top of the snow sample. The loading of the upper sample holder was achieved by draining fluid (i.e. alcohol) from a container placed on top of the shear apparatus into a container placed below the snow sample and attached to the upper sample holder. In order to avoid a torque on the weak layer, the upper sample holder was constructed T-shaped, and the weight was attached at its center of mass, so that the point of application of the load was at the weak layer (see Fig. 6.5). In Figure 6.5b the weak layer is faintly visible on the right side of the sample at the height of the red cross which marks the center of gravity of the upper sample holder. The weight of the upper sample holder was compensated with a balanced weight, which was also attached to the center of mass. The loading rate could be varied from 0.01 N s^{-1} (representing snowfall) to 5 N s^{-1} (representing rapid loading), and the maximum possible load was 180 N. Parts of the methods presented here have already been published in Reiweger et al. (2010) and Reiweger et al. (2009a).

The force acting on the sample, i.e. the weight of the drained liquid, was measured with a force sensor (BGI sensor) positioned below the snow sample, with a maximum range of 250 N and an accuracy of ± 0.1 N. The signal from the force sensor was recorded with a sampling rate of 65 Hz.

The displacements of the upper sample holder, in parallel and normal direction to the slope, were measured with displacement sensors. The sensors were conductive-plastic resistance sensors (T 25 from Novotechnik) with a range of 30 mm and an accuracy of ± 0.01 mm. The signals from the displacement sensors were recorded with a data

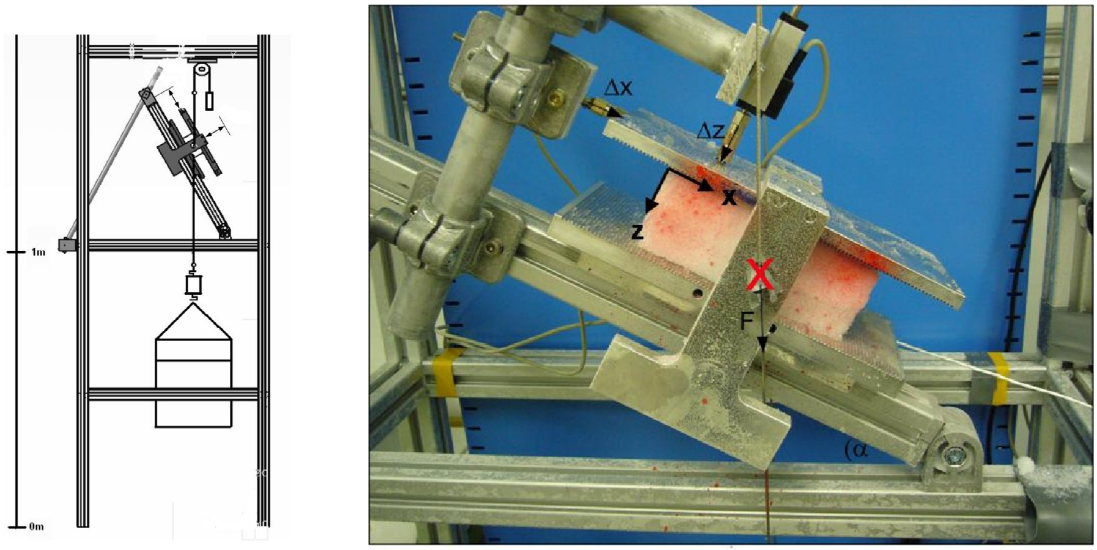

Figure 6.5: Schematic representation of the new loading apparatus and photograph of a snow sample in the apparatus. α denotes the slope angle, F is the force acting on the snow sample, and Δz and Δx denote the compressive and shear displacement of the upper plate.

acquisition card (DAQCard-1200) from National Instruments with a sampling rate of 25 kHz.

6.4 Tomography measurements of the snow samples

High resolution 3-dimensional images of the snow microstructure can be obtained with X-ray tomography (Schneebeli and Sokratov, 2004). A μ-CT 80 X-ray micro computer tomograph (μ-CT) from Sanco Medical (Bassersdorf, Switzerland) in the SLF cold laboratory was used to characterize the microstructure of the snow samples. Images with 18 μm nominal resolution were taken of cutouts (approximately 1.5 cm in length and width and 5 cm in height) of our samples. The duration of one scan was rougly 3 h. For image processing and stereological characterization the raw sinograms of the μ-CT were transformed into 16-bit images. To reduce the noise the stacked images were median filtered using a $3 \times 3 \times 3$ kernel and Gaussian filtered using a $5 \times 5 \times 5$ kernel with $\sigma = 1.2$. Finally these images were segmented by thresholding, resulting in a binary image of the snow microstructure. This work was mainly done by Margreth Matzl. With an IDL-program developed by Theile and Schneebeli (2010) we extracted parameters like the density of the thin weak layers, the specific surface area, and the coordination number of the single snow grains. The specific surface area measures the total surface area per ice volume, it is a commonly used material property of cellular solids.

6.5 Particle velocimetry method

During both the displacement-controlled shear and the force-controlled loading experiments the displacement field on the side of the snow samples was visualized with a particle image velocimetry algorithm (PIV). Assuming plane strain conditions, the displacement field on the side of the sample is representative for the displacement field also within the sample. The PIV algorithm recognizes patterns on a photograph (or an image from a movie sequence) taken from the snow sample and tracks them over various subsequent photographs. The snow sample was sprayed with paint to achieve sufficient contrast for the PIV algorithm to find a pattern. With a resolution of 1936 $\times$ 1288 pixels the maximum image rate was one image every two seconds. By comparing a sequence of images taken at different times during the experiment, the displacement, strain, and path lines were calculated (Roesgen and Totaro, 1995). The algorithm was adapted and tested for studying the deformation of snow by Huber (2008). Before applying the algorithm, we performed a parameter study to find the optimal parameter setting for our measurements. The parameters which can be varied within the PIV algorithm are:

```
wxy  size of interrogation window
sxy  max. shift in x & y-directions to be tested
oxy  offset to be included between search windows
dxy  shift between adjacent evaluations
```

While the optimal values `sxy = [5,5]`, `oxy = [0,0]`, and `dxy = [16,8]` were estimated by Thomas Huber in comparison with our experimental setup (speed of the upper sample holder, global deformation of the sample), the input variable `wxy` was optimized by trial and error. If the interrogation window was chosen too small, e.g. `wxy = [15,15]`, the displacement field was full of errors (Fig. 6.6), if the interrogation window was chosen too big, e.g. `wxy = [250,250]`, there was too much smoothing and no information obtained about the change of displacement within the snow sample (Fig. 6.7). The optimal size of the interrogation window was somewhere in between, at around `wxy = [100,100]` (Fig. 6.8). Note that the algorithm gives a constant displacement within an interrogation window. The units in the Figures are pixels, and the upper left arrow in all three Figures is only for reference, its coordinates are [0.5,0.5].

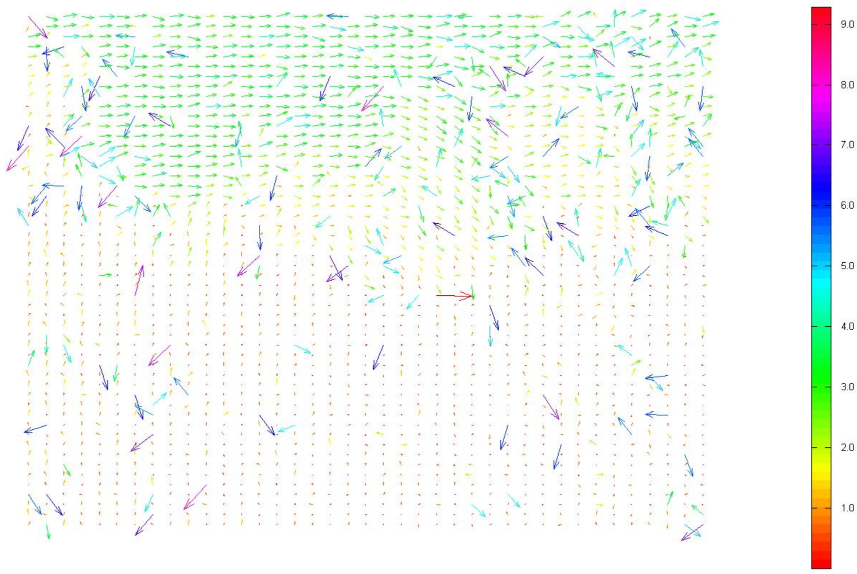

Figure 6.6: PIV test, interrogation window too small. Units are pixels.

For the optimal parameter and our camera setup, the accuracy of the displacement calculated by the algorithm was about $\pm$ 0.01 mm. This was checked by calculating the displacement of one image (which should be zero), and by calculating the displacement of the snow sample right under the upper sample holder (which should equal the global displacement measured with the linear encoder of the LFT).

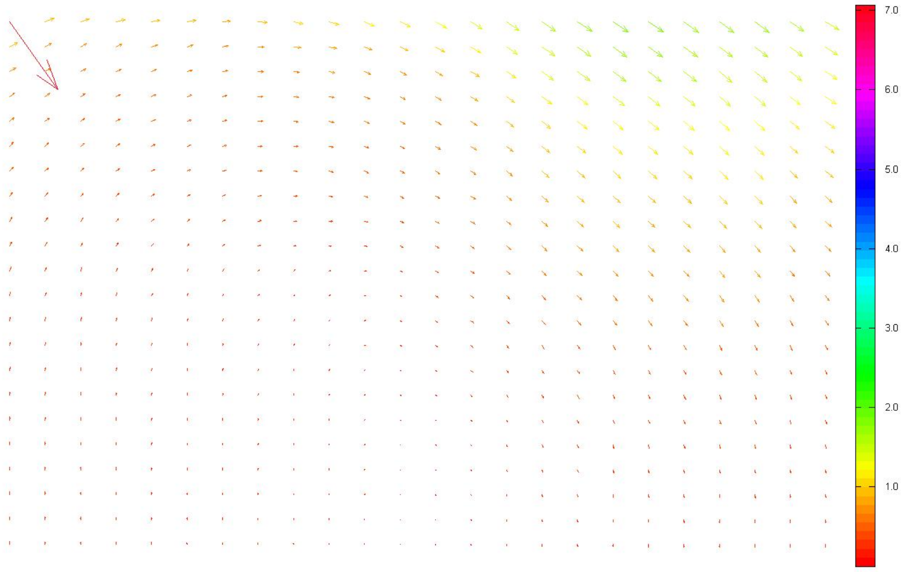

Figure 6.7: PIV test, interrogation window too big. Units are pixels.

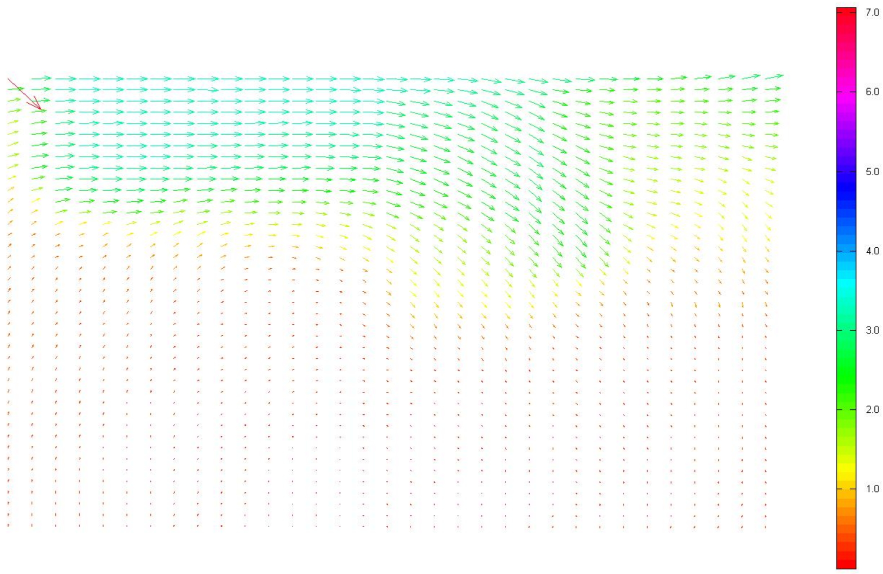

Figure 6.8: PIV test, optimal size of interrogation window. Units are pixels.

6.6 High speed camera imaging

For fast experiments we acquired images at a high rate with a high-speed camera. The camera was of type VDS Vosskühler HCC-1000. It had a resolution of 1024 by 512 effective pixels. Images were recorded at a rate of approximately 300 frames per second, depending on aperture and shutter speed. The device could store a sequence of 1024 images preceding a trigger signal, which was given manually soon after termination of the fracture process. The camera was mounted on a tripod and aimed approximately perpendicular to the exposed cross-section of the sample.

6.7 Acoustic emission measurement system

During the loading experiments acoustic emission (AE) signals were recorded. The setup was installed and tested by Robert Ernst within his Master's Thesis (Ernst, 2009). He performed standard acoustic methods like pencil lead fractures and studied the waveform of the signals he obtained with an oscilloscope. During the experiments presented within this thesis, only the count rate was measured and only one acoustic sensor was used at a time.

The acoustic measurement setup is shown in Figure 6.9. The piezoelectric transducers were mounted in the bottom plate of the sample holder, i.e. the sensor was directly frozen to the snow. The AE sensor used in most of the experiments shown below was a wide band piezoelectric transducer (range 100 kHz - 1 MHz) from Physical Acoustics (PA 1220B). If we show acoustic emission results measured with another sensor, this is mentioned explicitly. The signal was amplified (by 60 dB) with a preamplifier (also from PA) which included a filter with a frequency range from 400-600 kHz. The purpose of the filter was to eliminate background noise from the coldroom cooling machine. The outcoming signal was fed into a burst-trigger circuit with a threshold of 150 mV and a dead time of 20 μs. The threshold level setting and the dead time allowed us to avoid triggering by background noise with low intensity and short disturbance signals. The optimal threshold and dead time were selected on the basis of preliminary experiments, where we used an oscilloscope to study the acoustic waveform (Ernst, 2009). If the acoustic signal exceeded the threshold the burst-trigger circuit emitted a pulse of length of the dead time. The pulses were recorded with a maximum sampling rate of 20 kHz. The pulses per time give the acoustic count rate, which is a measure of the intensity of the acoustic activity. The setup we used was originally developed by Scapozza et al. (2004) who studied the acoustic emission response of snow under compression.

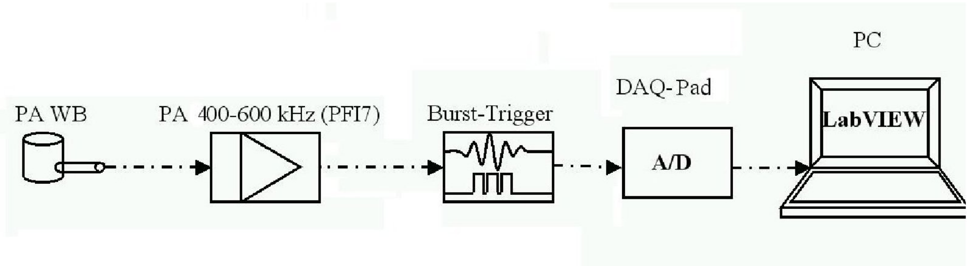

Figure 6.9: Acoustic emission setup.

6.8 Data acquisition

For the loading apparatus we programmed the data acqusition ourselves. The force sensor had a serial RS-232 output from where the signal was fed into a PC with a serial socket. The signals from the displacement and the acoustic sensors were fed into a DAQCard and a DAQPad, respectively. The data acquisition from the serial input, the DAQCard, and the DAQPad were controlled, synchronized, and recorded with a LABVIEW program. The photographs taken with the camera were directly transferred to the computer with the program DSLR Remote Pro.

Chapter 7

Experimental results

7.1 Analyzing the snow samples with tomography measurements

Additionally to manual characterization four types of samples where scanned with the μ-CT, namely samples of type A, B, C, and TRA (Tables 6.1 and 6.2).

Figure 7.1 shows a μ-CT image of a sample of type A. The surface hoar crystals and the holes between them are clearly visible in the middle of the sample. Also visible are small fragments of rounded and decomposed grains which had fallen in the gaps between the surface hoar crystals.

Figure 7.2 shows a μ-CT image of a sample of type B. The weak layer is fairly thick, only at the very top and bottom can one see the surrounding layers.

Figure 7.3 shows a μ-CT image of a sample of type C. The rounded grains in the upper layer are best visible in the upper left corner of the image. The large crystals in the middle were the surface hoar crystals which constituted the weak layer, while the crystals at the bottom of the sample were faceted crystals (slightly visible in the lower right corner of the image).

Figure 7.4 shows a μ-CT image of a sample of type TRA. One can clearly see the cup-shaped crystals typical for depth hoar in the middle of the sample and the rounded grains above and below.

With an Interactive Data Language (IDL) program developed by Theile and Schneebeli (2010) the μ-CT scans could be analyzed and several structural parameters calculated. An overview of the parameters obtained with this program by analysis of the weak layer is given in Table 7.1.

Table 7.1: Overview of the microstructural parameters derived from the μ-CT images. SSA denotes the specific surface area of the weak layer, ρ is the density of the weak layer, and CN is the coordination number of the grains within the weak layer. The samples are characterized in Tables 6.1 and 6.2.

Sample	SSA (mm^{-1})	ρ (kg m^{-3})	CN
A	25.3	60	*not possible*
B	9.6	190	*not possible*
C	13.5	71	*not possible*
TRA	12.5	240	*not possible*

The weak layers in samples B and TRA have a significantly higher density than the weak layers in samples A and C. As we will see later in Section 7.2, samples B and TRA have a higher shear strength than samples A and C (Fig. 7.15). Within our very limited number of measurements, we could not find a correlation between the specific surface area and snow strength.

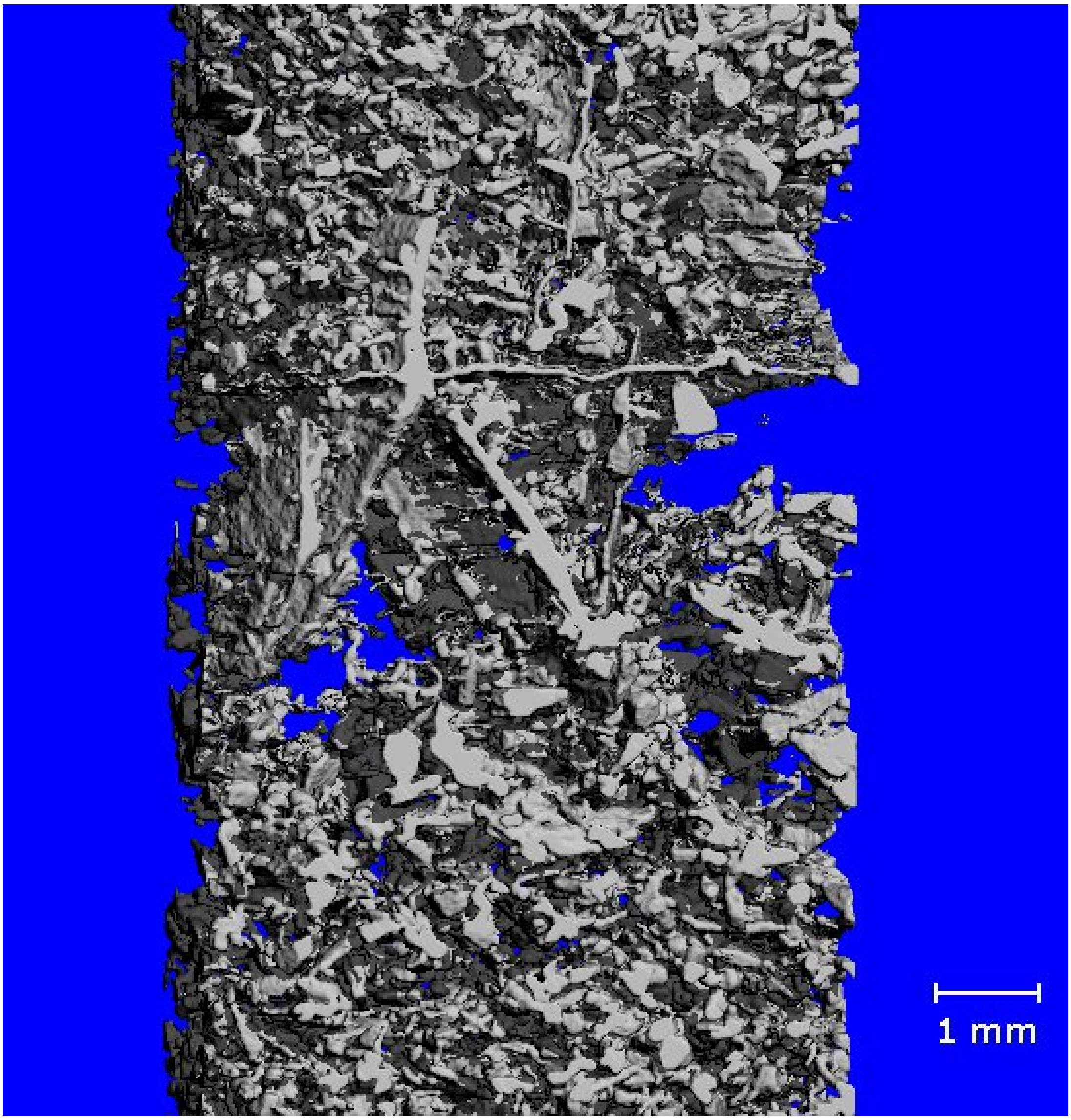

Figure 7.1: μ-CT image of a sample of type A, including a natural layer of buried surface hoar (Table 6.1).

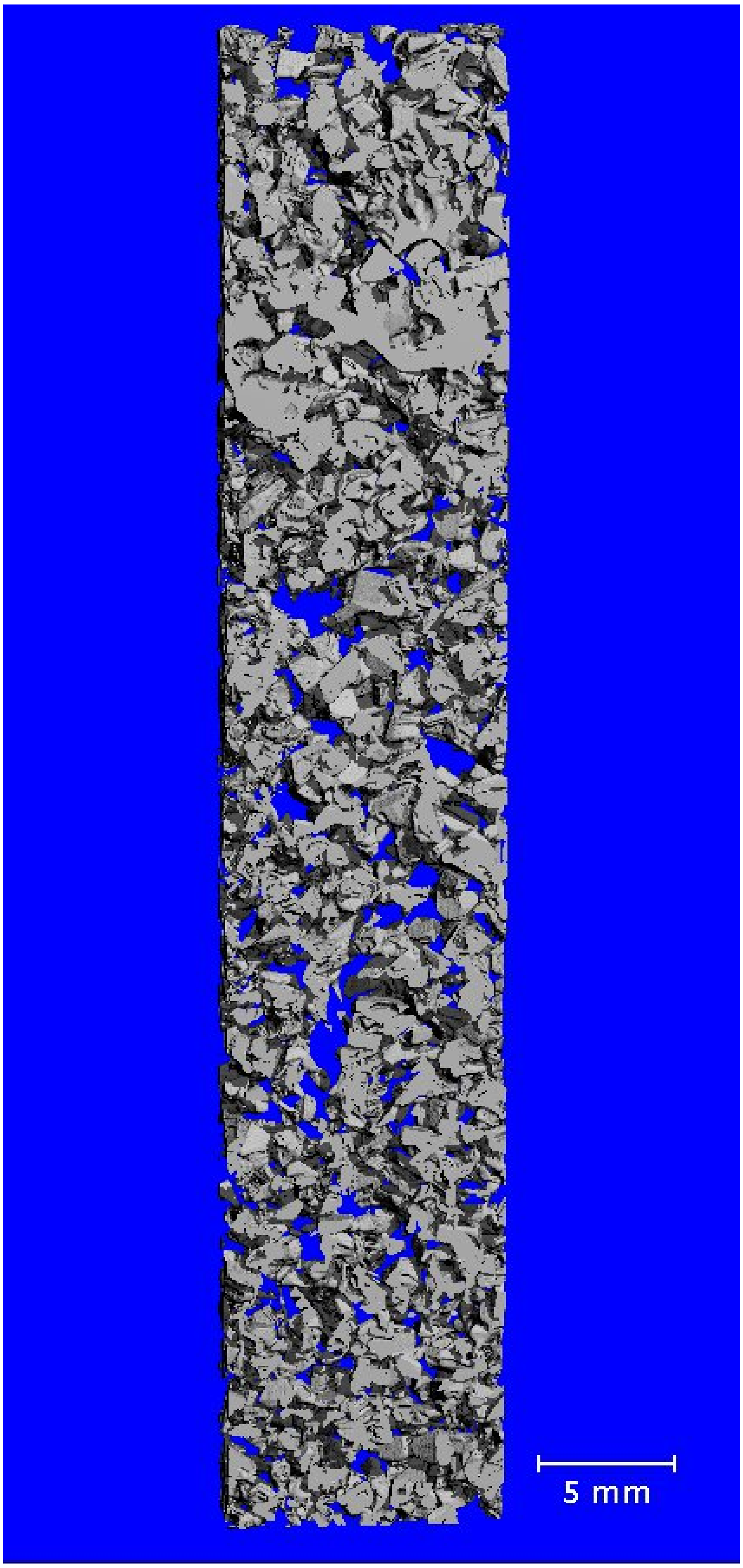

Figure 7.2: μ-CT image of a sample of type B, including a natural layer of depth hoar (Table 6.1).

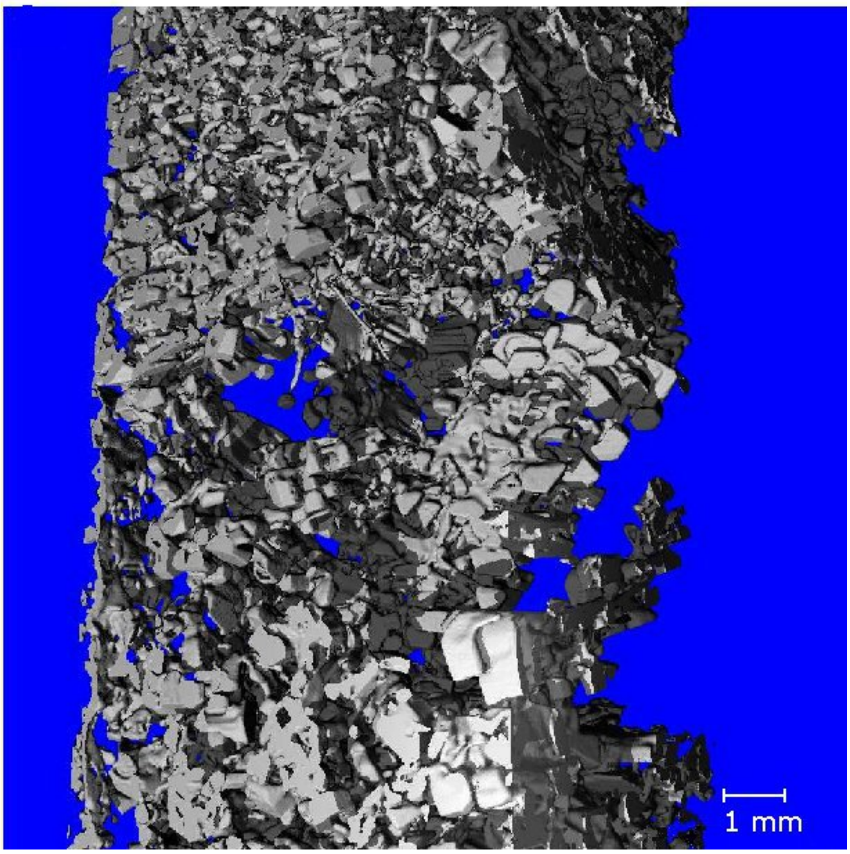

Figure 7.3: μ-CT image of a sample of type C, including a natural layer of buried surface hoar (Table 6.1).

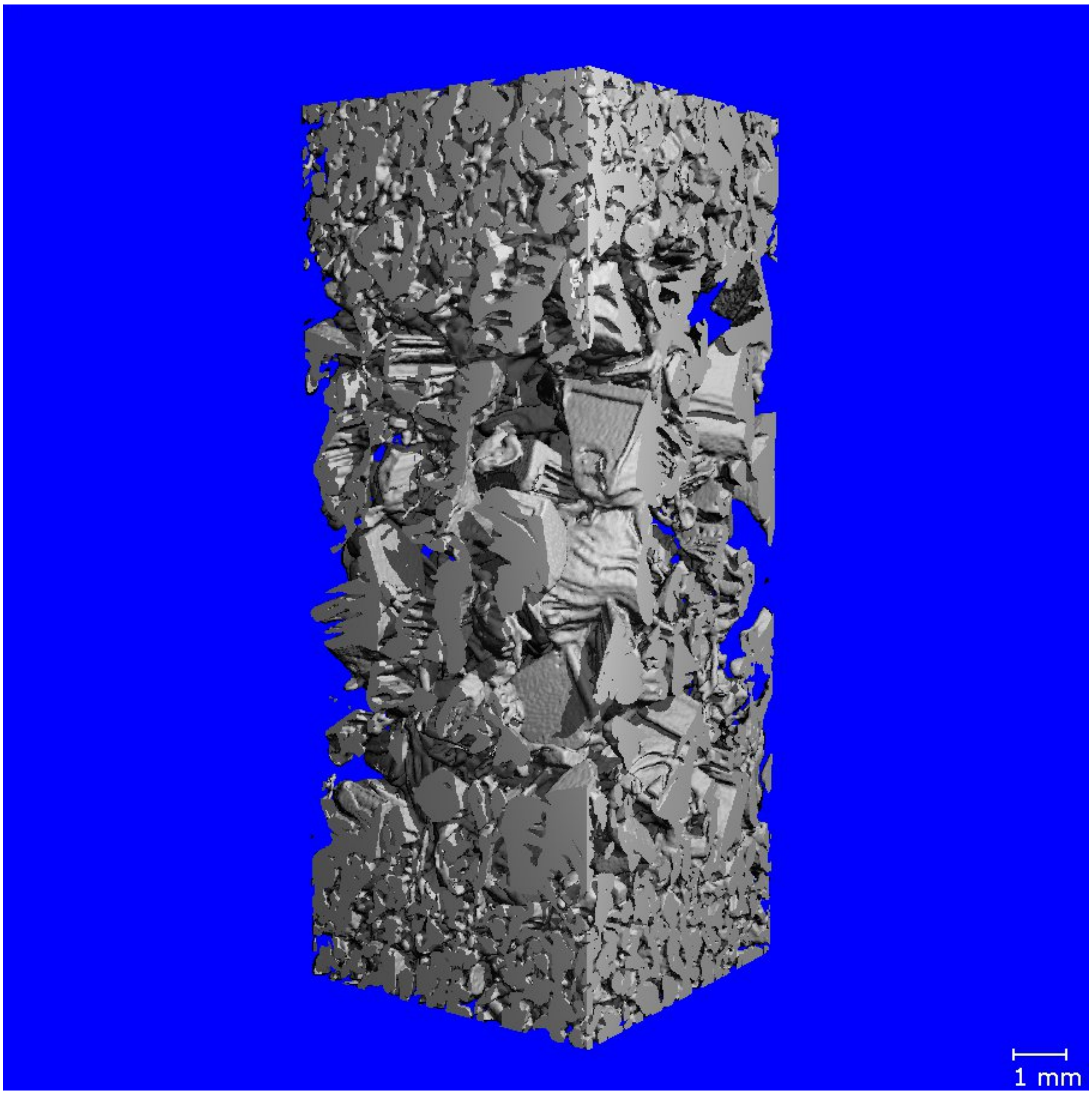

Figure 7.4: μ-CT image of a sample of type TRA, including a layer of artificial depth hoar (Table 6.2).

7.2 Displacement-controlled experiments

We performed over 70 displacement-controlled direct shear experiments with the LFT. Displacement-controlled experiments plus μ-CT measurements were performed with samples of type A, B, C, and TRA. An overview of all successful experiments with the samples where μ-CT images exist is given in Table 7.2. Samples AA3, BB4, BB5, and BB6[1] showed strain-softening; we could thus define a peak stress (σ_c), but the samples did not fail, so no strain at failure (ϵ_c) could be given. The results of the other experiments are summarized in Appendix B. The strains given are the global strains, i.e. the displacement of the upper plate divided by the initial height of the whole sample. The laboratory temperature was set to -6 °C for all experiments, and the normal stress σ_z was 0.9 ±0.3 kPa.

Table 7.2: Overview of deformation-controlled shear experiments performed with samples of types A, B[2], C, and TRA (see Tables 6.1 and 6.2). The experiments with samples of types TRA and HOM can also be found in the table in Appendix B, sorted by number. $\dot{\epsilon}$, σ_c, and ϵ_c denote the global shear strain rate, the peak shear stress, and the global shear strain at fracture, respectively.

Sample	$\dot{\epsilon}$ (s^{-1})	σ_c(kPa)	ϵ_c	Sample	$\dot{\epsilon}$ (s^{-1})	σ_c(kPa)	ϵ_c
AA2	1.6×10^{-3}	1.1	3.1×10^{-3}	TRA38	2.5×10^{-4}	7.2	0.1
AA3	1.5×10^{-4}	2.1	–	TRA43	2.0×10^{-4}	7.6	0.26
AA4	1.5×10^{-4}	3.8	0.3	TRA70	1.5×10^{-3}	2	2.8×10^{-3}
AA5	1.3×10^{-3}	1.0	4×10^{-4}	TRA71	1.4×10^{-3}	2.4	3.5×10^{-3}
BB1	1.7×10^{-3}	1.8	2×10^{-3}				
BB2	1.5×10^{-3}	1.3	4.6×10^{-3}	HOM47	3.1×10^{-4}	> 6	3×10^{-3}
BB3	1.8×10^{-3}	4.5	3.4×10^{-3}	HOM50	3.1×10^{-3}	4.2	$> 6\times10^{-2}$
BB4	1.7×10^{-4}	8	–				
BB5	1.6×10^{-4}	6.3	–				
BB6	1.9×10^{-4}	5.7	–				
C2	1.2×10^{-3}	1.2	3.6×10^{-3}				
C4	1.3×10^{-3}	0.5	2.6×10^{-3}				
C5	1.1×10^{-3}	0.6	3.2×10^{-3}				
C6	1.5×10^{-4}	2.9	0.27				
C7	1.3×10^{-4}	2.4	0.18				
C8	2.2×10^{-4}	2.5	0.46				
C9	6.1×10^{-4}	1.3	3.2×10^{-3}				
C10	7.1×10^{-4}	0.9	6.7×10^{-3}				

[1] Samples with names 'AA' and 'BB' are samples of types A and B with which displacement-controlled experiments were performed. This is to differentiate from the force-controlled experiments, which were also performed with samples of types A and B.

7.2.1 Stress-strain curves

As freezing the samples to the sample holders proved to be quite tricky, we performed several test experiments with homogeneous samples. Typical stress-strain curves for homogeneous samples consisting of rounded grains at a fast strain rate ($\dot{\epsilon} = 3.1 \times 10^{-3}\mathrm{s}^{-1}$, sample HOM 50, see Table in Appendix B) and a slow strain rate ($\dot{\epsilon} = 3.1 \times 10^{-4}\mathrm{s}^{-1}$, sample HOM 47, see Table in Appendix B) are shown in Figure 7.5. Sample HOM 47 failed in a ductile manner at a strain larger than 0.06, while sample HOM 50 failed in a brittle manner. This is in perfect agreement with Schweizer (1998) who found the ductile-to-brittle transition at a strain rate of about $1 \times 10^{-3}\mathrm{s}^{-1}$. The fracture surfaces for homogeneous samples was always rough and never a perfect smooth fracture parallel to the shear direction and sample holders.

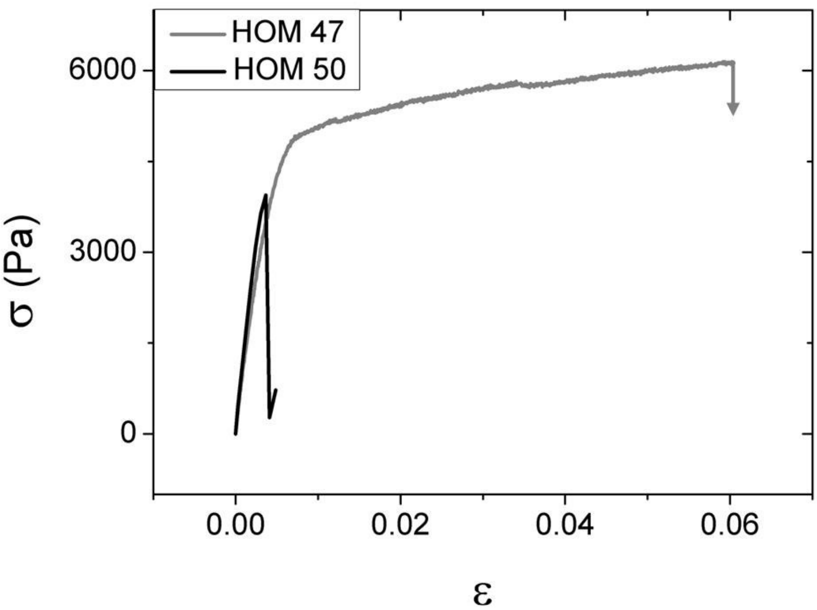

Figure 7.5: Stress-strain curves for shear experiments of homogeneous snow samples at a low ($3.1 \times 10^{-4}\mathrm{s}^{-1}$, sample HOM 47) and a high ($3.1 \times 10^{-3}\mathrm{s}^{-1}$, sample HOM 50) strain rate. The arrow marks the failure of sample HOM 47.

For layered samples, the stress-strain curves look qualitatively similar as for the homogeneous samples. Typical stress-strain curves for samples of kind A (natural surface hoar) for a slow strain rate (sample AA4, $\dot{\epsilon} = 1.5 \times 10^{-4}\mathrm{s}^{-1}$) and a fast strain rate (sample AA5,

$\dot{\epsilon} = 1.3 \times 10^{-3}\mathrm{s}^{-1}$) are shown in Fig. 7.6. Note that the strain-rates given here are the global strain rates, and as we will see later, the strain rates in the weak layer for samples of kind A were higher by about a factor of 13 ($= \frac{h_{\mathrm{tot}}}{h_{\mathrm{WL}}}$).

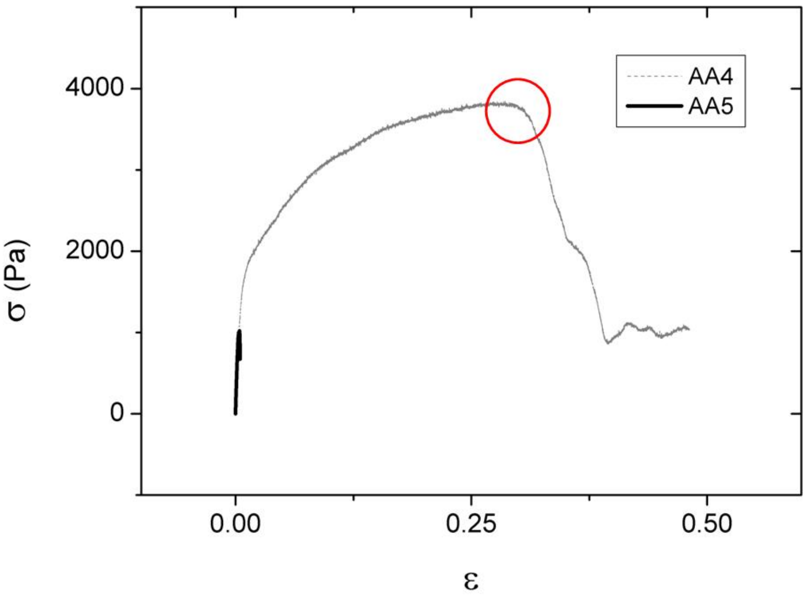

Figure 7.6: Stress-strain curves for shear experiments with surface hoar samples. The gray curve results from a slow experiment ($\dot{\epsilon} = 1.5 \times 10^{-4}\mathrm{s}^{-1}$, sample AA4), and the black curve was measured during a fast experiment (sample AA5, $\dot{\epsilon} = 1.3 \times 10^{-3}\mathrm{s}^{-1}$). The circle marks the region where sample AA4 failed.

Stress-strain curves for artificial depth hoar samples (samples of kind TRA, see Table 7.2) for different strain rates are shown in Fig. 7.7. Also here we see brittle behaviour at fast and ductile behaviour at slow strain rates.

Many (not all, see Table in Appendix B) layered samples collapsed vertically roughly at the same time they failed in shear (significant drop of shear force). Our measurement resolution did not allow us to clearly state whether the shear failure preceded the collapse or vice versa.

Sample TRA 70 is an example of a sample which obviously first failed in shear, and only at further deformation exhibited a vertical collapse. The stress-strain curve for sample TRA 70 is shown in Figure 7.8, together with the vertical displacement of the upper sample holder.

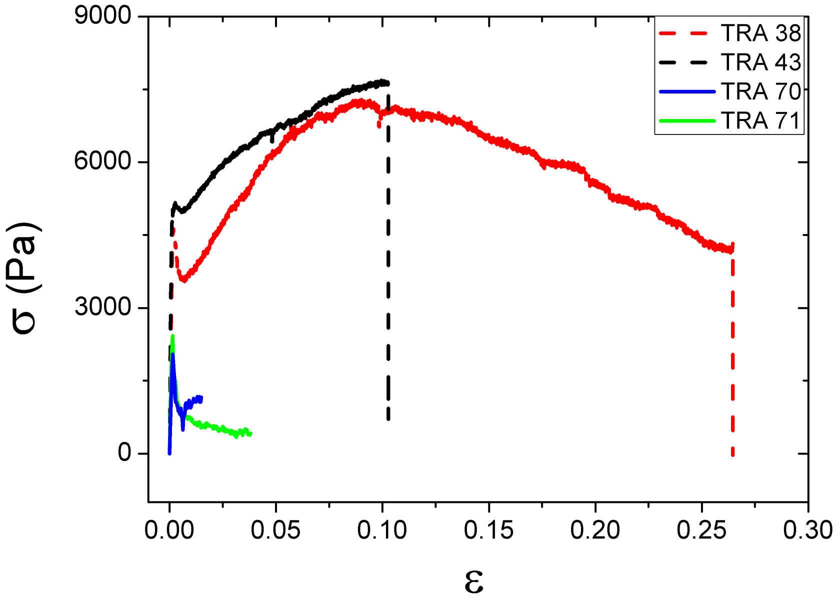

Figure 7.7: Stress-strain curves for shear experiments with artificial depth hoar samples (samples TRA). The strain rates were: $2.5 \times 10^{-4}\mathrm{s}^{-1}$ (sample TRA 38), $2.0 \times 10^{-4}\mathrm{s}^{-1}$ (sample TRA 43), $1.5 \times 10^{-3}\mathrm{s}^{-1}$ (sample TRA 70), and $1.4 \times 10^{-3}\mathrm{s}^{-1}$ (sample TRA 71).

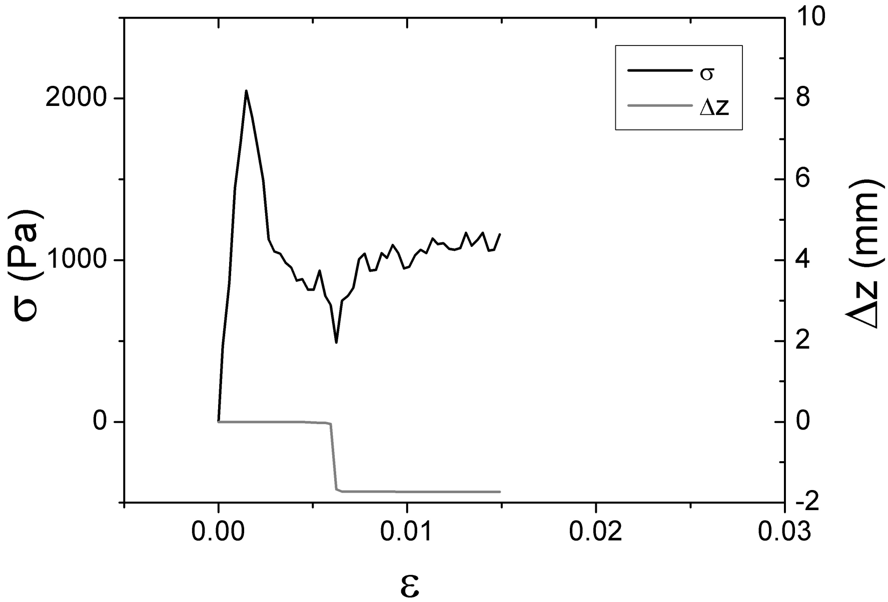

Figure 7.8: Stress, strain, and vertical displacement for sample TRA70.

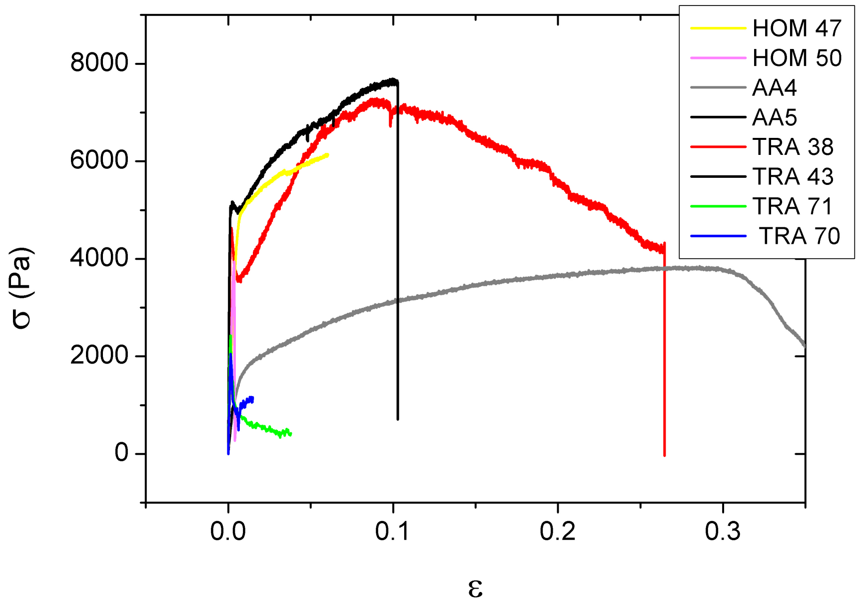

Figure 7.9: Summary of the results of the deformation-controlled experiments.

We note that there is no striking difference in the form of the stress-strain curves for layered and homogeneous samples. Also the strength of the homogeneous samples is not necessarily lower than for samples containing a 'weak' layer. In our examples, the strongest samples are layered depth hoar samples (Fig. 7.9), the homogeneous samples are slightly weaker , and the samples containing a surface hoar layer are weakest. Note that this cannot be generalized to surface hoar and depth hoar layers, i.e. surface hoar does not have to be weaker than depth hoar always, only for these two particular examples of weak layers this was the case.

Two qualitative differences between homogeneous and layered samples could be detected, though. First, the difference in strength between samples sheared at different strain rates was significantly higher in the case of the layered samples. Second, the fracture surface was always rough in the case of homogeneous samples, an example is given in Figure 7.10. Note that the crack has an uneven fracture surface. The crack is parallel to the sample holders in region B and runs at an angle of 45° (the direction of maximal tensile stress) to the sample holder in regions A. On the very left the crack continues at the top of the sample, very close but slightly below the sample holder.

Only for defined planes of weakness does a shear crack remain within its original plane. This was observed along the weak layers within the layered samples (at all strain rates). An example is given in Figure 7.11, where the upper sample holder was lifted after the sample had fractured.

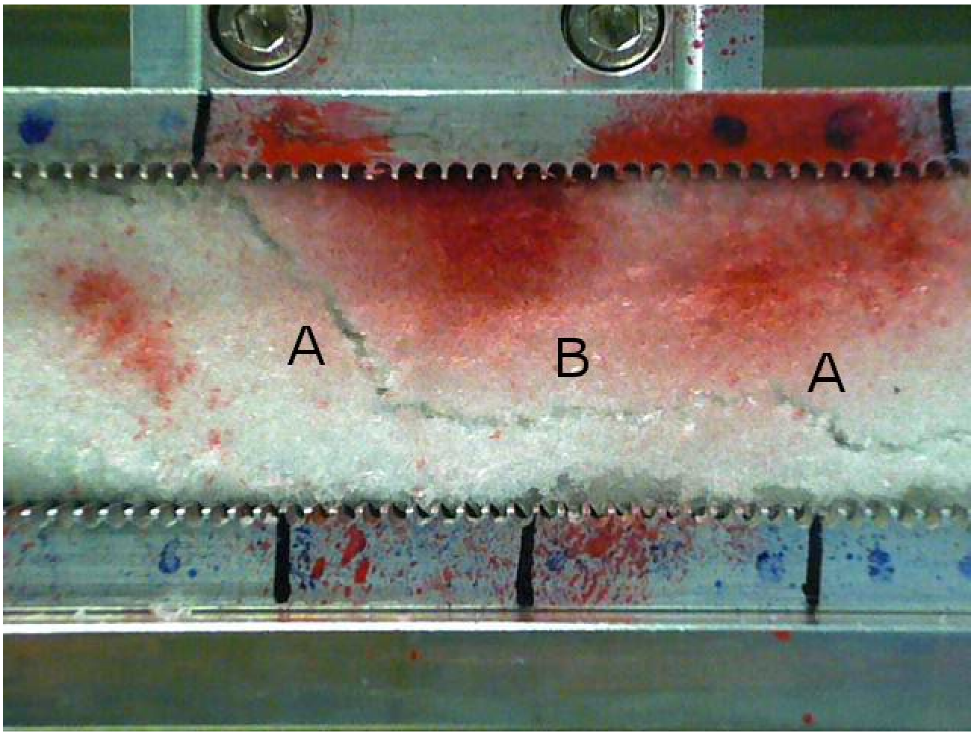

Figure 7.10: Uneven fracture surface of a homogeneous sample (sample HOM 35, see Table in Appendix B). The sample fractured in a brittle manner. The height of the sample was 3 cm. The letters A and B denote the different regions of the crack as described in the text.

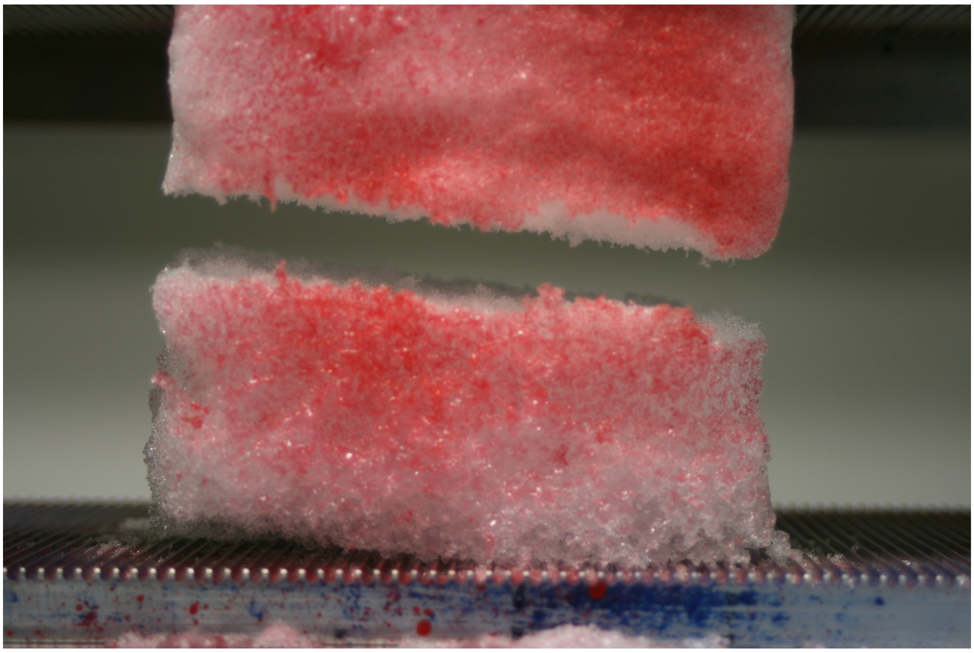

Figure 7.11: Even fracture surface of a layered sample (sample ORN 75, see Table in Appendix B). The height of the sample was 7 cm.

7.2.2 Concentration of deformation

Qualitatively, already photographs taken during experiments with relatively thick (10-15 mm) weak layers showed that the deformation was concentrated within the weak layer. Figure 7.12 shows two images taken during an experiment with a sample of type C (C6) which was marked with ink. It can be seen that the dots within the solid ellipses in the layers above and below the weak layer did not change their relative positions, i.e. there was hardly any deformation within these layers. The ink dots within the dashed ellipses in the weak layer obviously changed their relative positions, one can even see single grains that were tilted.

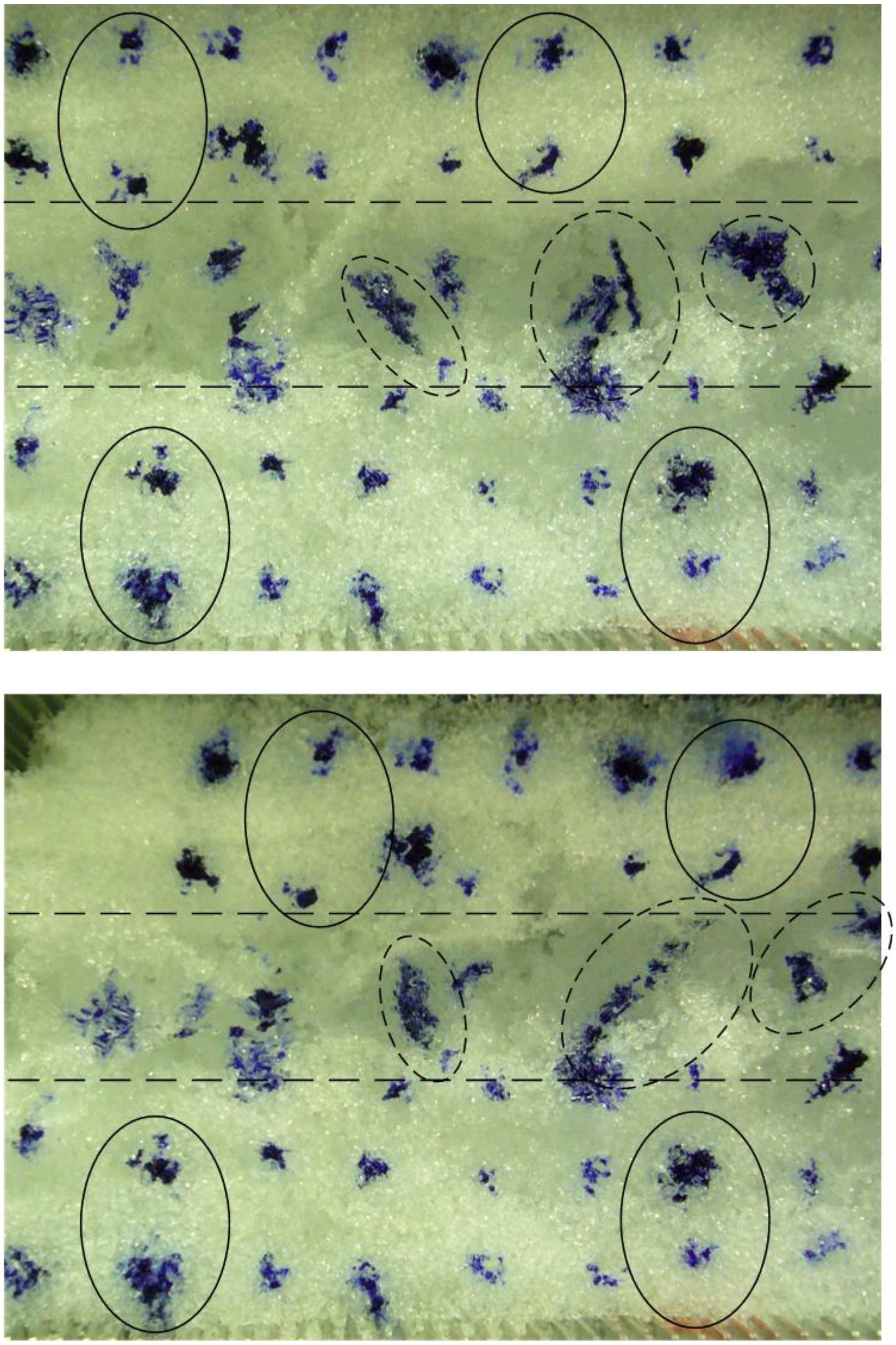

Figure 7.12: Deformation within a surface hoar sample (sample C6). The height of the weak layer (between the dashed lines) was 1 cm.

As we developed our PIV algorithm, the results from the ink dot pictures could be verified. This is illustrated with sample AA4. During the experiment with sample AA4, photos were taken, and the section shown in Figure 7.13 was analyzed with the PIV algorithm.

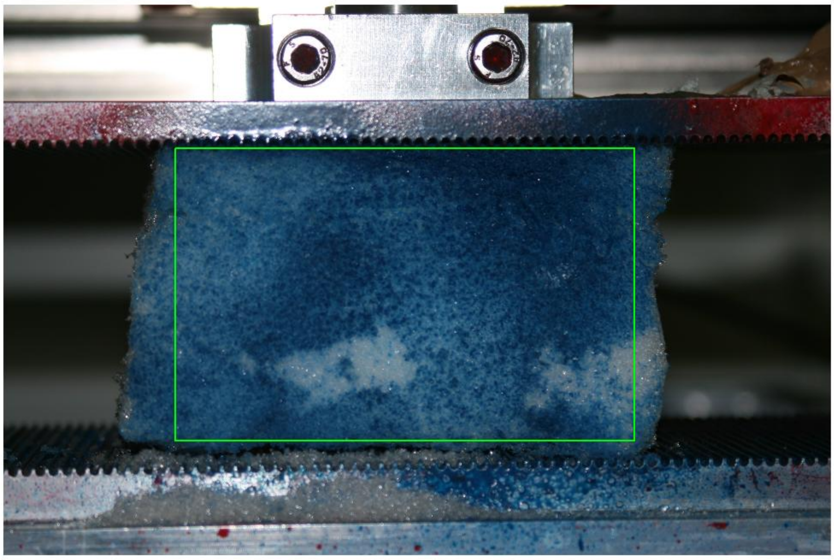

Figure 7.13: Section for PIV, sample AA4. The rectangle is 88 mm wide and 56 mm high.

The PIV results are shown in Figure 7.14. All the units given are in mm. The upper plot shows the displacement field derived with PIV. The lower plot shows the displacement field averaged over the horizontal direction. In the lower plot the strong displacement gradient within the weak layer (located at -18 mm of the ordinate) is best visible.

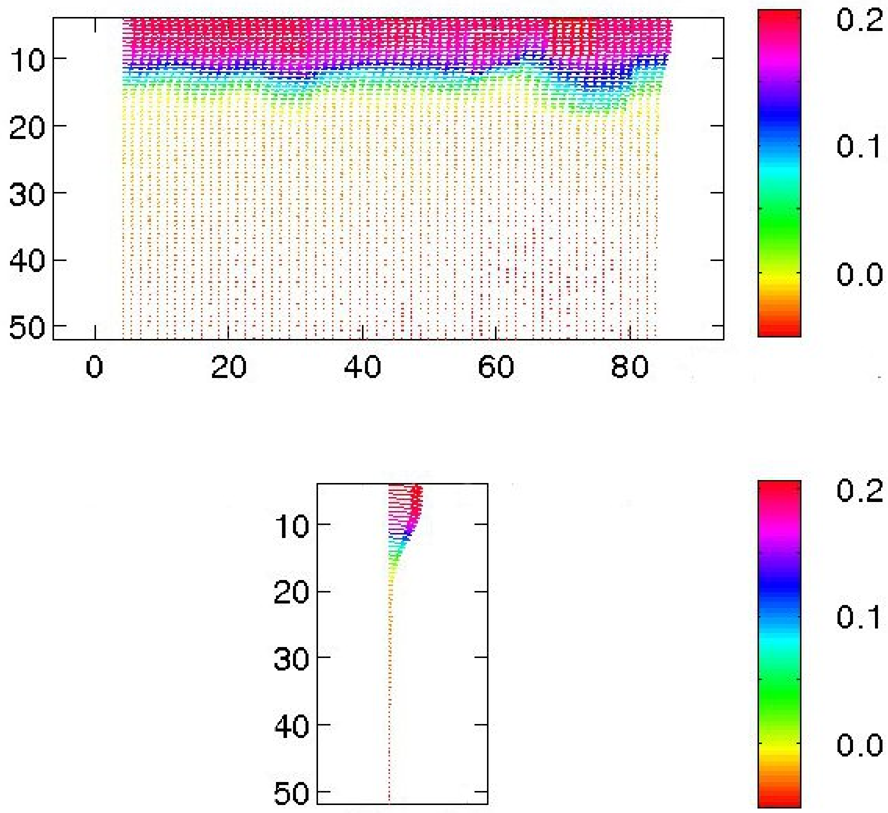

Figure 7.14: The displacement field of sample AA4 of the section shown in Figure 7.13. The lower plot shows the displacement averaged over the horizontal direction. All units given are mm.

7.2.3 Ductile-to-brittle transition

In Figure 7.15 we see the fracture stress[3] of the layered samples summarized in Table 7.2 plotted over the strain rate within the weak layer. For samples of type C and TRA, for which we performed the shear experiments before the PIV algorithm was developed, we assumed all deformation to be concentrated within the weak layer. For samples of type A and B this concentration of deformation was verified with PIV.

We see that the strength of the samples is consistent at all strain rates, i.e. sample type TRA is strongest, followed closely by sample type B. Samples of type A and C are significantly weaker. We find ductile behaviour at strain rates smaller than roughly $3-5\times10^{-4}\mathrm{s}^{-1}$ (which corresponds to strain rates of roughly $3-5\times10^{-3}\mathrm{s}^{-1}$ within the weak layer) and brittle behaviour at larger strain rates.

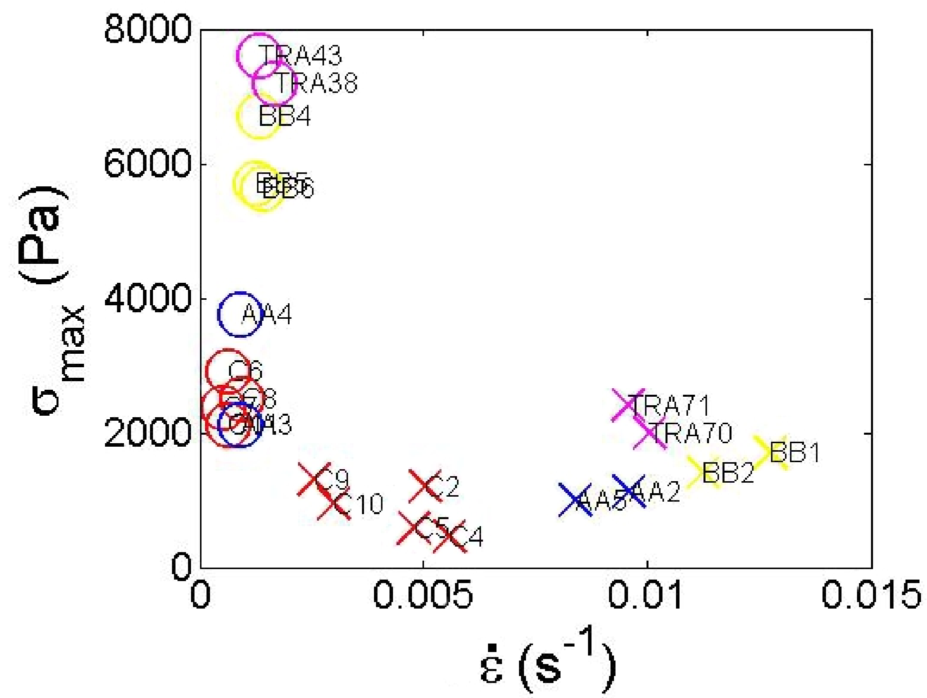

Figure 7.15: Fracture stress over strain rate within the weak layer for different kinds (colours of markers) of layered samples, namely samples of kind A, B, C, and TRA. Crosses depict brittle and circles depict ductile failure behaviour. The results are also summarized in Table 7.2, N = 22.

[3] As a proxy for the strain rate within the weak layer, we take 10 times the global strain rate. Within samples of type B, the deformation was concentrated at the interface of the weak layer and the crust below and sometimes the layer above.

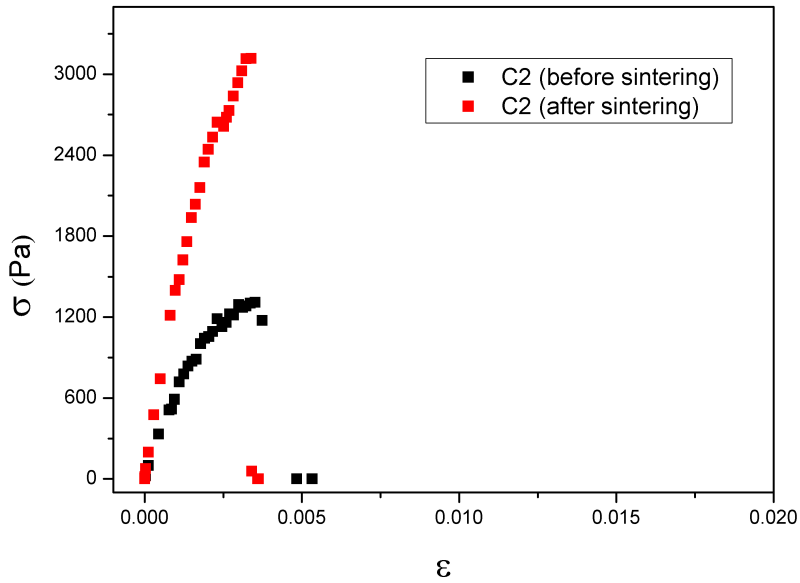

Figure 7.16: Stress-strain curves of natural surface hoar sample C2, sheared two times and left to sinter in between.

7.2.4 The effect of sintering

Several samples were left to sinter in the apparatus after they had broken, and were then sheared again (see Table in Appendix B, experiments 3, 9, 15, 18, 39, 53a, and 55a). Sample 55a had a lower shear strength the second time it was sheared, but this was because the strain-rate was higher by a factor of 5 at the second experiment. All other re-sintered samples had significantly higher shear strengths after the weak layer had fractured and re-sintered. In figure 7.16 the stress-strain curves of the natural surface hoar sample C2 (this corresponds to experiments 2 and 3 in Appendix B) are shown, between the two experiments the sample was left in the apparatus to resinter. It is evident that the failure strain does not change between the two experiments but the failure stress increases significantly after sintering.

7.3 Force-controlled experiments: layered versus homogeneous samples

For this set of experiments we used two different types of samples: homogeneous (H1) and layered (L1). Both types of samples were produced in the cold laboratory. An overview of the samples' properties is given in Table 6.2. The tilt angle α of the loading apparatus was fixed to 26 °, and the laboratory temperature was -6 °C.

Our experimental setup was designed to mimic loading conditions for a snowpack in nature, this makes it relevant for avalanche release but also difficult to compare to standard mechanical test procedures. The 'normalized loads' we refer to within this and the following sections are the loads divided by the upper area of the samples, independent of the slope angle. We use this quantity as a measure of sample strength since we feel it is the most relevant for avalanche release.

Typical stress (load divided by area) and strain (displacement divided by height) curves during a loading experiment with a homogeneous sample (H1, see Table 6.1) can be seen in Figure 7.17. All our samples had an area of the same order of magnitude (approximately 10 cm $\times$ 15 cm). In order to account for small differences in area due to sample preparation, we show the normalized load $\tilde{\sigma}$, i.e. the load divided by sample area. The sample was loaded with a constant rate of 0.5 kN m^{-2} s^{-1} and failed catastrophically at $t = 38$ s with a normalized load at fracture $\tilde{\sigma}_\mathrm{c} = 16$ kN m^{-2}. The strain in z-direction (see Fig. 6.5) was compressive, and the shear strain (in x-direction) was in 'slope downward' direction. Both strain curves stay constant after fracture, and the shear strain curve displays a drop of strain during fracture, but these are artifacts due to the limited range of the displacement sensors and the movement of the upper sample holder during fracture, respectively. The compressive and shear strain on a larger scale can be seen in Figure 7.18. The noise is due to vibrations of the apparatus during loading and is not a physical effect.

The compressive stress, shear stress, compressive strain, and shear strain of an experiment with a layered sample (L1, see Table 6.2) are shown in Figure 7.19. Qualitatively, the

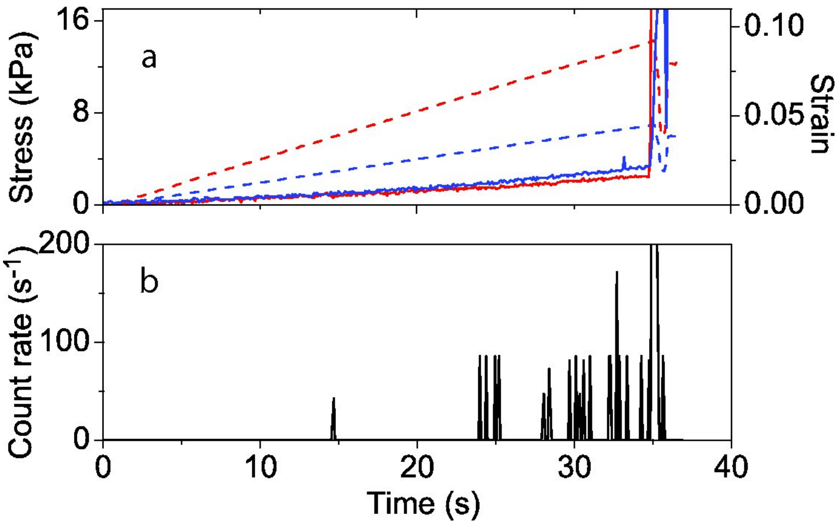

Figure 7.17: (a) Compressive stress (red dashed curve), shear stress (blue dashed curve), compressive strain (red solid curve), shear strain (blue solid curve), and (b) acoustic emissions (count rate) measured during a loading experiment with a homogeneous snow sample (H1, Table 6.2).

results look similar as in the experiment with the homogeneous sample. The sample fractured earlier, though, at $t = 12$ s and at a much smaller normalized load, $\tilde{\sigma_c} = 5$ kN m^{-2}. The applied normalized loading rate was 0.46 kN m^{-2} s^{-1}, the difference in loading rate was mainly due to the slightly different areas of the samples.

Figure 7.21 shows the displacement within the homogeneous sample between two photographs taken at 4 and 10 seconds before fracture, respectively. It can be seen that both the shear and the compressive strain were spread uniformly over the whole sample. The shear strain, i.e. the displacement gradient (change in displacement over height) in slope parallel direction, had a constant value of 2.5×10^{-3} ($\epsilon = \frac{\Delta}{h} = \frac{0.12 \text{ mm}}{48 \text{ mm}}$).

Figure 7.20 shows a photograph of the layered sample in the loading apparatus. The rectangle (35 mm $\times$ 63 mm) marked on the sample indicates the section which was used for the PIV analysis. The displacement field in the center of this rectangle can be seen in Figure 7.21. The weak layer was located parallel to the sample holders (direction of Δx, Fig. 6.5) and its vertical position was between 0 and -1 mm. Again we compared two photographs taken at 4 and 10 seconds before fracture. Clearly, both the shear and the compressive strain were concentrated within the weak layer, where we locally measured a displacement gradient in shear of 4×10^{-2}, while it was around 3×10^{-4} elsewhere. This gives a shear strain rate of 7×10^{-3} s^{-1} within the weak layer, while the global shear

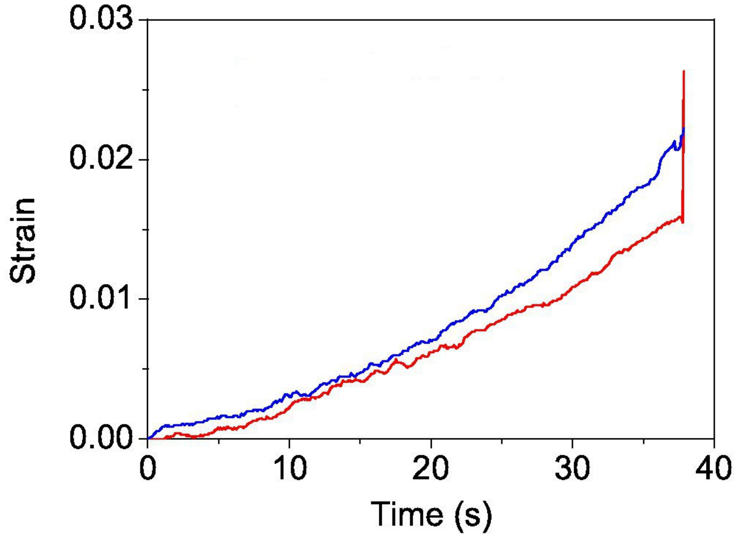

Figure 7.18: Compressive (red curve) and shear strain (blue curve) for the experiment with the homogeneous sample (Fig. 7.17), before the huge increase of strain at fracture.

strain rate was only about 2×10^{-4} s^{-1}.

Due to the finite size of the interrogation window of the PIV analysis, the strain within the (thin) weak layer is smeared out, i.e. we see a smaller displacement gradient over a larger height than the height of the weak layer, see e.g. Figure 7.21). This can be solved by measuring the global strain and the strains within the upper and lower layers (this can be done by PIV) and calculating the strain in the weak layer as described in Section 7.4.1.

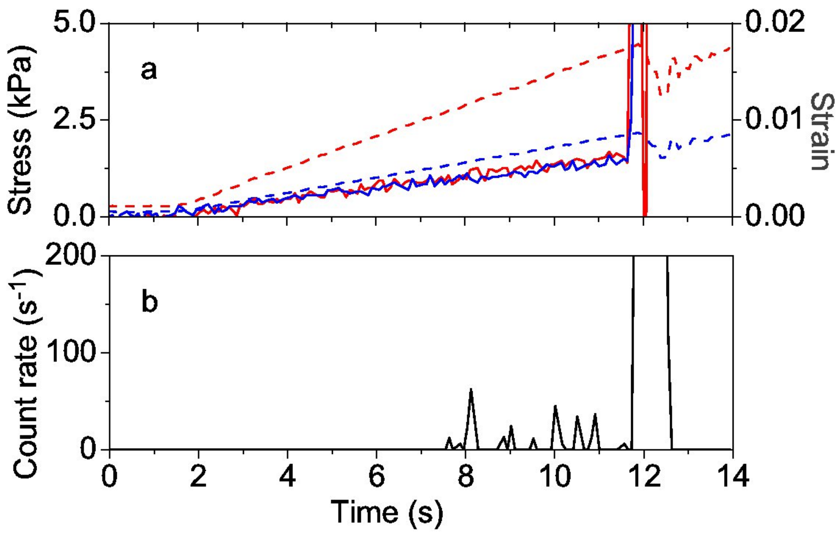

Figure 7.19: (a) Compressive stress (red dashed curve), shear stress (blue dashed curve), compressive strain (red solid curve), shear strain (blue solid curve), and (b) acoustic emissions (count rate) measured during a loading experiment with a layered snow sample (L1, Table 6.2).

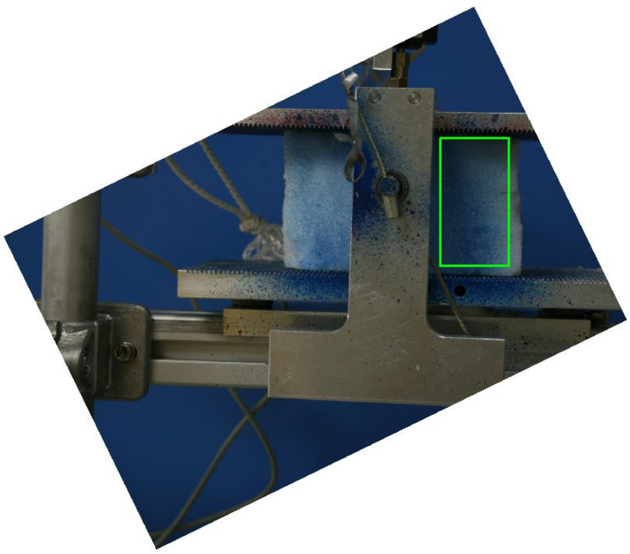

Figure 7.20: Photograph of the layered snow sample L1 during the loading experiment (Fig. 7.19) with the section marked which was used for the PIV analysis.

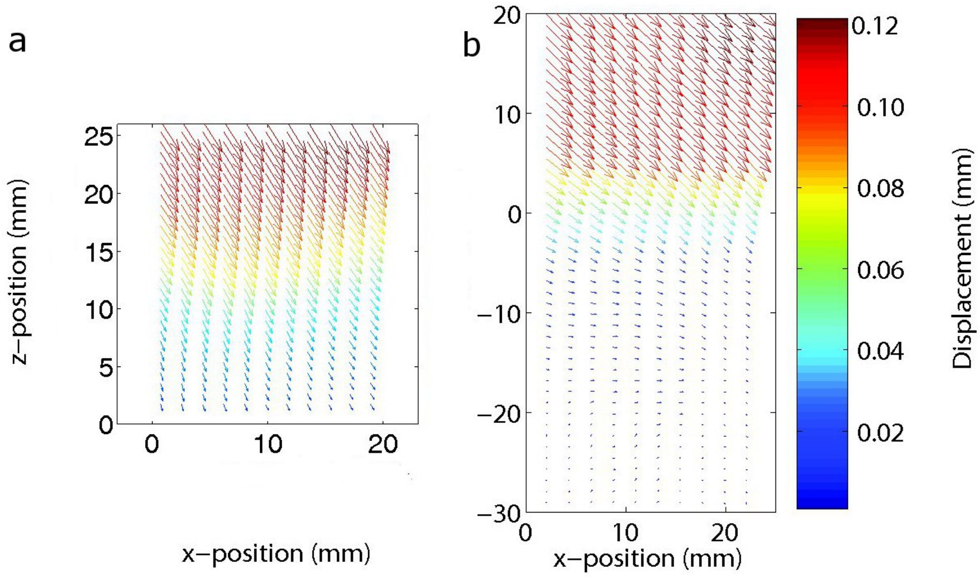

Figure 7.21: Displacement field on the side of the homogeneous snow sample H1 (a) and the layered snow sample L1 (b) obtained by PIV analysis during loading experiments.

7.4 Force-controlled experiments with surface hoar

An overview of loading experiments performed with surface hoar samples of type A (Table 6.1) is given in Table 7.3. The laboratory temperature was set to -6 °C for all experiments. We performed 19 experiments with samples of type A, only 10 of them were of use, the other samples broke during mounting. The results presented in this section have already been published in Reiweger and Schweizer (2010a) and Reiweger and Schweizer (2010b). Parts of the results presented here have already been published in Reiweger and Schweizer (2010b) and Reiweger and Schweizer (2010a).

Table 7.3: Overview of loading experiments performed with samples of type A. The symbols α, $\dot{\tilde{\sigma}}$, and $\tilde{\sigma_c}$ denote the slope angle, the normalized loading rate, and the normalized load at fracture, respectively.

Sample	α (°)	$\dot{\tilde{\sigma}}$ (N m^{-2} s^{-1})	$\tilde{\sigma_c}$ (kN m^{-2})
A1	25	9	0.84
A2	25	12	0.50
A3	25	1	>7
A4	35	20	0.36
A5	35	3	0.61
A6	35	21	0.26
A7	35	3.3	0.50
A8	25	3	>7
A9	15	21	1.9
A10	15	20	2.6

Figure 7.22 shows results of shear strain and stress, and compressive strain and stress for two experiments, with a slow (A5) and a fast (A6) loading rate, respectively. For all experiments the shear strain was substantially larger than the compressive strain, although the compressive stress was always larger than the shear stress (as the slope angle was always <45 °). No dilatancy was observed, i.e. the slope-normal deformation was always compressive. The acoustic count rate and cumulative count rate for the same two samples (A5 and A6) are shown in Figure 7.23. For the fast experiments, we in general observed only few events before fracture, while for the experiments at the slow loading rate, the slope of the cumulative count rate usually increased at the beginning of the loading process and shortly before fracture.

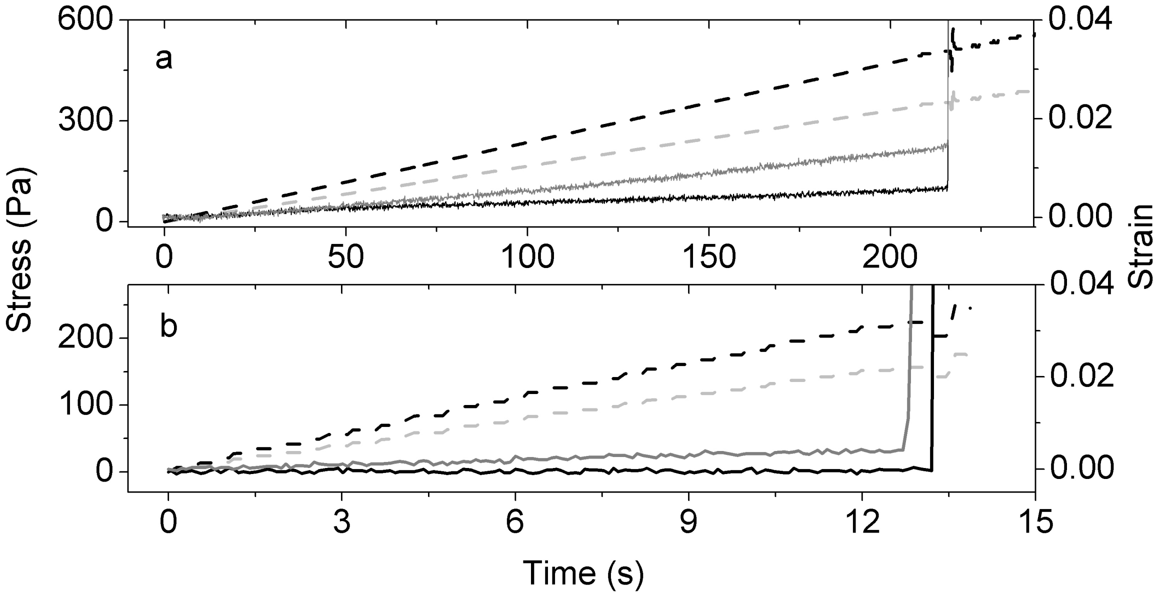

Figure 7.22: Typical stress (dashed) and strain (solid) curves for (a) a slow (sample A5) and (b) a fast (sample A6) loading experiment ('slope angle': 35°). The black lines indicate the compressive stress and strain, the gray lines the shear stress and strain.

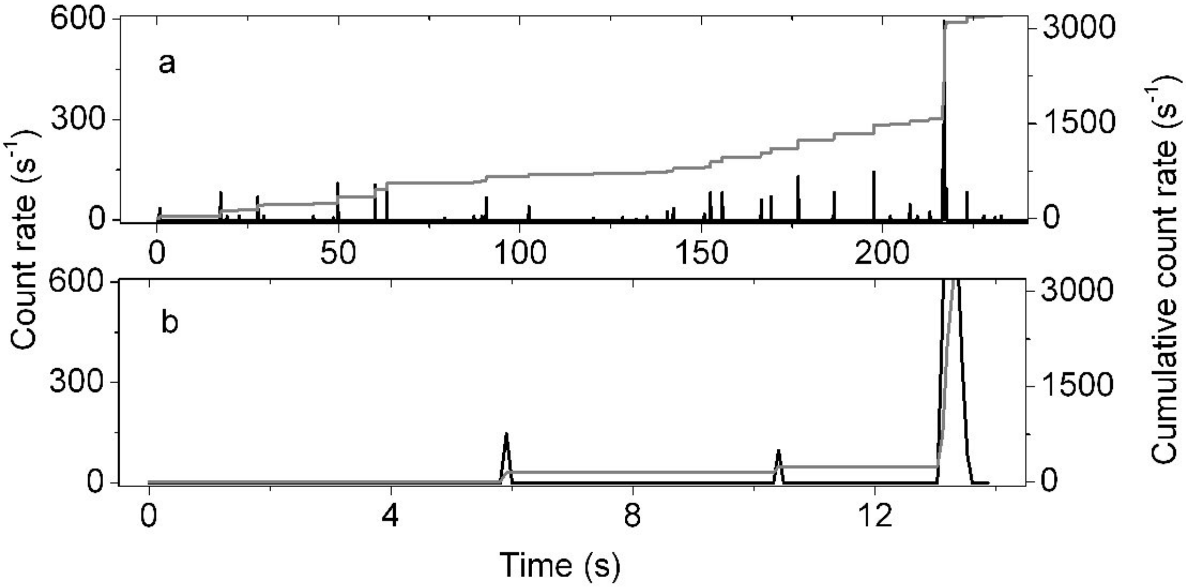

Figure 7.23: Acoustic count rate (black) and cumulative count rate (gray) for (a) a slow (sample A5) and (b) a fast (sample A6) loading experiment.

7.4.1 Concentration of shear deformation

The total shear strain, the shear strain in the upper layer, and the shear strain in the lower layer can straightforwardly be obtained with PIV. From now on, within this paragraph 'shear strain' is denoted by 'strain' only. The resolution of the PIV is too small for measuring the strain in the weak layer directly, but it can easily be calculated. If all other strains are known, the strain in the weak layer can be calculated via

$$\epsilon_{\mathrm{WL}} = (\epsilon_{\mathrm{tot}} \times h_{\mathrm{tot}} - \epsilon_{\mathrm{u}} \times h_{\mathrm{u}} - \epsilon_{\mathrm{l}} \times h_{\mathrm{l}})/h_{\mathrm{WL}}, \tag{7.1}$$

where ϵ denotes the strain, h denotes the height and the indices u/l/WL/tot stand for upper/lower/weak layer/total, respectively. The strain in the weak layer compared to the total strain is

$$\frac{\epsilon_{\mathrm{WL}}}{\epsilon_{\mathrm{tot}}} = \frac{\Delta_{\mathrm{WL}}}{\Delta_{\mathrm{tot}}} \times \frac{h_{\mathrm{tot}}}{h_{\mathrm{WL}}}. \tag{7.2}$$

where Δ denotes the displacement. This means that $\frac{\epsilon_{\mathrm{WL}}}{\epsilon_{\mathrm{tot}}}$ is a linear function of $\frac{h_{\mathrm{tot}}}{h_{\mathrm{WL}}}$ and the factor $\frac{\Delta_{\mathrm{WL}}}{\Delta_{\mathrm{tot}}}$ is a measure of concentration of deformation within the weak layer. If all the deformation was concentrated in the weak layer, i.e. $\Delta_{\mathrm{WL}} = \Delta_{\mathrm{tot}}$, the plot of $\frac{\epsilon_{\mathrm{WL}}}{\epsilon_{\mathrm{tot}}}$ over $\frac{h_{\mathrm{tot}}}{h_{\mathrm{WL}}}$ would be a straight line with slope 1.

Figure 7.24 shows the shear strain within the weak layer (measured indirectly by PIV) divided by the total strain (both measured shortly before fracture) as a function of the inverse relative thickness of the weak layer $h_{\mathrm{tot}}/h_{\mathrm{wl}}$. Figure 7.24 also includes data from displacement-controlled shear experiments; these three samples consisted of the same snow types and had the same properties as samples A1-A10 (Table 1). The slope of the fitted line was 0.87 (standard error: 0.02), which means that on average almost 90% of the shear strain was concentrated within the weak layer. This is remarkable, since the samples of type A had very soft layers above and below the weak layer, and we initially had expected a fair amount of deformation there. For compressive strain, no concentration of strain within the weak layer was observed.

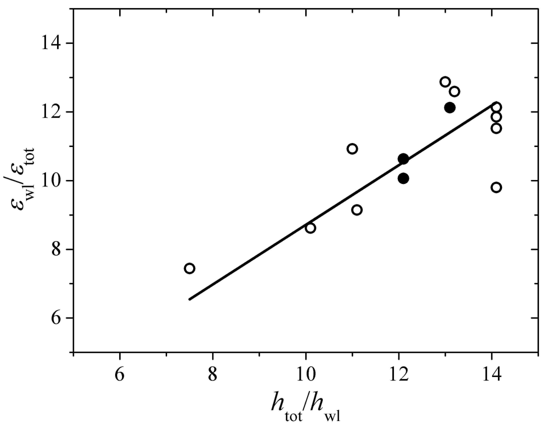

Figure 7.24: Relative shear strain within the weak layer as a function of the inverse relative thickness of the weak layer. The red data points are from force-controlled experiments, the pink data points are from displacement-controlled experiments (N = 13).

7.4.2 Influence of loading rate and slope angle on the strength of a surface hoar layer

Due to the limited number of natural samples we could only perform two tests for one set of parameters (loading rate and 'slope angle'). The results of the successful experiments are compiled in Table 7.4. At the fast loading rate (> 3 N m^{-2} s^{-1}), most samples fractured within several tens of seconds. Two of the four samples tested at the slow loading rate (3 N m^{-2} s^{-1}) did not fail before the maximum possible load was reached, namely those for $\alpha = 25\,°$. Only the samples loaded at the steeper 'slope angle' fractured. In general, the normalized load at fracture decreased with increasing 'slope angle' (Fig. 7.25).

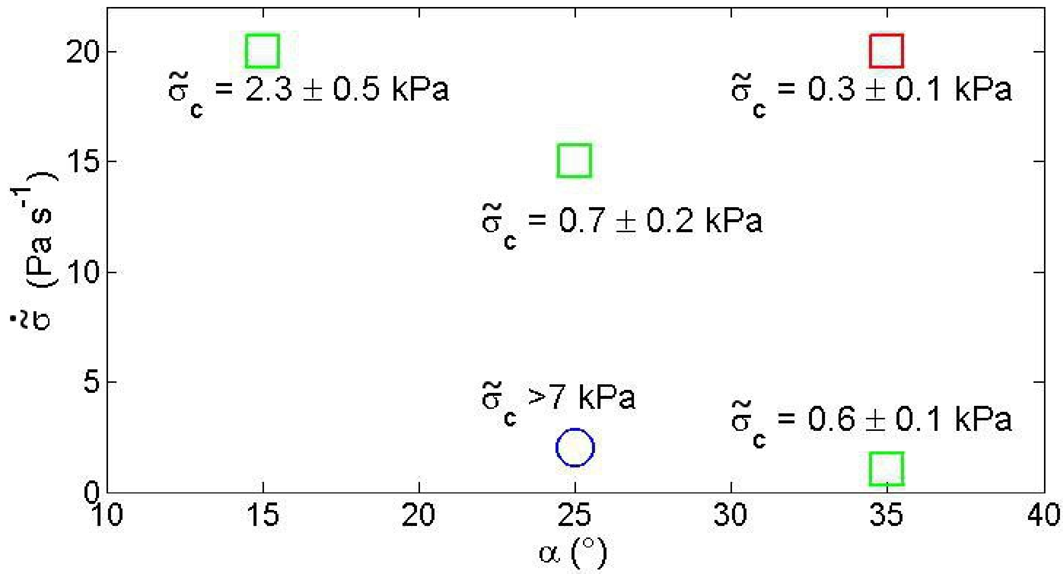

Figure 7.25: Normalized load (load divided by upper area of the sample) at fracture $\tilde{\sigma_c}$ as a function of loading rate and slope angle for samples of type A. Squares denote fracture, while the circle denotes no apparent fracture. The colors illustrate the magnitude of the normalized load ($N = 10$).

For a given slope angle the normalized load at fracture decreased with increasing loading rate. Shear strain at fracture ranged from 0.4 to 7% depending on loading rate and slope angle. The global (sample average) shear strain rates were between 8×10^{-5} and 7×10^{-4} s^{-1}. These strain rates are smaller than the critical strain rate for the ductile-to-brittle transition commonly reported for homogeneous snow samples (e.g. Schweizer, 1998), but agree quite nicely if we consider the strain rates within the weak layer, which are an order of magnitude larger than the global strain rates.

7.5 Force-controlled experiments with depth hoar

Finally we performed a series of loading experiments with samples of type B. An overview of loading experiments performed with samples of type B (Table 6.1) is given in Table 7.4. Again, the laboratory temperature was set to -6 °C for all experiments. We performed 30 experiments with samples of type B, 17 of them were of use, the other samples broke during mounting.

Table 7.4: Overview of loading experiments performed with samples of type B. α, $\dot{\tilde{\sigma}}$, and $\tilde{\sigma}_c$ denote the slope angle, the normalized loading rate (force per sample area per time), and the normalized load at fracture, respectively.

Sample	α (°)	$\dot{\tilde{\sigma}}$ (N m^{-2} s^{-1})	$\tilde{\sigma}_c$ (kN m^{-2})
B1	25	42	1.6
B2	25	200	0.7
B3	25	84	2.4
B4	25	9	2.3
B5	25	14	2.0
B6	35	10	3.8
B7	35	200	1.0
B8	35	200	1.2
B9	35	18	1.7
B10	35	20	0.8
B11	0	444	2.7
B12	0	439	2.5
B13	0	30	2.5
B14	0	15	2.5
B15	25	290	1.3
B16	0	42	6.0
B17	25	220	1.7

Figure 7.26 shows stress, displacement, and acoustic emissions for a loading experiment with a sample of type B (B2) with slope angle $\alpha = 25°$. We see that the shear strain changed before the compressive strain did, i.e. the complete collapse of the sample happened after a significant movement in shear direction. Before fracture, we recorded virtually no acoustic emissions. Both was typical for samples of type B.

All samples of type B failed catastrophically, at all slope angles and with all loading rates

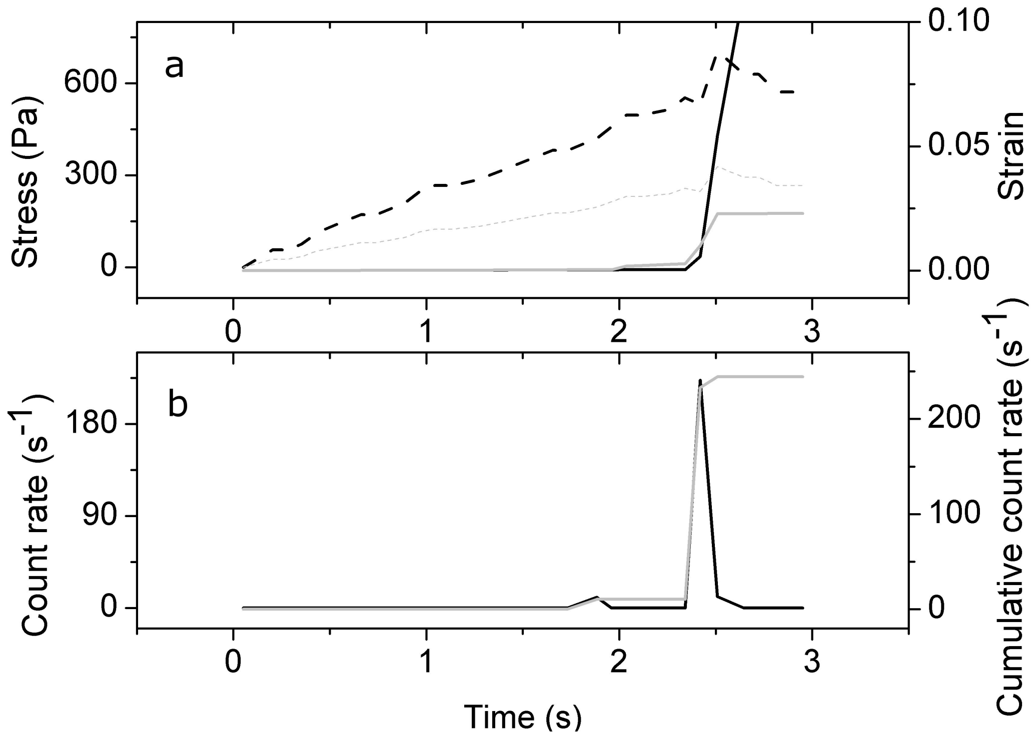

Figure 7.26: (a) Typical compressive stress (black, dashed), shear stress (gray, dashed), compressive strain (black, solid), shear strain (gray, solid), and (b) acoustic emissions (count rate: black, cumulative count rate: gray) over time for a loading experiment with a depth hoar sample (sample B2). The slope angle α was 25°.

we tested. Every time the weak layer fractured. We studied the deformation before failure with PIV measurements. With these measurements we could always see the deformation was fairly equally spread within the weak layer and there was a slight concentration of deformation at the interface between the weak layer and the crust below (see Fig. 7.27). Since we assume plane strain conditions, the strain should be constant over the y-direction (direction perpendicular to the figure).

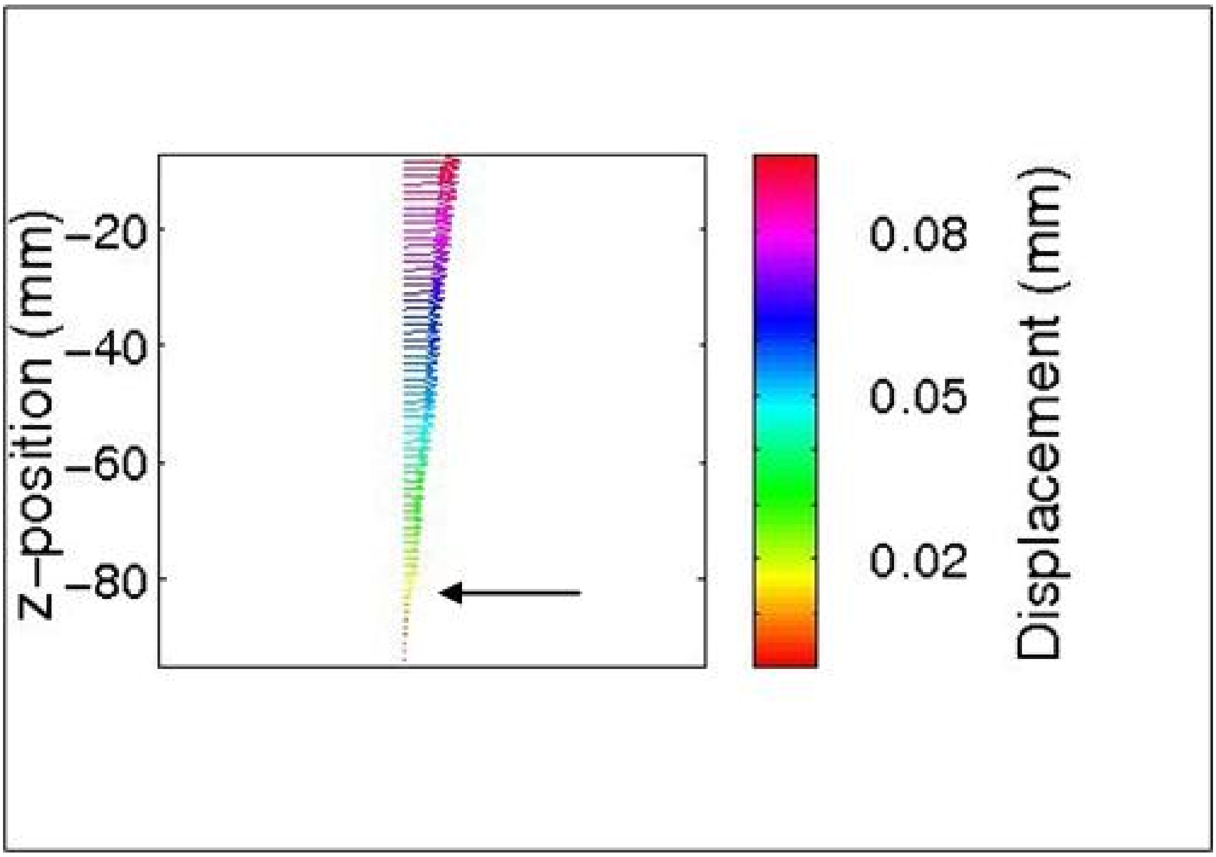

Figure 7.27: The displacement field of a snow sample of type B (B2) during a loading experiment before final fracture, averaged over the x-direction. The arrow marks the position of the weak interface.

7.5.1 Influence of loading rate and slope angle on the strength of a depth hoar layer

Figure 7.28 shows the normalized load at fracture $\tilde{\sigma_c}$ depending on loading rate and slope angle for samples of type B. The average size of the samples tested (length×width×height) was 150 mm×115 mm×110 mm. Again, each data point consists of two measurements each. Here we see only a weak dependence of the load at fracture on the loading rate and the slope angle.

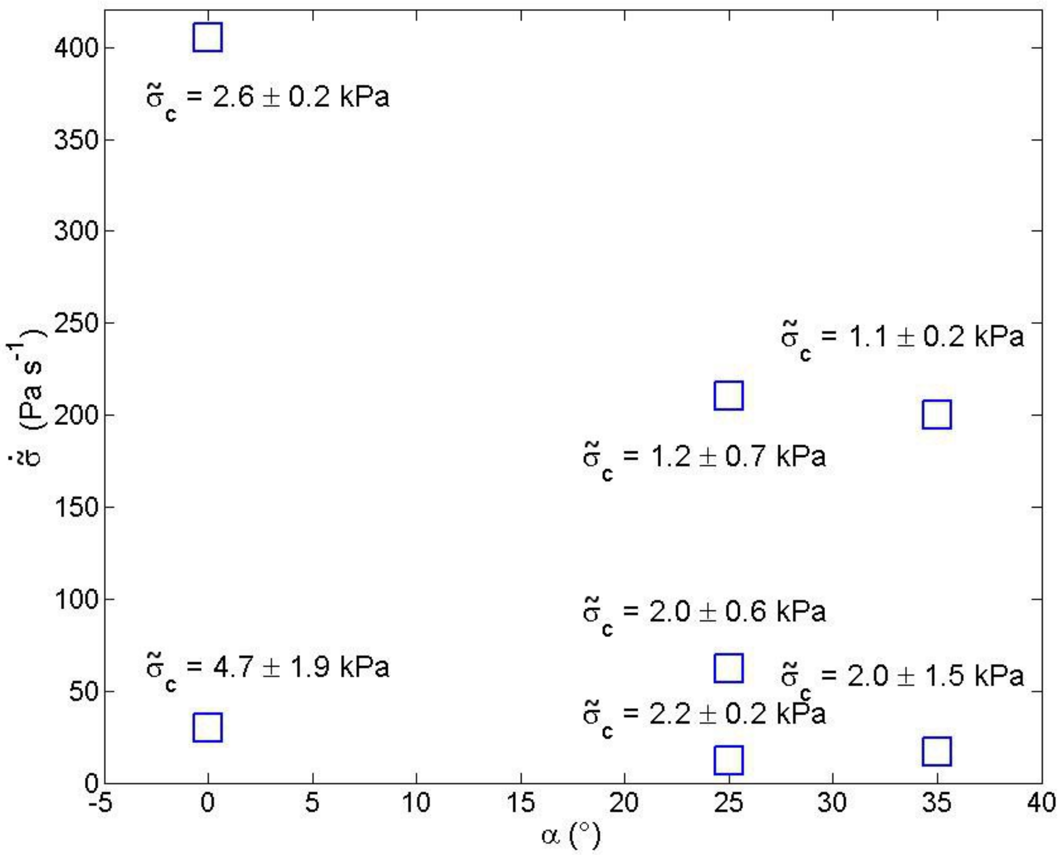

Figure 7.28: Normalized load at fracture $\tilde{\sigma_c}$ dependent on loading rate and slope angle for samples of type B.

7.5.2 Studying the fracture process with high-speed camera measurements

For measurements B8, B9, B10, and B17 we recorded the experiments, in particular the fracture process, with a high speed camera. Since this weak layer was thick we could observe what was happening within the weak layer shortly before and during fracture.
The high speed images show that a small fracture happened at an arbitrary place within the weak layer, and this fracture then triggered a shear crack at the interface between the weak layer and the crust at the bottom. This crack propagated through the whole sample (in x-direction) and caused the samples to fail catastrophically. Note that this weak layer was very thick, as is common with depth hoar layers in a natural snowpack. The approximate location of the weak layer within the sample is depicted in Figure 7.30. An overview of the times the different images were taken is given in Figure 7.29. Only the last image (Fig. 7.42) is not shown on this Figure; it was taken 1 s after the first image.
The PIV analysis of the 33 images before and after the onset of the final crack taken with the high speed camera during the experiment with sample B9 allow us to exactly follow the failure and fracture process. The time difference between two subsequent images was $\frac{1}{300}$ s. The PIV analysis always shows the displacement between the first of the 33 images and image i, where $i = 2, \ldots, 33$. Note that both series of PIV results show the displacements at the same times, but at different locations, namely within the upper search window shown in Figure 7.30 for the first series and within the lower search window shown in Figure 7.35 for the second sequence. The first series of PIV results (Figs. 7.31, 7.32, 7.33, and 7.34) shows the displacement caused by the local fracture at the top, while the second series of images (Figs. 7.36, 7.37, 7.38, and 7.39) shows the PIV results of the onset of the final crack at the bottom.
The seemingly chaotic and even upward movement during fracture (Figs. 7.31, 7.32, 7.33, and 7.34) reflects the layer being crushed and pieces of snow being pressed out of the sample sideways.
A small fracture at the top (Figs. 7.30 and 7.31) triggered another local failure lower down (Fig. 7.31, image 7) and even later a failure at the interface between the weak layer and

the crust below (Figs. 7.35 and 7.39). This failure grew to a macroscopic crack which propagated through the whole sample (in x-direction, 0.1 s after the first local failure). Figures 7.36, 7.37, and 7.38 illustrate that the lower part of the sample was not affected by the local failure at the top right away. The disturbance at the top reaches the bottom only in image 26 (Fig. 7.39). The sample then moved in slope downward direction, and during this movement the whole weak layer collapsed.

The fracture at the bottom propagated through the whole sample (in x-direction) and caused the sample to break apart. Figure 7.40 shows an image of the sample taken 0.2 s after the images shown in Figures 7.30 and 7.35. We see that the upper part of the sample moves more or less as a cohesive block and the fracture plane is clearly within the plane where the fracture started (Fig. 7.35).

The image of sample B9 0.3 s after the image shown in Figures 7.30 and 7.35 (which were taken $\frac{1}{100}$ s before the first local failure at the top) is displayed in Figure 7.41. The upper and lower parts of the sample are still fairly intact, but the weak layer is squashed and the snow has crumbled away sideways. The final image of the high speed camera sequence (Fig. 7.42), taken 1 s before the images in Figures 7.30 and 7.35, shows the sample holders after 'the avalanche has released'.

We see a similar mechanism in the high speed videos from samples B8, B10, and B17.

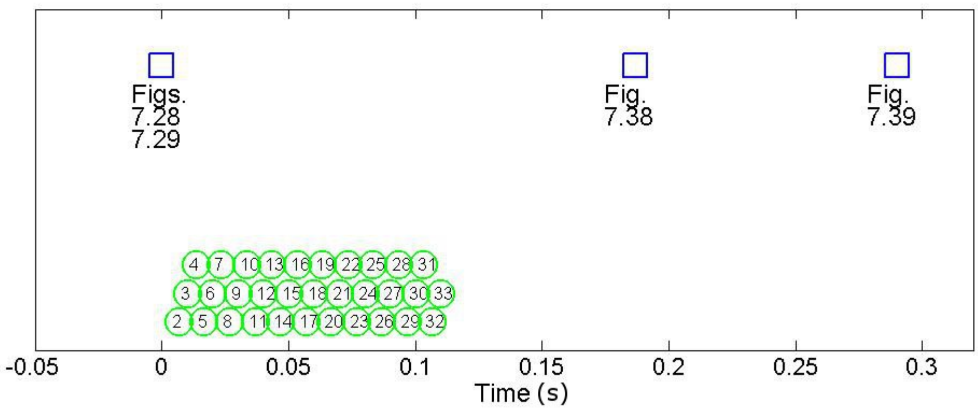

Figure 7.29: Overview of times when images were taken. The squares represent the photos in the respective Figures, while the circles represent the averaged displacement fields shown in Figures 7.31, 7.32, 7.33,7.34, 7.36, 7.37, 7.38, and 7.39.

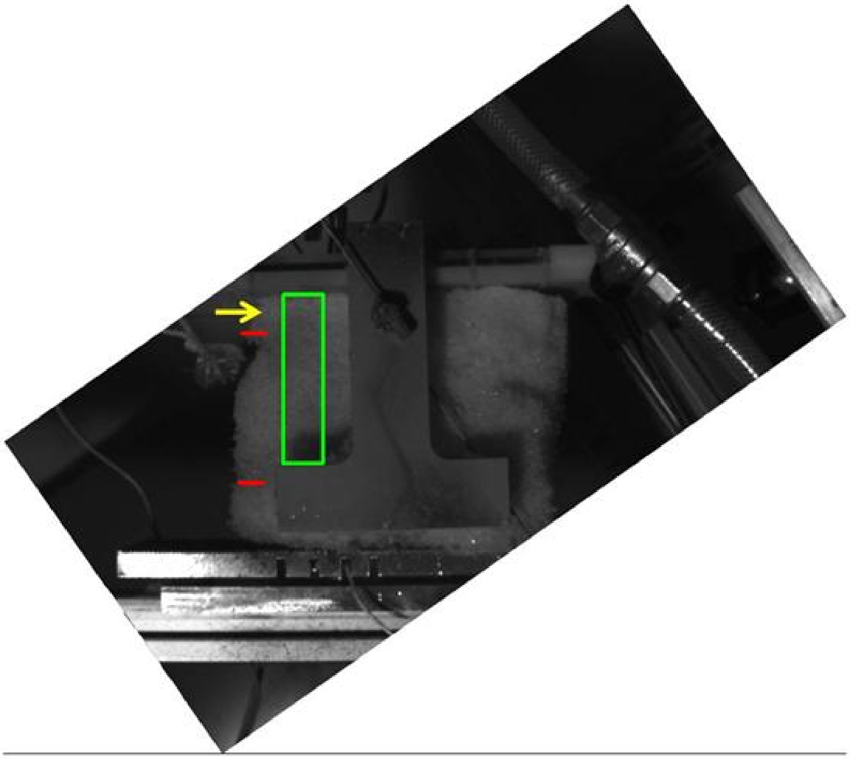

Figure 7.30: Section where first local failure happened, sample B9. The arrow marks the place of failure. the weak layer is approximately located between the two red lines, and the rectangle is 22 mm wide and 87 mm high. The slope angle α was 35°.

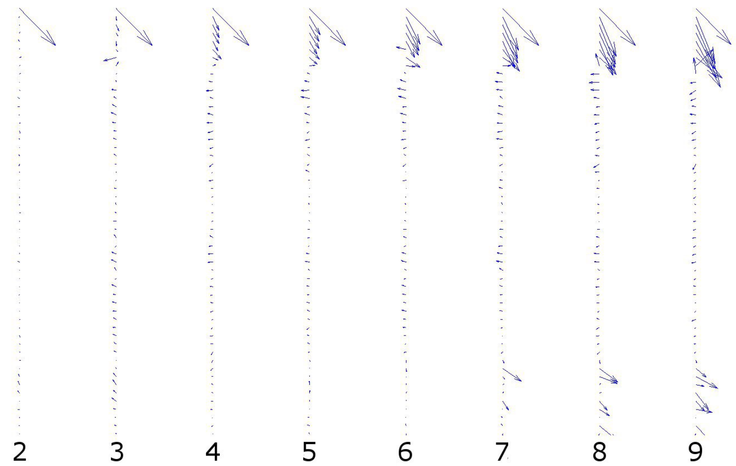

Figure 7.31: Local failure at the top of the sample, sample B9. The PIV analysis is for the section shown in Fig. 7.30 and shows the displacement between the first image and images 2-9. The displacement is averaged in the x-direction. The uppermost arrow in each sequence is only for reference, its coordinates are [0.8 mm, 0.8 mm].

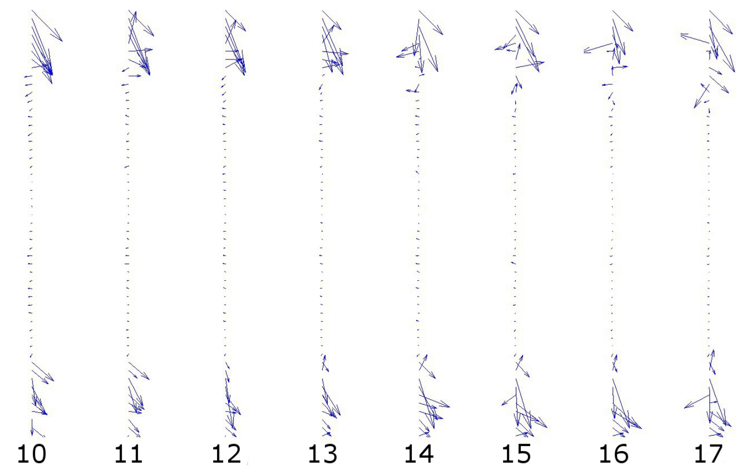

Figure 7.32: As Figure 7.31, but displacement between image 1 and images 10-17.

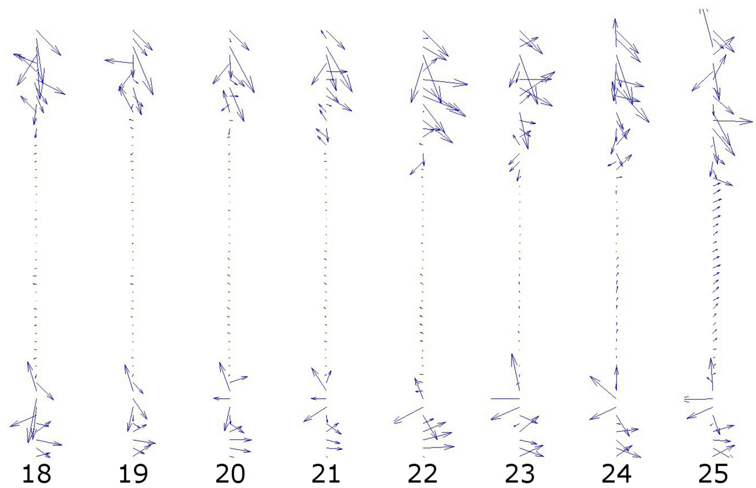

Figure 7.33: As Figure 7.31, but displacement between image 1 and images 18-25.

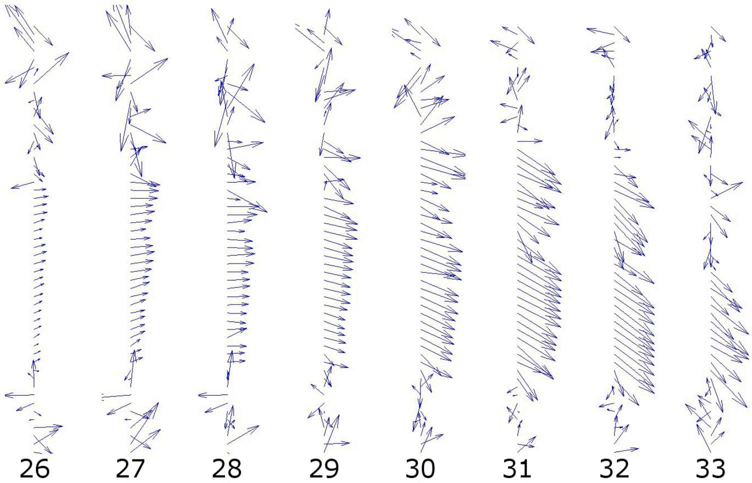

Figure 7.34: As Figure 7.31, but displacement between image 1 and images 26-33. One can see that the catastrophic failure has started, as the snow starts moving to the right and downwards as a cohesive block (parallel arrows in the middle of the displacement fields.)

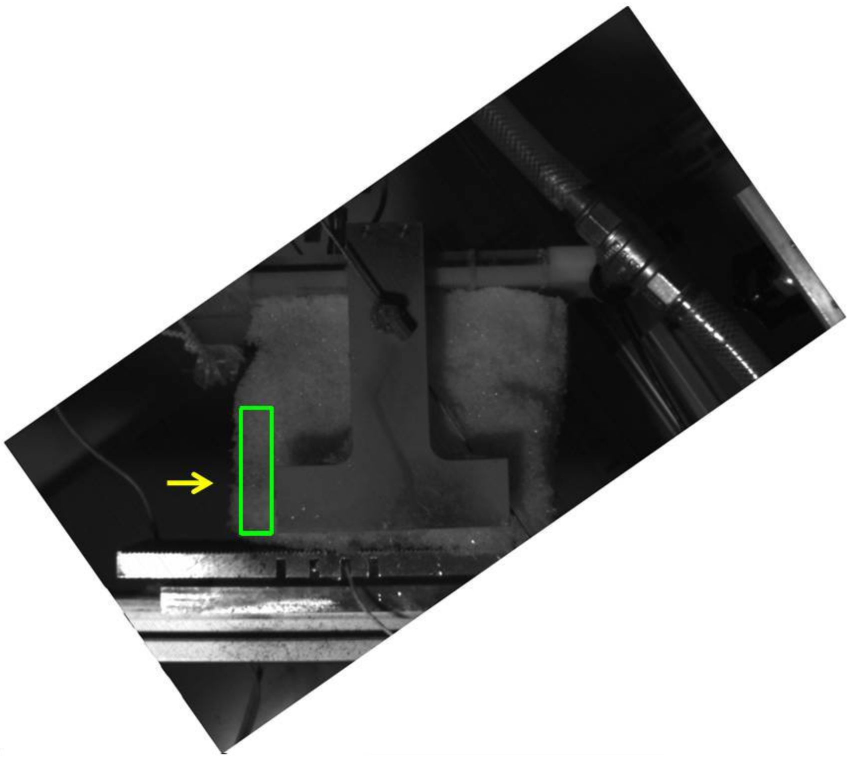

Figure 7.35: Section where the catastrophic failure initiated, sample B9. The place where the propagating fracture will start is marked with an arrow. The rectangle is 16 mm wide and 64 mm high.

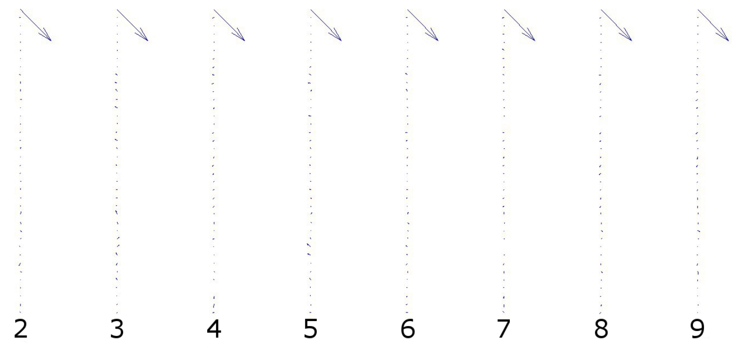

Figure 7.36: Initiation of the catastrophic failure at the bottom of the sample, sample B9. The PIV analysis is for the section shown in Figure 7.35 and shows the displacement between the first image and images 2-9. The displacement is averaged over the x-direction. The uppermost arrow in each sequence is only for reference, its coordinates are [0.8 mm, 0.8 mm].

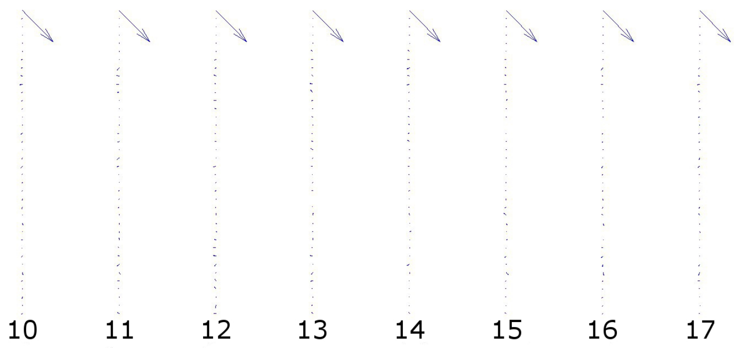

Figure 7.37: As Figure 7.36, but displacement between image 1 and images 10-17.

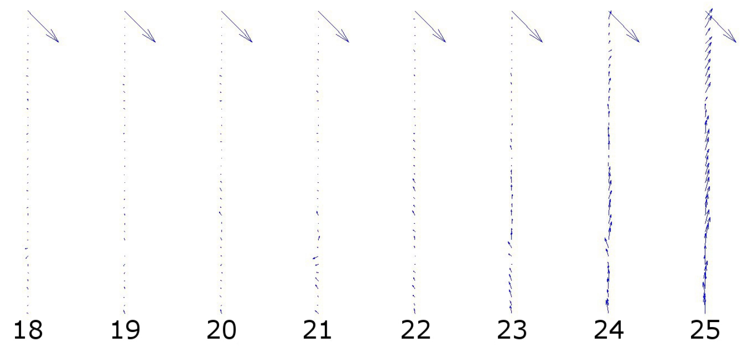

Figure 7.38: As Figure 7.36, but displacement between image 1 and images 18-25.

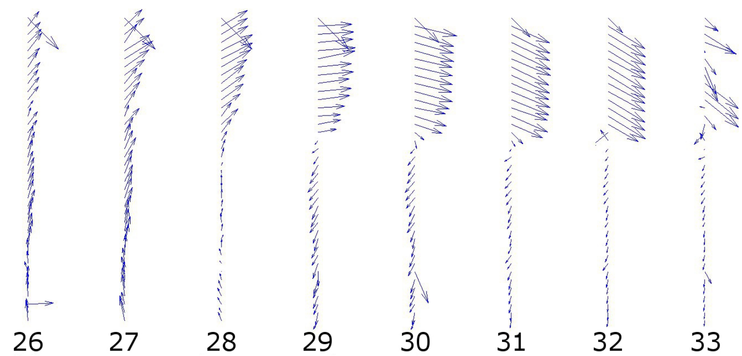

Figure 7.39: As Figure 7.36, but displacement between image 1 and images 26-33. We see the onset of the catastrophic fracture.

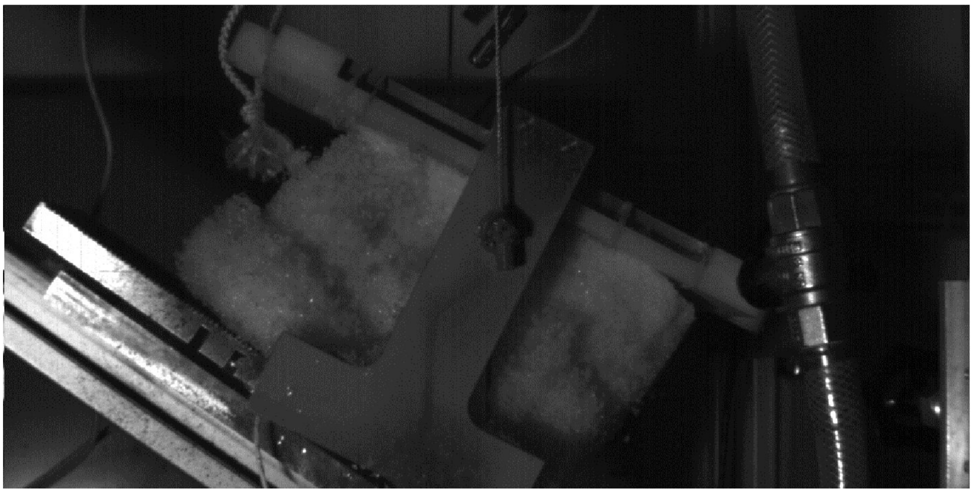

Figure 7.40: Sample B9 after the crack at the bottom has propagated. Final breakdown.

Figure 7.41: Sample B9, crushed and broken.

Figure 7.42: Sample B9, last image, the snow sample has fractured completely.

Chapter 8

Discussion of the experimental results

8.1 Tomography measurements

The surface hoar layer in samples of type A (see Table 6.1) can easily be noted on the μ-CT image; one can clearly see the large crystals and the large pore space in between. The rounded grains of the upper and lower layer are significantly smaller than the surface hoar crystals and the gaps between them.

The depth hoar layer of the sample of type B (see Table 6.1) is harder to detect on the μ-CT image. The layer above and the crust below are much thinner than the thick depth hoar layer. On a closer look one notices the huge pores also in this weak layer.

As can be seen in Figure 7.3 the large surface hoar crystals of the weak layer of sample type C were already covered by small facets. This is due to the fact that this surface hoar layer had been within the snowpack for approximately two weeks before it was harvested. Consequently, this surface hoar layer may be considered as relatively strong for a surface hoar layer.

On one hand this raises the question on whether this was a representative surface hoar layer for performing shear experiments. On the other hand only the layer's high strength made it possible to cut a sample small enough for the μ-CT sample holder without destroying the sample. (We managed at about the tenth try.) So using this layer for our experiments seemed justified, especially after performing several series of shear experiments with surface hoar, and seeing that layer A (Fig. 7.15) was roughly as strong as

layer C. Layer A was harvested only a couple of days after it has been covered by snowfall (when the upper layer was cohesive enough for harvesting). Considering the similar shear strengths of layers A ('fresh') and C ('old') support the assumption that surface hoar layers form persistent weak layers which may stay weak throughout the whole season (Jamieson and Schweizer, 2000).
The μ-CT image from the sample of kind TRA (see Fig. 7.4) is not only a very beautiful picture to look at, it also proves that the depth hoar we produced in our laboratory consists of the same cup-shaped crystals as natural depth hoar. This image is also a good example of the layered nature of the snowpack, which can be recognized here even by persons who know nothing about CT-images or snow.

Comparing the densities of the weak layers in Table 7.1 and the results of the displacement-controlled shear experiments in Section 7.2, one notices that the weak layers with lower densities also had a lower shear strength. Samples of type A and C were significantly weaker than samples of type B and TRN and also had a much lower density. This is what was expected as others had already noted this direct correlation between snow density and snow strength (see e.g. McClung and Schaerer, 2006).
It has to be noted, though, that the densities measured for samples A and C are unrealistically low. This is due to the fact that the very small samples that could be scanned with the μ-CT (sample area approximately 1.5 cm $\times$ 1.5 cm) mostly consisted of the main connected element of the small samples, and many protruding structures fell out of the sample during cutting. So the pores of the scanned surface hoar samples of types A and C are probably unrealistically large and the bulk density of a surface hoar layer is usually larger than the densities we measured.
Density of course is not the only material parameter associated with snow strength. Hardness, grain type, and grain size are of equal importance. All our weak layers were very soft, so no conclusions about the effect of the weak layer's hardness can be made. The hardness of the layers above and below the weak layer had no noticeable effect on the sample's strength. Increasing grain size has been shown to decrease snow strength by Schweizer et al. (2004), but since we only have a limited number of different grain sizes

within our experiments, we cannot make any statements here. We saw that surface hoar crystals were weaker than the rounded grains of the homogeneous samples, which is in agreement with the field experiments of Jamieson and Johnston (2001).

Originally we had planned to calculate microstructural parameters like bond-to-grain ratio or the coordination number of the grains within the weak layer. We had hoped to find a correlation between those microscopic parameters and the macroscopic strength measured during our shear experiments. While the grain detection algorithm developed by Theile and Schneebeli (2010) works well for rounded grains, it unfortunately cannot yet detect grains with a surface structure like surface hoar (samples A), especially faceted surface hoar (samples C), and depth hoar (samples B and TRA). The algorithm is based on curvature, and it associates changes in curvature with grain boundaries, which is problematic for crystals with surfaces of varying curvature.
We are sure that the further development of the algorithm will overcome the difficulties of working with irregular crystal shapes. Calculating microscopic parameters from our images and comparing them to the macroscopic properties should provide new insights into the microscopic relations of snow.

8.2 Displacement-controlled shear experiments

The stress-strain curves we found for layered samples were fairly similar to the stress-strain curves for homogeneous snow samples. This can be understood since we saw that the strain is concentrated in the weak layer, and the upper and lower layers only act as 'extended sample holders'.

Two differences were noted between the experiments with the homogeneous and the layered samples. First, the crack surface was very rough for homogeneous samples whereas it was smooth and within the weak layer for layered samples.
The second difference observed was that the shear strength in the case of brittle failure and the shear strength at ductile behaviour, differed less in the case of homogeneous

samples. For homogeneous samples the shear strength in the ductile case was larger than the shear strength in the brittle case by a factor of about 1.5-2. For layered samples, on the other hand, the shear strength in the ductile case was larger than the shear strength in the brittle case by a factor of 2.5-5. This means that the shear strength for brittle failure behaviour in the case of layered samples was significantly smaller than in the case of ductile failure behaviour. We assume that this is due to crack propagation even within our small laboratory samples. The defined plane of weakness given by the weak layer allowed a small perturbation or crack to propagate and favoured brittle fracture at already small stresses. For homogeneous samples, on the other hand, the sample had to break apart and the crack could not follow a defined plane of weakness. Since we assume ductile failure behaviour to result from small fractures and the simultaneous healing of other small fractures, the weakening effect of the defined failure plane seems to be of less importance there, at least for the dimensions of our laboratory samples.
Differences in behaviour can also be attributed to the different grain types, the homogeneous samples consisted of rounded grains, while the weak layers consisted of faceted grains and depth hoar crystals, respectively.

The stress-strain curves at low deformation rates of the surface hoar samples in Figure 7.7 overlap each other in the beginning, but sample TRA43 seems to fracture at the point of highest stress, while sample TRA38 shows strain softening before fracturing. Both phenomena were observed quite often. But the apparent fracture at the point of the highest stress was always associated with an error of the LFT (the drive stopped for some time, error messages popped up, the power had to be turned off and on again), so it has to be assumed that the sample did not fracture at this point but the drop in shear force was due to an error of the apparatus. The stresses we give are not the stresses at fracture but the peak stresses, since these could always be obtained whereas we often had the problem of the apparatus stopping during slow experiments.

There has been a debate on whether the first failure in a weak snow layer is in shear or in compression, whether the initial failure is a collapse of the weak layer. Very often, not always, did we observe a collapse of the weak layer, usually simultaneously with the drop in shear force, at least simultaneously within our measuring resolution, so it is difficult to answer the question on what is the trigger and what is the reaction. For sample TRA70 we definitely observed a shear fracture before the sample collapsed. As can be seen in Figure 7.8, the drop in shear force came clearly before the vertical displacement (collapse) of the weak layer, which means that in this case the shear fracture came clearly before the collapse of the weak layer. Sample TRA70 failed in shear, and it collapsed as a reaction to this failure.

The stress-strain curves obtained at slow loading rate of the surface hoar samples in Figure 7.7 are surprisingly similar to the simulation results of the FBM with large shape factor, (Fig. 4.4c), while the stress strain curves for snow samples consisting of rounded grains (Schweizer, 1998) and surface hoar crystals (Fig. 7.6) look more like the simulation results of the FBM with small shape factor, Figure 4.4a and b. This suggests that the strength distribution of the bonds between the rounded grains which Schweizer (1998) used and also of the bonds between surface hoar crystals (Fig. 7.6) have a smaller shape factor than the strength distribution of the bonds between crystals of a depth hoar layer.
We can therefore assume that rounded grains and surface hoar have an exponential strength distribution (Weibull distribution with $\beta = 1$) while depth hoar crystals have a Gaussian distribution. A small shape factor implies that there are many very weak bonds, but also quite a few strong ones. A large shape factor on the other hand means that the strength of the bonds does not vary too much. Two examples of Weibull distributions with equal scale factor ($\alpha = 3$) but different shape factors ($\beta = 0.1$, $\beta = 1$, and $\beta = 3.4$) are shown in Figure 8.1.

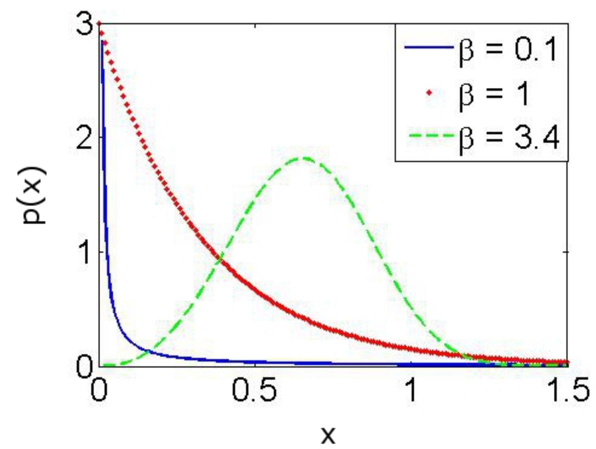

Figure 8.1: Density function of the Weibull distribution (Equation 3.1) with constant scale factor ($\alpha = 3$) and different shape factors β.

As Schweizer (1998) has reported for homogeneous snow samples, also for layered snow samples we found a clear strain rate dependence of the fracture stress and the failure behaviour. Considering the strain concentration within the weak layer, for both layered and homogeneous samples and our sample size we found the ductile-to-brittle transition (DBT) at about $3 \times 10^{-3}\mathrm{s}^{-1}$.

There might be a finite size effect since we dealt with fairly small samples. We varied the sample sizes (areas) from 5 cm $\times$ 5 cm up to 10 cm $\times$ 20 cm, and could not find a size effect within this range. Unfortunately, larger samples could not be tested with our apparatuses.

Low strain rates favor high fracture stress and ductile behaviour, while high strain rates induce brittle behaviour at a lower fracture stress. We observed the ductile-to-brittle transition (DBT) to take place at strain rates of $3 \cdot 10^{-3}$ s^{-1} at a normal stress of 1 kPa. Schweizer (1998) found the DBT at a strain rate of about 10^{-3} s^{-1} normal stress 0.5 kPa, while Fukuzawa and Narita (1993) found the DBT at approximately $2 \cdot 10^{-4}$ s^{-1} at no (or at least no mentioned) normal stress.These findings are consistent with the observation in rocks that increasing pressure enhances ductile behaviour (Robertson, 1955).

Another notable point from the results of the displacement-controlled experiments concerns sintering. Some samples were left in the apparatus to sinter after they had broken. Most samples collapsed as they fractured, and during this collapse the grains within the weak layer were crushed and the layer densified. The crushed and re-sintered weak layer had a higher shear strength than the original weak layer. We could observe this strengthening effect for all samples which were sheared twice, also for the ones which did not display a notable collapse the first time they were sheared. Our findings are in accordance with the experience of avalanche professionals and field measurements (Birkeland et al., 2006) which state that 'whumpfing' a slope without releasing an avalanche increases stability (maybe not directly after fracture, but hours afterwards). We expect this to be valid in general for thin weak layers. For thick depth hoar layers or a slope containing more than one weak layer, several whumpfs within one layer or slope have been reported, we expect an increase in stability only after the last possible whumpf.

8.3 Force-controlled experiments: layered versus homogeneous samples

For the force-controlled experiment with the homogeneous sample, we see that although the stress rate was constant, the strain rate increased (Fig. 7.18). This means the material progressively weakened during the loading process.

As we can see in Figure 7.21, for the homogeneous sample, the strain was uniform over the whole sample. For the layered sample, on the other hand, we see a clear concentration of strain (or deformation) within the weak layer (Fig. 7.21). This concentration of deformation (strain) in weak snowpack layers has often been assumed but has not been measured so far.

During the loading experiment with the homogeneous sample, the acoustic count rate (Fig. 7.17, lowest subfigure) increased shortly before fracture, this was also observed in other experiments performed with homogeneous samples (Ernst, 2009). Acoustic emissions are presumed to be a measure of the number of bonds breaking between the snow grains during deformation. The non-linear increase in strain (Fig. 7.18) indicates that the material progressively weakened during deformation, and the AE may be an indicator of this weakening process.

Also for the layered sample we measured an increase in acoustic counts shortly before and, of course, at fracture (Fig. 7.19, lowest subfigure). The count rate was smaller than in the case of the homogeneous sample, which can be easily understood if one considers that we were dealing with a weak layer, which had less bonds to break than a strong homogeneous sample.

The repeated occurrence of acoustic counts shortly before fracture supports the hypothesis that acoustic emission signals may act as precursors to global failure within snow samples and may therefore also be useful as precursors to avalanche release.

8.4 Force-controlled experiments with surface hoar

Due to the fragile nature of the weak layer tested, we obtained only a limited number of results. However, due to the fragility these results are very relevant and in addition they are consistent and seem plausible. As the sample size is small, catastrophic failure occurs relatively soon. Obviously, in a natural snowpack this would not be the case, but our results on the loading rate dependence, the strain concentration and the strength anisotropy are expected to be independent of sample size. Our laboratory experiments are related to failure initiation, whereas the field tests developed by Gauthier and Jamieson (2006) and Sigrist and Schweizer (2007) are appropriate to study crack propagation and crack-face friction during the initial stage of dry-snow slab avalanche release (van Herwijnen and Heierli, 2009).

The decrease of strength with loading rate is in agreement with previous measurements with displacement-controlled experiments (e.g. Schweizer, 1998) and statistical evidence on the effect of precipitation intensity on avalanche hazard probability (Perla, 1970). The strong concentration of shear deformation in the weak layer by a factor of 10 (depending on the thickness of the weak layer) indicates that the shear strain rate in the weak layer must have been similarly larger than the average global strain rate. Accordingly, the strain rates in the weak layer were about one order of magnitude larger and hence in good agreement with the critical strain rate of about $1 \times 10^{-3}\ \mathrm{s}^{-1}$ for the ductile-to-brittle transition reported for homogeneous snow samples (Schweizer, 1998). The lower critical strain rate ($1 \times 10^{-4}\ \mathrm{s}^{-1}$) reported by Fukuzawa and Narita (1993) might as well be due to the fact that they used artificially produced layered samples and reported global strain rate.

The large strain concentration suggests that strain rates in thin weak layers may be large enough so that damage occurs which may accumulate so that the layer eventually might fail - even at globally slow shear strain rates in the sloping snowpack (well below the ductile-to-brittle transition).

The dependence of strength on slope angle shows that layers of buried surface hoar are weaker in shear than in compression (Fig. 7.25) - this already became obvious (purely qualitatively) during sample preparation when typically disturbances in shear caused many samples to fail. This result has often been proposed (e.g. McClung and Schaerer, 2006), but to our knowledge so far has never been shown. For depth hoar layers the anisotropic failure behavior has already been postulated by Akitaya (1974). The dependence of strength on loading direction is probably related to the strong anisotropy of the microstructure in layers of buried surface hoar. Jamieson and Schweizer (2000) observed that those layers were relatively stiff in compression, but susceptible to shear. This finding is of particular relevance for the initiation of naturally (spontaneously) releasing dry-snow slab avalanches. Obviously, the weak layers are loaded by the weight of the overlaying layers, so under mixed compressive and shear load - with the compressive load always dominating below 45 °. Nevertheless, initiation by damage accumulation leading to failure due to shear deformation seems more probable than due to compressive deformation. As we observed brittle failure in 8 out of 10 tests, this strain rate value agrees with the critical strain rate typically reported for the ductile-to-brittle transition for homogeneous snow samples. This implies that the strain rate due to creep in a weak layer in a natural snowpack may be high enough for failure even if the global strain rate is low.

The fracture stress decreased with increasing slope angle. This demonstrates that layers of buried surface hoar are weaker in shear than in compression. Probably the largely anisotropic, truss-like structure of these mono-crystalline layers is responsible for the dependence of strength on loading direction.

We could not find a concentration of compressive deformation in the surface hoar layers studied. This may be due to the fact that we are dealing with a monocrystalline layer which cannot easily be compressed by rearranging grains unless the whole layer collapses. On the other hand, as can be seen in Fig. 7.22, our compressive strains were often very small, maybe too small for finding any significant trends with PIV analysis.

8.5 Force-controlled experiments with depth hoar

Natural depth hoar samples are especially difficult to harvest, since, in contrast to layers of buried surface hoar, they are usually at the bottom of the snowpack and hardly ever have a cohesive layer beneath them. In the case of samples of kind B, we were lucky to have a crust below the depth hoar layer, which made it possible to cut and transport samples. The height of the samples had to be chosen quite large for the reason of keeping the crust at the bottom. We are aware that this gives an unfavourable area to height ratio for the whole sample. Studying the deformation during the experiment, though, we see a concentration of deformation at the interface between the faceted layer and the crust below. This is also the location where the samples fractured. Considering this very thin weak interface, the area to height ratio seems acceptable.

Interestingly, although the samples of kind B were stronger at high slope angles and loading rates than the samples from layer A, they always fractured, even at the slope angle of 25° and a loading rate of 2 N m^{-2} s^{-1} (normalized load), where samples from layer A did not fracture. This might be due to the large thickness of the samples, so any perturbative displacement of the upper sample holder might lead to an uniform stress field and to fracture of the samples.

The movies from samples B8, B9, B10, and B17 are unique in showing the actual formation of the initial catastrophic failure [1]. All four movies suggest that the catastrophic failure was a shear failure in the interface of the depth hoar layer and the crust below the layer. The catastrophic failure was triggered by some disturbance somewhere within the weak layer, maybe at a point where the weak layer had a particularly weak spot due to the inherent small-scale inhomogeneity of snow layers.

[1] 'Initial' because we consider the initial failure which may lead to the release of an avalanche, and 'catastrophic' from the laboratory sample's point of view.

Chapter 9

Conclusions

9.1 Modelling snow failure with a fibre bundle model

We used a simple fibre bundle model to simulate the deformation and failure of a weak snow layer under shear loading. For the case of no sintering the model can be solved analytically and our simulation results agreed with the analytic solution (Fig. 4.1). By incorporating sintering (i.e. re-bonding of fibres after fracture) into the model, we showed that the rate dependence of snow strength and the rate dependent mechanical behaviour can be reproduced by introducing a sintering probability and two different characteristic times for sintering and for breaking of fibres (Fig. 4.4). Thus the competing effects of bond breaking and sintering of bonds (after rearranging) between snow grains might be sufficient to explain the strain rate dependent bulk behaviour of snow. This had so far only been hypothesized (Schweizer, 1999). Our results also suggest that incorporating sintering is crucial for realistically modelling the mechanical behaviour of snow, at least for time scales of the order of seconds or larger. Despite the simplicity of the model, we found good qualitative agreement of the model output with the experimental data of displacement-controlled shearing of snow samples at different strain rates (Schweizer, 1998).

9.2 Tomography imaging

The μ-CT gives beautiful and interesting images, and we could also calculate weak layer density and specific surface area (SSA) from those images. As could be expected, lower weak layer density resulted in lower strength of the weak layer. Within our limited number of samples, no correlation between strength and SSA could be found. This is not surprising, since snow may contain many protruding structures, which increase the SSA, but do not contribute to snow strength.

Theile and Schneebeli (2010) developed an algorithm for analyzing the μ-CT images and calculating parameters like bond-to-grain ratio or the number of neighbouring grains. The algorithm works well for rounded grains but not for faceted grains or surface hoar since it uses curvature to distinguish between different grains. A further development of the algorithm might shed more light on the microscopic properties of our snow samples and their relation to macroscopic snow strength and failure behaviour.

9.3 Displacement-controlled shear experiments

Our displacement-controlled shear experiments showed that layered samples show fairly similar qualitative behaviour as the homogeneous samples. Two striking differences were noted, though. First, the fracture surface was always smooth and within the weak layer for the layered samples, while the fracture surface was rough and the crack often left its initial plane of fracture within the homogeneous samples. We can therefore conclude that a defined plane of weakness is needed for a shear fracture in snow (this is common also in other materials). The second notable difference between homogeneous and layered samples was that the difference in strength between brittle and ductile behaviour was larger in the case of the layered samples. We assume that this is due to the weak layer, which allows a small crack to propagate, even within our small laboratory samples, making the brittle shear strength of the layered samples very low. For ductile behaviour, sintering becomes increasingly important, probably overriding the effect of crack propagation.

We saw that almost all (90%) of the deformation was concentrated within the weak layer.

This has often been assumed, but never been measured so far.
For layered snow samples we found the ductile-to-brittle transition to take place at a strain rate of roughly $3 - 5 \times 10^{-3}\mathrm{s}^{-1}$ which is in fair agreement to (Schweizer, 1998), who found the DBT at a strain rate of about $1 \times 10^{-3}\mathrm{s}^{-1}$.

9.4 Development of a force-controlled loading apparatus for snow

We have developed a loading apparatus with a measuring system to study the processes that lead to catastrophic fracture of layered snow samples with respect to dry-snow slab avalanche release. In our loading apparatus, the snow sample is loaded under nature-like conditions, i.e. it is tilted by a 'slope angle' and is thereby loaded in shear and compression simultaneously. The advantage of this setup is clearly its resemblance to the processes occurring in nature, and therefore the relevance of the measurements performed for the release of slab avalanches. Until now, a simultaneous loading in shear and compression under controlled laboratory conditions had not been possible. A possible disadvantage of our setup might be, that its uniqueness makes exact comparison to other (laboratory) experiments with snow or to standard experiments with other materials difficult. Yet the order of magnitude of e.g. the fracture stress we measure for the homogeneous samples is the same as we and Schweizer (1998) found in the displacement-controlled shear experiments with homogeneous snow.

9.5 Force-controlled experiments with snow samples containing a weak layer

We have performed a series of strength tests with a bidirectional force-controlled test apparatus with layered samples containing natural layers of buried surface hoar and depth hoar. These kinds of layers are known to be weak and frequently form the failure layers of dry-snow slab avalanches. For the first time, the failure behavior of a natural, particularly fragile weak layer was characterized. However, due to the fragile nature of the layers only 27 samples from the originally 49 could be tested.

Our results from the measurements with the surface hoar layer clearly confirm that strength decreases with loading rate. With PIV we analyzed the deformation field and found that the shear strain was concentrated in the weak layer and was in most cases about 10 times larger than the global strain. The strain concentration factor depends on the thickness of the weak layer in relation to the sample thickness. In a natural snowpack the concentration factor might well reach a value of 100. Considering the concentration of shear strain within the weak layer, the strain rate within the weak layer was about 1×10^{-3} s^{-1}.

By varying the 'slope angle' the amount of mixed mode loading (compression vs. shear) varied. The observed failure behavior suggests that the initial failure leading to natural dry-snow slab avalanche release is rather caused by the shear component of deformation than by the compressive component - at least if the failure layer consists of surface hoar. For avalanche release this means that steep terrain favours the initiation of a crack prone for propagation, provided that snowpack conditions are similar.

We found that the snow strength decreases with loading rate. In practice this implies that a skier may trigger an avalanche due to fast loading, even if the weight of the skier is comparable or lower than the weight of snow above the weak layer (which accumulated slowly).

Within the experiments with the depth hoar samples we could actually follow how the initial failure started. It seemed to start as a local failure at a seemingly arbitrary position within the weak layer which induced a shear crack at the weak interface between the depth hoar layer and the crust below. So the inherent disordered nature of snow seems to be important for failure initiation, and a weak layer or interface is needed where a macroscopic crack which can grow large enough for crack propagation can form. In our displacement-controlled experiments we saw that cracks heal again after only a short time, so if they cannot propagate, they will disappear again and not remain as 'hot spots' within the snowpack. On the contrary, a crack which has resintered seems to be stronger than the original zone where the crack developed.

9.6 Comparison of displacement- and force-controlled experiments

The displacement-controlled experiments allowed us to study the material behaviour of layered snow samples, especially the ductile-to-brittle transition. We could show that it has the same order of magnitude as for homogeneous snow samples. We could also study the fracture surface and saw a nice shear crack for layered samples and an uneven crack for homogeneous samples. Also the effect of sintering could be observed, we clearly saw a strengthening of fractured and re-sintered weak layers.

Direct simple shear experiments such as the ones we performed with the linear friction tester are widely performed with other materials, this enables comparison of our data to data from other materials (such as clay, rock, wet sand, metal, industrial foam, etc.).

The force-controlled apparatus was designed to mimic field conditions in the laboratory. So the experiments with this apparatus allowed us to study the effect of slope angle and loading rate, two important factors within avalanche initiation. It was not possible to study sintering within the force-controlled apparatus, since the pieces of a fractured sample were separated immediately due to the geometric setup. We feel that our force-controlled experiments give exciting insights into avalanche formation, but we are aware of the fact that it is not easily possible to compare those experiments to standard fracture mechanical experiments.

In an ideal new series of experiments, all kinds of snow samples would be tested with both kinds of apparatuses.

9.7 Comparison of experimental data with modelled results, implication for the strength distribution of bonds between snow grains

As we have seen in Chapter 8.2, the form of the stress-strain curves for the slow displacement-controlled experiments with homogeneous samples and surface hoar samples resembles the modelled stress-strain curves if one assumes a fibre strength distribution (Weibull distribution) with a small shape factor. The stress-strain curves of the depth hoar samples, on the other hand, exhibit the distinct kink which was also found within our simulation results with probability distributions with a large shape factor, $\beta \gtrsim 2$. We assume the bonds[1] between grains break during snow deformation. This comparison suggests that the bonds in snow consisting of rounded grains or surface hoar have an exponential strength distribution while the bonds in snow consisting of depth hoar and faceted crystals have a Gaussian distribution. According to these distributions there should be many weak bonds in rounded grained snow and surface hoar, while the variation of bond strengths should be relatively small in snow consisting of faceted crystals.

[1] We can also define 'bond' as the part of the snow matrix which breaks during deformation.

Chapter 10

Outlook

Modelling snow and especially snow containing a weak layer for mechanical purposes with a fibre bundle model (FBM) turned out to be a good approach. With more input from experiments, the model could be improved, though. It would be particularly interesting to compare acoustic emission patterns obtained from experiments during snow deformation to fibre breaking patterns from the FBM. A related approach has been used by Cruz Hidalgo et al. (2002) who measured acoustic emissions during compression experiments with granular media and compared the distribution of the signal amplitude to their modelled result.

A more sophisticated modelling approach might also include dropping the assumption of stiff plates and introducing load sharing into the model. We then could study the influence of slab stiffness on the weak layer. Furthermore, metamorphism could be included into the model so that the strength distribution explicitly would change over time.

A future statistically based microstructural failure model might be coupled with a fracture mechanical model to simulate failure initiation as well as crack propagation in the snow slab avalanche release process.

Our acoustic emission measurements remained at a very preliminary state. Parameters like the acoustic impedance of snow and the sample holders, the coupling between the snow and the sensors and the acoustic velocity of snow still have to be determined. The question whether these quantities are isotropic within snow and how the snow layering effects them remain to be answered. We still do not know exactly whether sound within snow travels mostly within the ice matrix, within the air, or both (Marco et al., 1998), there is a density and probably also a microstructure and frequency dependence. Acoustics in wet snow have not been studied yet. Also a frequency analysis of the acoustic emissions measured within snow remains to be done.

In the future, it would be relevant to perform more acoustic emission measurements during deformation and loading experiments with snow samples, both homogeneous and layered. Clear acoustic precursors (in time or frequency domain) remain to be found. And finally, using an array of acoustic sensors for measuring the acoustic emissions might allow localizing the origin of the acoustic emissions (the bond breaking) within the snow sample.

Adapting the acoustic measurement system for field experiments would probably require using microphones, since the damping of ultrasonic sound in snow is very high. A preceding thorough experimental acoustic study in the laboratory for finding the optimal frequency range (and maybe even precursors) might be useful.

μ-CT images were taken of samples of kind A, B, C, and TRA. One could skeletonize these images and use the skeletons as structural input for a finite element program. A periodic assembly of the images would lead to realistic sample sizes for mechanical simulations. One could then perform finite element calculations (e.g. deform the samples in compression or shear, or load them with different loading rates), compare the outcome with the experimental results, and also identify which parts of the ice matrix are the first to break and maybe even detect crack propagation.

Another option would be to use a further developed detection algorithm of Theile and Schneebeli (2010). With such an algorithm, one might be able to relate the acoustic emissions to the exact bonds which are breaking. The comparison between the micro-mechanical properties obtained from these images and the macro-mechanical properties from the shear- and loading experiments including the acoustic emissions might also lead to a better understanding of the relationship between microstructure and macroscopic properties of snow.

For better relating our experimental results to actual failure of potential avalanche slopes, loading experiments with bigger samples would be relevant. Our loading apparatus could be modified for bigger sample sizes. Parallel to the laboratory experiments also field experiments could be performed (e.g. one field experiment with a very large sample and several laboratory experiments with smaller samples harvested at the site of the field experiment).

Wet-snow slab avalanches have not been regarded within this thesis. We assume that our loading apparatus might also be useful for studying this topic. One could heat or wet a snow sample within the apparatus and measure the amount of heat/water and an eventual additional load which is needed for wet-snow failure.

Appendix A

List of symbols and abbrevations

Symbols fibre bundle model		
Symbol	**Description**	**Unit**
A	area	m^2
F	force	N
f	force acting on a single fibre	N
l_0	initial fibre length	m
N	number of fibres	–
p_s	sintering probability	–
p_{max}	maximum sintering probability	–
t_s	time it takes for a fibre to sinter	s
α	scale factor of the Weibull distr.	–
β	shape factor of the Weibull distr.	–
Δl	elongation of a fibre	m
Δx	horizontal displ. of upper plate	m
ϵ	strain	–
ρ	density	kg/m^3
σ	stress	Pa
σ_c	strength	Pa

Symbols experiments		
Symbol	**Description**	**Unit**
F	force	N

h	height	m
N	number of experiments	–
T	temperature	°C
t	time	s
α	slope angle	°
Δx	shear displacement	m
Δz	normal displacement	m
ϵ	strain	–
$\dot{\epsilon}$	strain rate	–
ρ	density	kg m^{-3}
σ	stress	Pa
σ_{c}	critical stress/stress at fracture	Pa
$\tilde{\sigma}$	normalized load	N m^{-2}
	(load divided by sample area)	
$\tilde{\sigma}_c$	normalized load at fracture	N m^{-2}
$\dot{\tilde{\sigma}}_c$	rate of normalized load	N m$^{-2}s^{-1}$

Abbreviations for grain types

Abbreviation	**Description**
CR	crust
DH	depth hoar
FC	faceted crystals
RG	rounded grains
SH	surface hoar

Other abbreviations

Abbreviation	**Description**
AE	acoustic emissions
CN	coordination number
DBT	ductile-to-brittle transition
FBM	fibre bundle model
FCH	fracture character
IDL	interactive data language
LFT	linear friction tester

PBC	periodic boundary conditions
PIV	particle image velocimetry
SMP	snow micro-penetrometer
SSA	specific surface area
μ-CT	micro computer tomograph

List of Figures

List of Tables

Appendix B

Results of experiments with the linear friction tester

Below we show a table with additional results of successfully performed displacement-controlled experiments. We include them in this thesis mainly because they might be of interest to a successional PhD student performing mechanical experiments with weak snow layers. The most important results from the displacement-controlled shear experiments were presented in detail already in section 7.2.

The sample types are ORN (natural surface hoar), ORA (artificial surface hoar), TRN (natural depth hoar or faceted weak layer), TRA (artificial depth hoar or faceted weak layer), and HOM (homogeneous sample, either natural or artificial). The samples described in more detail in section 6.1 were of type ORN (sample labelled A and C), TRN (samples labelled B). The experiments shown in section 7.2 which were labelled TRA or HOM plus a number correspond to the experiments in this table. Within the table, they are labelled with the number only. Experiments with samples A, B, and C see Table 7.2 are not shown in this appendix. Snow type is described as grain type according to Fierz et al. (2009), average grain size, and hand hardness index (1: Fist, 2: Four fingers). For the layered samples, which consisted of three layers, the snow is characterized layer by layer, beginning with the top layer. The fracture character (FCH) can either be ductile or brittle. $\dot{\epsilon}_{\mathrm{g}}$ denotes the global strain rate, $\tilde{\sigma}_{\mathrm{c}}$ the normalized peak load, and ϵ_{c} the shear strain at fracture.

The remarks were copied from the laboratory book and are not always exhaustive [1].

[1]If, for example, 'collapse' is remarked, this means that this particular sample showed a significant collapse. If, on the other hand, there is no remark for an experiment, this does NOT mean that the sample concerned did not collapse. We include this remark anyway, since for some reason it might be of interest in the future to have data from experiments which showed a collapse for sure.

Name	Type	Snow type	FCH	$\dot{\epsilon}_\mathrm{g}$ (s^{-1})	$\tilde{\sigma}_\mathrm{c}$ ($\mathrm{kN\ m}^{-2}$)	ϵ_c	remarks
1	ORN	RG, 0.5-1, 3-4; SH, 15, 1; RG, 0.5-1,1-2	brittle	e-3	3.4 e3	0.005	collapse
2	ORN	RG, 0.5, 3-4; SH, 15, 1; FC, 1-1.5,1-2	brittle	1.20E-03	1.20E+03	0.0039	collapse
3	ORN	RG, 0.5-1, 3-4; SH, 15, 1; RG, 0.5-1,1-2	brittle	1.40E-03	2.90E+03	0.004	collapse, broken and resintered sample
4	ORN	RG, 0.5-1, 3-4; SH, 15, 1; RG, 0.5-1,1-2	brittle	1.30E-03	4.50E+02	0.0026	collapse
5	ORN	RG, 0.5-1, 3-4; SH, 15, 1; RG, 0.5-1,1-2	brittle	1.10E-03	5.80E+02	0.0036	collapse
6	ORN	RG, 0.5-1, 3-4; SH, 15, 1; RG, 0.5-1,1-2	ductile	1.50E-04	2.90E+03	0.27	softening
7	ORN	RG, 0.5-1, 3-4; SH, 15, 1; RG, 0.5-1,1-2	ductile	1.30E-04	2.40E+03	0.21	softening
8	ORN	RG, 0.5-1, 3-4; SH, 15, 1; RG, 0.5-1,1-2	ductile	2.20E-04	2.50E+03	0.47	softening; broken and resintered sample
9	ORN	RG, 0.5-1, 3-4; SH, 15, 1; RG, 0.5-1,1-2	brittle	6.10E-04	1.30E+03	0.0032	
10	ORN	RG, 0.5-1, 3-4; SH, 15, 1; RG, 0.5-1,1-2	brittle	7.10E-04	9.70E+02	0.0064	also tensile fracture in middle of sample
11	ORN	RG, 0.5-1, 3-4; SH, 15, 1; RG, 0.5-1,1-2	ductile	1.50E-04	2.10E+03	0.21	also tensile fracture in middle of sample
12	ORN	RG, 0.5, 3-4; SH, 15, 1; FC, 1-1.5,1-2	ductile	1.20E-04	5.40E+03	0.18	hardening; collapse
13	ORN	RG, 0.5, 3-4; SH, 15, 1; FC, 1-1.5,1-2	ductile	1.60E-04	7.50E+03	0.17	hardening
14	ORN	RG, 0.5, 3-4; SH, 15, 1; FC, 1-1.5,1-2	ductile	1.80E-04	7.10E+03	0.15	hardening
15	ORN	RG, 0.25-0.5, 3; SH, 0.5-1, 1; FC, 1.25-1, 1	ductile	2.20E-03	1.70E+04	3.40E-03	broken and resintered sample
16	ORN	RG, 0.25-0.5, 3; SH, 0.5-1, 1; FC, 1.25-1, 1	brittle	2.00E-03	2.10E+03	0.001	collapse
17	ORN	RG, 0.25-0.5, 3; SH, 0.5-1, 1; FC, 1.25-1, 1	?!	2.00E-03	2.10E+03	8.30E-03	collapse
18	ORN	RG, 0.25-0.5, 3; SH, 0.5-1, 1; FC, 1.25-1, 1	ductile	2.40E-04	8.00E+03	0.38	softening; broken and resintered sample
19	ORN	RG, 0.5, 3-4; SH, 15, 1; FC, 1-1.5,1-2	brittle	1.90E-03	2.50E+03	2.30E-03	collapse
20	ORN	RG, 0.5, 3-4; SH, 15, 1; FC, 1-1.5,1-2	ductile	1.80E-04	8.40E+03	0.18	hardening
21	ORA	sample christoph 24	brittle	1.50E-02	3.80E+03	7.90E-04	
22	ORA	RG, 0.25-5, 2; SH, 1-40, 1; FC, 1-1.5, 3	ductile	1.70E-04	3.50E+03	0.18	softening
23	ORA	RG, 0.25-5, 2; SH, 1-40, 1; FC, 1-1.5, 3	ductile	1.80E-04	3.60E+03	1.50E-01	softening
24	ORA	RG, 0.5-1, 3; SH, 15, 1; RG, 0.5-1, 2	brittle	1.50E-02	3.50E+02	0.0074	shear force smaller than friction after fracture
25	ORA	RG, 0.5-1, 3; SH, 15, 1; RG, 0.5-1, 2	?!	2.20E-04	1.90E+04	3.40E-03	
26	ORA	sample christoph 34	ductile	3.40E-04	7.60E+03	0.19	hardening
27	TRA	RG, 0.5, 3-4; FC, 0.5-0.75, 1; RG, 0.25-0.5,3-4	?!	3.30E-04	3.70E+03	2.20E-01	softening
28	TRA	RG, 0.5, 3-4; FC, 0.5-0.75, 1; RG, 0.25-0.5,3-5	ductile	3.00E-04	2.70E+03	0.08	softening
29	TRA	RG, 0.5, 3-4; FC, 0.5-0.75, 1; RG, 0.25-0.5,3-6	ductile	2.30E-04	2.40E+03	2.20E-02	softening
30	TRA	FC, 0.5, 3; FC, 1, 2; FC, 1, 3	brittle	1.40E-03	7.00E+02	4.00E-03	collapse
31	HOM	FC, 1, 3-4	brittle	2.10E-03	3.30E+03	2.20E-03	uneven fracture in middle of sample

32	TRA	FC, 1, 3-4; FC, 1, 1; FC, 1, 3-4	brittle	1.60E-03	1.10E+03	1.30E-03	
33	HOM	FC, 1, 3	ductile	1.70E-04			uneven fracture in middle of sample
34	HOM	FC, 1, 3	brittle	1.70E-03			fracture partly in snow, partly between snow and sample holder
35	HOM	FC, 1, 3	brittle	3.00E-03	6.40E+03	3.00E-03	fracture partly in snow, partly between snow and sample holder
36	HOM	FC, 1, 3	brittle	2.10E-02	6.70E+03	8.50E-04	uneven fracture in middle of sample
37	HOM	FC, 1, 3	brittle	2.10E-03	6.20E+03	1.50E-03	uneven fracture in middle of sample
38	TRA	RG, 0.75, 4; DH, 2, 3; RG, 0.75, 4	ductile	2.50E-04	7.20E+03	2.00E-01	
39	TRA	FC, 1.5, 3-4; FC, 2, 1; FC, 1.5, 3-4		1.70E-04	1.20E+04	3.30E-02	sintered sample
41	TRA	FC, 1.5, 3-4; FC, 2, 1; FC, 1.5, 3-4	brittle	8.00E-04	1.80E+04	4.80E-03	
42	TRA	RG, 0.25, 4; FC, 1.5, 1; RG, 0.25, 4	brittle	1.00E-03	1.60E+04	3.50E+03	
43	TRA	RG, 0.75, 4; DH, 2, 3; RG, 0.75, 4	ductile	2.00E-04	7.60E+03	2.00E-01	
44	TRA	RG, 0.75, 4; FH, 2, 3; RG, 0.75, 4	brittle	2.00E-04	2.30E+04	2.80E-03	
46	HOM	RG, 0.75, 3-4		3.10E-04			
47	HOM	RG, 0.75, 3-4		3.10E-04	6.10E+03	5.80E-02	
49	HOM	RG, 0.75, 3-4		3.10E-03			fracture between sample holder and sample
50	HOM	RG, 0.75, 3-4		3.10E-03	3.90E+03	3.70E-03	
52	TRA	FC, 1, 3; DH, 1.5, 3; FC, 1, 3	brittle	1.80E-03	6.40E+03	3.10E-03	relatively uneven fracture surface
53	TRA	FC, 1, 3; DH, 1.5, 3; FC, 1, 3	ductile	1.80E-04	7.90E+03	3.50E-02	hardening
53a	TRA	FC, 1, 3; DH, 1.5, 3; FC, 1, 3	brittle	1.80E-03	7.45E+03	2.50E-03	broken and resinterd sample
54	TRA	FC, 1, 3; DH, 1.5, 3; FC, 1, 3		9.10E-04	3.00E+03	1.10E-02	
55	TRA	FC, 1, 3; DH, 1.5, 3; FC, 1, 3		1.80E-04	8.90E+03	4.90E-02	hardening
55a	TRA	FC, 1, 3; DH, 1.5, 3; FC, 1, 3		9.10E-04	1.00E+04	6.40E-03	broken and resinterd sample
56	HOM	RG, 0.25, 2-3	brittle	4.50E-03	3.10E+03	6.80E-03	
57	HOM	RG, 0.25, 2-3	brittle	1.90E-03	3.10E+03	5.80E-03	
58	HOM	RG, 0.25, 2-3	brittle	3.80E-03	3.20E+03	7.70E-03	
59	TRA	FC, 1, 2; DH, 1.5, 1; FC, 1, 2		1.60E-03			breaks in upper layer, upper layer too soft
60	HOM	RG, 0.25, 2-3	brittle	4.70E-03			
70	TRA	RG, 0.75, 4; DH, 2, 3; RG, 0.75, 4	brittle	0.0015	2E+03	2.80E-03	
71	TRA	RG, 0.75, 4; DH, 2, 3; RG, 0.75, 4	brittle	0.0014	2.4E+03	3.50E-03	
74	ORN	RG, 0.25, 4; SH, 1, 1; FC, 1, 4		1.3E-04	4.0E+03	1.9E-03	collapse

Bibliography

Akitaya, E., 1974. Studies on depth hoar. Contributions from the Institute of Low Temperature Science, Series A 26, 1–67.

Alava, M., Nukala, P., Zapperi, S., 2006. Statistical models of fracture. Advances in Physics 55 (3-4), 349–476.

Ammann, W., Buser, O., Vollenwyder, U., 1997. Lawinen. Birkhäuser Verlag, Basel, Switzerland.

Anderson, T. L., 1995. Fracture Mechanics. CRC Press, 2000 Corporate Blvd., N.W., Boca Raton, Florida 33431.

Bader, H., Haefeli, R., Bucher, E., Neher, J. Eckel, O., Thams, C., Niggli, P., 1939. Der Schnee und seine Metamorphose. Kümmerly & Frey, Zürich.

Bader, H., Salm, B., 1990. On the mechanics of snow slab release. Cold Regions Science and Technology 17, 287–300.

Bartelt, P., von Moos, M., 2000. Triaxial tests to determine a microstructure-based snow viscosity law. Annals of Glaciology 31, 457–462.

Bažant, Z., Zi, G., McClung, D., 2003. Size effect law and fracture mechanics of the triggering of dry snow slab avalanches. Journal of Geophysical Research 108 (B2), doi:10.1029/2002JB001884.

Birkeland, K., Kronholm, K., Logan, S., Schweizer, J., 2006. Field measurements after fracture of snowpack weak layers. Geophysical Research Letters 33, doi:10.1029/2005GL025104.

Borstad, C., McClung, D., 2008. Slab fracture at 1900 frames per second - experimental methods. In: Campbell, C., Conger, S., Haegeli, P. (Eds.), Proceedings ISSW 2008. International Snow Science Workshop. Whistler, BC, Canada, 21-27 September 2008, pp. 22–24.

Camponovo, C., Schweizer, J., 2001. Rheological measurements of the viscoelastic properties of snow. Annals of Glaciology 32, 44–50.

Chakrabarti, B., Benguigui, L., 1997. Statistical physics of fracture and breakdown in disordered systems. Oxford University Press, Oxford, U.K.

Cole, D., Dempsey, J., 2004. In situ sea ice experiments in McMurdo Sound: cyclic loading, fracture, and acoustic emissions. Journal of Cold Regions Engineering 18, 155–174.

Cruz Hidalgo, R., Grosse, C. U., Kun, F., Reinhardt, H. W., Herrmann, H. J., 2002. Evolution of percolating force chains in compressed granular media. Physical Review Letters 89 (20), 205501.

Daniels, H., 1945. The statistical theory of the strength of bundles of threads. Proceedings of the Royal Society of London A183, 405.

de Montmollin, V., 1982. Shear tests on snow explained by fast metamorphism. Journal of Glaciology 28 (98), 187–198.

Delaplace, A., Pijaudier-Cabot, G., Roux, S., 1996. Progressive damage in discrete models and consequences on continuum modelling. Journal of the Mechanics and Physics of Solids 44 (1), 99–136.

Duxbury, P., 1990. Breakdown of diluted and hirarchical systems. In: Herrmann, H., Roux, S. (Eds.), Statistical models for the fracture of disordered media. Elsevier (North-Holland), Amsterdam, pp. 189–228.

Ernst, R., 2009. Akustische Emissionen von Schnee bei kraftgesteuerten Scherversuchen. M.S. thesis, ETH Zürich, Switzerland.

Fierz, C., Armstrong, R., Durand, Y., Etchevers, P., Greene, E., McClung, D., Nishimura, K., Satyawali, P., Sokratov, S., 2009. The International Classification for Seasonal Snow on the Ground. Paris, UNESCO-International Hydrological Program. (IHP-VII Technical Documents in Hydrology) 83, 90 pp.

Föhn, P., Camponovo, C., Krüsi, G., 1998. Mechanical and structural properties of weak snow layers measured in situ. Annals of Glaciology 26, 1–6.

Fukuzawa, T., Narita, H., 1993. An experimental study on the mechanical behavior of a depth hoar layer under shear stress. In: Proceedings International Snow Science Workshop. Breckenridge, Colorado, U.S.A., 4-8 October 1992, pp. 171–175.

Fyffe, B., Zaiser, M., 2004. The effects of snow variability on slab avalanche release. Cold Regions Science and Technology 40 (3), 229–242.

Gauthier, D., Jamieson, J. B., 2006. Fracture propagation propensity in relation to snow slab avalanche release: Validating the propagation saw test. Geophysical Research Letters 35 (13), L13501.

Gibson, L. J., Ashby, M. F., 1997. Cellular solids: structure and properties. Cambridge University Press, Cambridge, U.K.

Gleason, J. A., 2004. Particle image velocimetry; a new technique to measure strain in loaded snow. In: Elder, K. (Ed.), Proceedings ISSW 2004. International Snow Science Workshop. Jackson Hole, Wyoming, USA, 19-24 September 2004, pp. 44–49.

Gubler, H., 1982. Strength of bonds between ice grains after short contact times. Journal of Glaciology 28 (100), 457–473.

Haefeli, R., 1967. Some mechanical aspects on the formation of avalanches. In: Physics of snow and ice, Vol. 1, Part 2. The Institute of Low Temperature Science, Hokkaido University, Sapporo, Japan, 1199–1214.

Herrmann, H. J., Roux, S., 1990. Statistical models for the fracture of disordered media. Elsevier Science Publishers, Amsterdam.

Huber, T., 2008. Deformationsmessungen in geschichteten Schneeproben. B.S. thesis, ETH Zürich, Switzerland.

Jamieson, J. B., Johnston, C. D., 1992. Snowpack characteristics associated with avalanche accidents. Canadian Geotechnical Journal 29, 862–866.

Jamieson, J. B., Johnston, C. D., 2001. Evaluation of the shear frame test for weak snowpack layers. Annals of Glaciology 32, 59–69.

Jamieson, J. B., Schweizer, J., 2000. Texture and strength changes of buried surface-hoar layers with implications for dry snow-slab avalanche release. Journal of Glaciology 46 (152), 151–160.

Johnson, J., 1998. A preliminary numerical investigation of the micromechanics of snow compaction. Annals of Glaciology 26, 51–54.

Joshi, S. K., Mahajan, P., Upadhyay, A., 2006. Study of layered snow under shear and tension. In: Gleason, A. (Ed.), Proceedings ISSW 2006. International Snow Science Workshop. Telluride, Colorado, USA, 1-6 October 2006, pp. 165–173.

Keeler, C. M., Weeks, W. F., 1968. Investigations into the mechanical properties of alpine snow-packs. Journal of Glaciology 7 (50), 253–271.

Kirchner, H., G. Michot, G., Suzuki, T., 2000. Fracture toughness of snow in tension. Philosophical Magazine A 80 (5), 1265–1272.

Kirchner, H. O. K., Peterlik, H., Michot, G., 2004. Size independence of the strength of snow. Physical Review E.

Kovacs, K., Reiweger, I., Herrmann, H., Schweizer, J., 2010. Analytic study of snow failure using a fiber bundle model. submitted to the Journal of Statistical Mechanics.

Kun, F., Costa, M., Costa Filho, R., Andrade Jr, J., Soares, J., Zapperi, S., Herrmann, H., 2007. Fatigue failure of disordered materials. Journal of Statistical Mechanics 2, P02003.

Kun, F., Hidalgo, R., Raischel, F., Herrmann, H., 2006. Expansion of fibre bundle models for creep rupture and interface failure. International Journal of Fracture 140, 255–265.

Lang, R., Leo, B., Brown, R., 1984. Observation on the growth process and strength characteristics of surface hoar. In: Proceedings ISSW 1984. International Snow Science Workshop. Aspen, Colorado, USA, 24-27 October, pp. 188–195.

Lehning, M., Bartelt, P., Brown, B., Fierz, C., 2002. A physical snowpack model for the Swiss avalanche warning: Part III: meteorological forcing, thin layer formation and evaluation. Cold Regions Science and Technology 35 (3), 169–184.

Louchet, F., 2001. Creep instability of the weak layer and natural slab avalanche triggerings. Cold Regions Science and Technology 33 (2-3), 141–146.

Mahajan, P., Brown, R. L., 1993. A microstructure-based constitutive law for snow. Annals of Glaciology 18, 287–294.

Marco, O., Buser, O., Villemain, P., Touvier, F., Revol, P., 1998. Acoustic impedance measurement of snow density. Annals of Glaciology 26, 92–96.

McClung, D., 1979. Shear fracture precipated by strain-softening as a mechnism of dry slab avalanche release. Journal of Geophysical Research 84 (B7), 3519–3526.

McClung, D., 1981. Fracture mechanical models of dry slab avalanche release. Journal of Geophysical Research 86 (B11), 10783–10790.

McClung, D., 1987. Mechanics of snow slab failure from a geotechnical perspective. In: Salm, B., Gubler, H. (Eds.), Symposium at Davos 1986 - Avalanche Formation, Movement and Effects. Vol. 162. IAHS Publication, pp. 475–508.

McClung, D., 2005. Dry slab avalanche shear fracture properties from field measurements. Journal of Geophysical Research 110, F04005.

McClung, D., Schaerer, P., 2006. The Avalanche Handbook, 2nd edition. The Mountaineers, Seattle, U.S.A.

Meier, M., 2006. Produktion von naturidentischem Schnee. M.S. thesis, ETH Zurich, Switzerland.

Mellor, M., 1975. A review of basic snow mechanics. In: Symposium at Grindelwald 1974 - Snow Mechanics, IAHS Publication. Vol. 114. International Association of Hydrological Sciences, Wallingford, U.K., pp. 251–291.

Narita, H., 1980. Mechanical behaviour and structure of snow under uniaxial tensile stress. Journal of Glaciology 26 (94), 275–282.

Narita, H., 1983. An experimental study on tensile fracture of snow. Contributions from the Institute Low Temperature Science, Series A 32, 1–37.

Palmer, A. C., Rice, J. R., 1973. The growth of slipe surface in the progressive failure of over-consolidated clay. Proceedings of the Royal Society of London. Series A 332, 527–548.

Perla, R., 1970. On contributory factors in avalanche hazard evaluation. Canadian Geotechnical Journal 7, 1–6.

Perla, R., 1980. Avalanche release, motion, and impact. In: Colbeck, S. (Ed.), Dynamics of Snow and Ice Masses. Academic Press, New York, pp. 397–462.

Perla, R., Sommerfeld, R., 1987. On the metamorphism, morphology and microstructure of snow. In: Proceedings International Snow Science Workshop. Lake Tahoe, U.S.A, pp. 98–102.

Petrenko, V., Whitworth, R., 1999. Physics of ice. Oxford University Press Inc., New York.

Pinzer, B., Schneebeli, M., 2009. Snow metamorphism under alternating temperature gradients: Morphology and recrystallization in surface snow. Geophysical research letters 36, L2305.

Podolsky, E., Chernous, P., Abe, O., Barashev, N., Nishimura, K., 2008. Experimental study of short-term loading influence on shear strength. In: Campbell, C., Conger, S., Haegeli, P. (Eds.), Proceedings International Snow Science Workshop. Whistler B.C., Canada, 21-27 September, pp. 701–708.

Raischel, F., 2006. Fibre models for shear failure and plasticity. Ph.D. thesis, Universität Stuttgart.

Reiweger, I., Ernst, R., Schweizer, J., Dual, J., 2009a. Force-controlled shear experiments with snow samples. In: Schweizer, J., van Herwijnen, A. (Eds.), Proceedings International Snow Science Workshop. Davos, Switzerland, 27 September - 2 October 2009, pp. 120–123.

Reiweger, I., Schweizer, J., 2010a. Failure of a layer of buried surface hoar. Geophysical Research Letters 37, L24501.

Reiweger, I., Schweizer, J., 2010b. How snow fails. In: Osterhuber, R. (Ed.), Proceedings International Snow Science Workshop. Squaw Valley, CA, October 17-22, 2010, pp. 204–206.

Reiweger, I., Schweizer, J., Dual, J., Herrmann, H., 2009b. Modelling snow failure with a fibre bundle model. Journal of Glaciology 55 (194), 997–1002.

Reiweger, I., Schweizer, J., Ernst, R., Dual, J., 2010. Load-controlled test apparatus for snow. Cold Regions Science and Technology 62 (2-3), 119–125.

Robertson, E. C., 1955. Experimental study of the strength of rocks. Bulletin Geological Society of America 66, 1275–1314.

Roesgen, T., Totaro, R., 1995. Two-dimensional on-line particle imaging velocimetry. Experiments in Fluids 19 (3), 188–193.

Roux, S., 1990. Continuum and discrete description of elasticity and other rheological behaviour. In: Herrmann, H. J., Roux, H. (Eds.), Statistical models for the fracture of disordered media. Elsevier Science Publishers, Amsterdam, pp. 87–114.

Scapozza, C., Bartelt, P., 2003. Triaxial tests on snow at low strain rate. part ii. constitutive behaviour. Journal of Glaciology 49 (164), 91–101.

Scapozza, C., Bucher, F., Amann, P., Ammann, W., Bartelt, P., 2004. The temperature- and density-dependent acoustic emission response of snow in monoaxial compression tests. Annals of Glaciology 38, 291–298.

Schneebeli, M., 2004. Numerical simulation of elastic stress in the microstructure of snow. Annals of Glaciology 38, 339–342.

Schneebeli, M., Sokratov, S., 2004. Tomography of temperature gradient metamorphism of snow and associated changes in heat conductivity. Hydrological Processes 18, 3655–3665.

Schweizer, J., 1998. Laboratory experiments on shear failure of snow. Annals of Glaciology 26, 97–102.

Schweizer, J., 1999. Review of dry snow slab avalanche release. Cold Regions Science and Technology 30 (1-3), 43–57.

Schweizer, J., Jamieson, J. B., 2001. Snow cover properties for skier triggering of avalanches. Cold Regions Science and Technology 33 (2-3), 207–221.

Schweizer, J., Jamieson, J. B., Schneebeli, M., 2003. Snow avalanche formation. Reviews of Geophysics 41 (4), 1016.

Schweizer, J., Michot, G., Kirchner, H. O. K., 2004. On the fracture toughness of snow. Annals of Glaciology 38, 1–8.

Shapiro, L. H., Johnson, J. B., Sturm, M., Blaisdell, G. L., 1997. Snow mechanics - review of state of knowledge and applications. Tech. Rep. CRREL 97-3, U.S. Army Cold Reg. Res. and Eng. Lab., Hanover, N.H.

Sigrist, C., Schweizer, J., 2007. Critical energy release rates of weak snowpack layers determined in field experiments. Geophysical Research Letters 34, L03502.

Sommerfeld, R., 1973. Statistical problems in snow mechanics. In: Perla (Ed.), Advances in North American Avalanche Technology. USDA Forest Service, General Technical Report RM-3, pp. 29–36.

Sommerfeld, R., Gubler, H., 1983. Snow avalanches and acoustic emissions. Annals of Glaciology 4, 271–276.

St. Lawrence, W., 1980. The acoustic emission in snow. Journal of Glaciology 26 (94), 209–216.

St. Lawrence, W., Bradley, C., 1975. The deformation of snow in terms of a structural mechanism. In: Snow Mechanics Symposium (Proceedings of the Grindelwald Symposium), April 1974 International Association of Hydrological Sciences Publication 114, 155–170.

Suo, Z., Hutchinson, J., 1989. Sandwich test specimens for measuring interface crack toughness. Materials Science and Engineering, 135.

Szabo, D., Schneebeli, M., 2007. Subsecond sintering of ice. Applied Physics Letters 90 (15), 151916.

Theile, T., Schneebeli, M., 2010. Algorithm to decompose three dimensional complex structures at the necks, tested on snow structures. IET Image Processing in press.

Theile, T., Szabo, D., Lüthi, A., Rhyner, H., Schneebeli, M., 2009. Mechanics of the ski-snow contact. Tribology Letters 36 (3), 223–231.

Tschirky, F., Brabec, B., Kern, M., 2001. Avalanche rescue systems in Switzerland: Experience and limitations. In: Proceedings of the International Snow Science Workshop, Big Sky, Montana, U.S.A. 1-6 October 2000, Montana State University, Bozeman, U.S.A., pp. 369–376.

van Herwijnen, A., Heierli, J., 2009. Measurement of crack-face friction in collapsed weak snow layers. Geophysical Research Letters 36, L23502.

van Herwijnen, A., Jamieson, J. B., 2005. High speed photography of fractures in weak snowpack layers. Cold Regions Science and Technology 43 (1-2), 71–82.

van Herwijnen, A., Schweizer, J., 2008. Continuous monitoring of acoustic emissions in an avalanche start zone. Geophysical Research Abstracts 10, EGU2008–A–09762.

von Moos, M., Bartelt, P., Zweidler, A., Bleiker, E., 2003. Triaxial tests on snow at low strain rate. Part I. Experimental device. Journal of Glaciology 49 (164), 81–90.

Wakahama, G., 1967. The metamorphism of wet snow. In: Ward, W. (Ed.), International Association of Scientific Hydrology General Assembly of Bern, Comission of Snow and Ice reports and discussions. IAHS Proceedings and Reports 'Red Books' Publication. International Association of Scientific Hydrology, pp. 370–379.

Wei, Y., Adamson, R., Dempsey, J., 1996. Ice/metal interfaces: fracture energy and fractography. Journal of Material Science 31, 943–947.

Yosida, Z., 1963. Physical properties of snow. In: Kingery, W. (Ed.), Ice and Snow. MIT Press, Cambridge, Mass., pp. 485–527.

Curriculum Vitae

Personal data

Name	Ingrid Reiweger
Nationality	September 25, 1978
Nationality	Austrian

Education

since 2006	PhD-student at the SLF and at the ETH Zürich
1998-2006	Studies of Technical Physics at the TU Graz, Austria
2002	Exchange student (Erasmus) at the University of Lund, Sweden

Publications

Reiweger, I., Schweizer, J., 2010. Failure of weak layers in the snowpack: experiments with a layer of buried surface hoar. Geophysical Research Letters 37,L24501.

Reiweger, I., Schweizer, J., 2010. How snow fails. In: R. Osterhuber (Editor), International Snow Science Workshop. Lake Tahoe, California, October 17-22, 2010. Proceedings, pp. 204-206.

Reiweger, I., Schweizer, J., Ernst, R., Dual, J., 2010. Load-controlled test apparatus for snow. Cold Regions Science and Technology, doi:10.1016/j.coldregions.2010.04.002.

Reiweger, I., Schweizer, J., Dual, J. and Herrmann, H.J., 2009. Modelling snow failure with a fiber bundle model. Journal of Glaciology, 55(194): 997-1002.

Genswein, M., Reiweger, I., Schweizer, J., 2009. Survival chance optimized search strip width in avalanche rescue. Cold Regions Science and Technology, 59(2-3): 259-266.

Reiweger, I., Ernst, R., Schweizer, J., Dual, J., 2009. Force-controlled shear experiments with snow samples. In: J. Schweizer and A. van Herwijnen (Editors), Proceedings International Snow Science Workshop. Davos, Switzerland, 27 September - 2 October 2009, pp. 120-123.